Modèles géométriques avec defauts pour la fabrication additive

Zuowei Zhu

To cite this version:

Zuowei Zhu. Modèles géométriques avec defauts pour la fabrication additive. Génie mécanique [physics.class-ph]. Université Paris Saclay (COmUE), 2019. Français. NNT : 2019SACLN021 . tel-02390292

HAL Id: tel-02390292

https://theses.hal.science/tel-02390292

Submitted on 3 Dec 2019

université
PARIS-SACLAY

école
normale
supérieure
paris–saclay

NNT : 2019SACLN021

Modèles géométriques avec défauts pour la fabrication additive

Skin Model Shapes for Additive Manufacturing

Thèse de doctorat de l'Université Paris-Saclay
préparée à École normale supérieure Paris-Saclay

Ecole doctorale n°579 Sciences mécaniques et énergétiques, matériaux et géosciences (SMEMAG)
Spécialité de doctorat : Génie Mécanique

Thèse présentée et soutenue à Cachan, le 10 Juillet 2019, par

ZUOWEI ZHU

Composition du Jury :

M. François Villeneuve Professeur, G-SCOP - UMR 5272, Université Grenoble Alpes	Président
M. Alex Ballu Maitre de Conférences HDR, I2M - UMR 5295, Université de Bordeaux	Rapporteur
M. Jean-Yves Dantan Professeur, LCFC - EA 4495, Arts et Métiers ParisTech	Rapporteur
M. Olivier Bruneau Professeur, LURPA - EA 1385, Université Paris-Sud	Examinateur
M. Luc Mathieu Professeur, LURPA - EA 1385, Université Paris-Sud	Examinateur
M. Giovanni Moroni Professeur, Politecnico di Milano	Examinateur
Mme Lihong Qiao Professeur, Beihang University	Examinatrice
M. Nabil Anwer Professeur, LURPA - EA 1385, Université Paris-Sud	Directeur de thèse

Thèse de doctorat

Contents

List of Figures

List of Tables

Abbreviations

AM Additive Manufacturing

ANOVA Analysis of Variance

CAD Computer-Aided Design

CASC Circular Approximation with Selective Cornering

CAT Computer-Aided Tolerancing

CCS Cartesian Coordinate System

CCW Counter-ClockWise

CNN Convolutional Neural Network

CT Computed Tomography

DCT Discrete Cosine Transform

DfAM Design for Additive Manufacturing

DoE Design of Experiment

DRF Datum Reference Frame

DSI Discrete Smooth Interpolation

ESC Energy Significance Criterion

FD Fourier Descriptors

FDM Fused Deposition Modeling

FEA Finite Element Analysis

FFD Free-Form Deformation

FSE Fourier Series Expansion

GP Gaussian Process

GPS Geometrical Product Specification

HDC Hausdorff Distance Criterion

KDE Kernel Density Estimate

LHD Latin Hypercube Design

MCMC Markov Chain Monte Carlo

MMD Metric Modal Decomposition

MRI Magnetic Resonance Imaging

PCA Principle Component Analysis

PCS Polar Coordinate System

PDM Point Distribution Model

RMSE Root Mean Square Error

SCS Spherical Coordinate System

SLM Selective Laser Melting

SMA Statistical Modal Analysis

SMS Skin Model Shapes

SSA Statistical Shape Analysis

SSM Statistical Shape Model

STL STereoLithography

VTA Vertex Translation Algorithm

Chapter 1

Introduction

Additive Manufacturing (AM), as a rapidly growing manufacturing technology nowadays, was first explored and applied in the automotive, aerospace and medical industries. It is considered as one of the pillars of the fourth industrial revolution. AM is also known as Rapid Prototyping, Direct Digital Manufacturing, Freeform Fabrication, 3D Printing and Layered Manufacturing. Different from traditional machining, in which parts are made by removing materials from a larger stock through different processes, AM fabricates volumes layer by layer from their three-dimensional CAD model data, thus enabling the fabrication of products with more complex shape and internal structure.

The different technologies of AM have been comprehensively investigated by researchers from industry and academia. A classification of additive manufacturing technologies can be found in Table 1.1 according to their characteristics.

Categories	*Description*	*Related technologies*
Binder jetting	Binding agent selectively deposited to join powder particles	Ink-jetting, 3D Printing
Material jetting	Droplets of build material selectively deposited and fused	Multi-Jet Modeling (MJM)
Powder bed fusion	Regions of powder bed selectively fused by thermal energy	Electron beam melting (EBM), Selective Laser Sintering (SLS), Selective Laser Melting (SLM)
Directed energy deposition	Deposited materials fused by focused thermal energy	Laser metal deposition (LMD)
Sheet lamination	Sheets of material trimmed and bonded together in layers	Laminated object manufacturing (LOM), Ultrasonic Consolidation(UC)
Vat photopolymerization	Liquid photopolymer selectively cured by light activation	Stereolithography (SLA), Digital Light Processing (DLP)
Material extrusion	Material selectively dispensed through nozzle or orifice	Fused Deposition Modeling (FDM)

Table 1.1: Categories of AM processes as classified by ASTM [AST13]

Despite the advantages brought by AM, the control of geometrical accuracy remains a major bottleneck that hinders its mass adoption. The geometric deviations resulting from different error sources, including geometric approximation errors, machine errors and especially material related errors, demonstrate far more complex patterns than traditional manufacturing processes. Therefore, effective modeling of these geometric deviations becomes an important topic within the research of AM and will significantly benefit different aspects of the AM process chain.

Among the many investigated tasks of Design for Additive Manufacturing (DfAM), the geometrical validation aiming to ensure the consistency between digital product and the final outcome, as well as design optimization intended to achieve optimal geometrical or topological design incorporating process knowledge, are also closely concerned with geometric deviations [LSAL15, TMV+16]. In the tolerancing domain, driven by the new characteristics and capabilities of AM, challenges with the tolerance specifications are emerging, posing the need for a more comprehensive investigation of geometric deviations with respect to process-, material- and geometry-related properties of AM [AWML15, MPP17]. The quality control of AM process calls for accurate prediction of geometrical defects on manufactured products, so that appropriate compensation plans can be made to improve the products' geometric accuracy. All these demands have motivated the research to develop a deviation modeling framework for AM processes. However, existing methods are not mature yet to be used for this purpose due to several reasons:

- Methods developed for traditional manufacturing process cannot account for the new layer-per-layer mechanism of AM;
- Methods developed for AM tend to focus on some specific issues such as material shrinkage, warpage effect, etc., making them unsuitable for modeling the deviation of the overall part geometry;
- Most methods ignore the effects of process conditions, while the thermal and mechanical behavior in the AM manufacturing process is quite sensitive to the changes of process conditions.

Therefore, a comprehensive deviation modeling framework is necessary for geometry and quality control in AM.

With the theoretical background of Geometrical Product Specification and Verification (GPS), the Skin Model Shapes (SMS) is proposed as a comprehensive deviation modeling framework that could be used in different stages of the product life-cycle to model shape variability [ABM13]. SMS considers geometric deviations that are either predictable or observable in actual manufacturing processes. Though SMS has proved its effectiveness in several engineering applications, the extension to AM has seldom been exploited and the challenges are non-trivial. From the prediction perspective, since AM remains a new kind of manufacturing process, the process knowledge from either industries or the academic world is yet immature. From the observation perspective, common measurement devices hardly allow to gain information of deviations that occur within the layers, which impedes the layer-wise investigation of the deviations. On the other hand, AM simulation techniques came into development only in recent years and their capability remains to be further exploited. The varieties of deviation sources in AM cause much fuzziness in identifying the systematic and random properties of deviations, and result in unrepeatable deviation patterns that are hard to capture using conventional methods developed for the current SMS framework.

The challenges have elicited new research questions, among which the followings are identified in this thesis:

- How to represent deviations in an appropriate deviation space, in which the deviation signatures or patterns could be intuitively identified?
- How to parameterize the deviations in the deviation space, thus a limited number of parameters could sufficiently explain the deviation signatures or patterns?
- Considering observation data from measurement or simulations, how to estimate the parameters and derive predictive deviation models that could be used to predict deviations for new parts?

Therefore, in this thesis, we address these questions with new deviation modeling methods and a novel framework is proposed to build SMS for Additive Manufacturing. With detailed discussion as well as experimental validation of the methods, the rest of this thesis is organized as follows:

In Chapter 2, the current status of research on the geometric deviation modeling methods for AM processes are investigated. Three major categories of methods are identified and their respective characteristics are discussed. The theoretical background as well as the applications of the SMS is introduced. Regarding the characteristics of AM, a classification of in-plane and out-of-plane deviation has been made which respectively models the shape variations within each layer and the deformation of each layer towards the build direction. This classification decomposes the whole part surface into separate layers on which the modeling problem will be addressed and conforms to the layer-based nature of AM processes. Based on this classification, the general framework for developing the SMS for AM is proposed.

In Chapter 3, the in-plane deviation modeling is discussed. The shape parameterization methods aim at deriving parametric models to describe the nominal and actual in-plane shapes and to represent the in-plane deviation as their radial difference in the Polar Coordinate System. A transformation based method is proposed to parameterize the in-plane deviation with a set of transformation parameters which capture the typical variations of the in-plane shape. Bayesian inference is adopted to gain an estimation of the transformation parameters in the parametric function together with evaluation of the estimation uncertainty. A multi-task Gaussian Process model is further proposed which conducts concurrent learning of the residual deviations for a batch of parts.

In Chapter 4, the out-of-plane deviation modeling is proposed. To begin with, the deviations are modeled from the whole part surface combining systematic and random deviation models with surface deformation techniques such as Free-form Deformation. In order to achieve more precise investigation, statistical modal analysis methods are adopted to realize layer-level modeling of out-of-plane deviations. A grid-based structure is used for deviation representation, based on which mode-decomposition methods are adopted to parameterize the deviation with frequency or geometrical modes. These modes are further characterized with respect to design and process parameters, and finally a deviation model is obtained that could make layer-wise prediction of out-of-plane deviations.

In Chapter 5, the deviation models are applied to obtain the deformed geometry of each layer of a part and a layer connection algorithm is proposed to conduct inter-layer triangulation to finally construct the complete SMS of the AM part. A case study is presented to illustrate all the mentioned methods on a graphical user interface developed on the MATLAB platform.

In Chapter 6, the conclusion is drawn. Perspectives on the possible improvements of the existing research and some promising directions for the future work are envisioned.

Chapter

2

Literature review

Contents

2.1 Introduction

Deviation modeling requires effective identification of error sources in the process. Though the mechanisms of different AM processes may vary, they typically share a similar work-flow, as illustrated in Figure 2.1. This work-flow is composed of an input phase, a build phase and an output phase. The input phase deals with the preparation of input data, in which the CAD part model is converted as a STereoLithography (STL) file format that provides the geometric information readable for the AM machine. This file is further processed to repair the possible defects in geometry before being transferred to the machine. In the build phase, following process settings such as build orientation, layer thickness, energy intensity and support structure, the part is manufactured in a layer-by-layer manner. To meet quality and performance requirements, in the output phase, procedures like support removal, cleaning, heat treatment and NC machining are conducted.

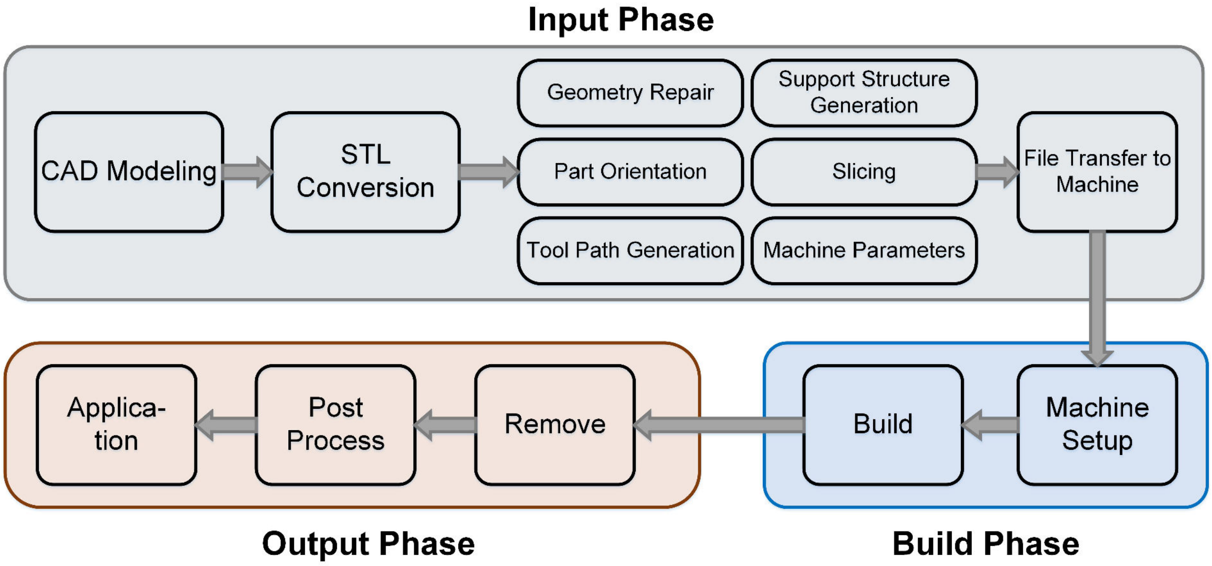

Figure 2.1: Typical work-flow of an AM process

Factors arising from each of the above phases may induce or affect the geometric deviations on the manufactured part. Based on [Reh10], Figure 2.2 provides a cause-and-effect diagram that makes a summary of such factors. Starting from these factors, research efforts are devoted either to modeling their relationships with resulting deviations or to improve them in product design according to the quantified magnitude of deviations, among which three major categories of methods can be identified focusing on the following topics: geometric approximation error, machine error and process parameters, and quality issues from material behavior. Therefore, in Section 2.2 of this chapter, a brief review is conducted on these methods and remarks will be given regarding their strengths and weaknesses.

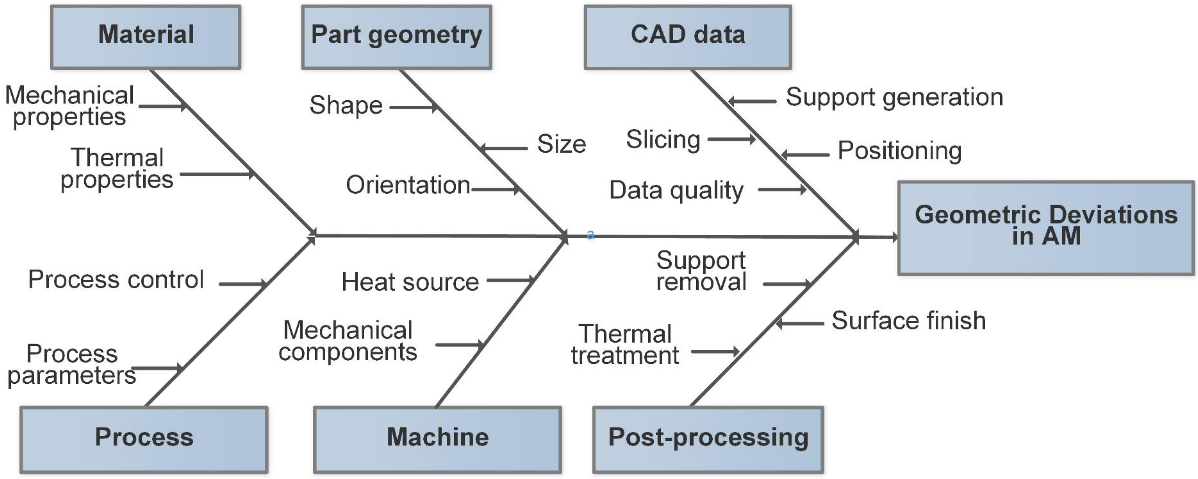

Figure 2.2: Cause-and-effect diagram of geometric deviations in AM [Reh10]

Whereas, the capability of the mentioned works is still limited, since they could cover only specific issues or phases of the process. Hence, a more comprehensive deviation modeling framework is anticipated, which could provide detailed solutions to the prediction and representation of deviations. In this regard, the SMS will be demonstrated as a promising choice for this framework. As a background, the concept, methodology as well as applications of SMS are introduced in Section 2.3. The challenges upon extension of SMS to the AM process are non-trivial. Considering the layer-per-layer characteristics of AM, new methods have to be developed shifting the current feature-wise modeling manner to the layer-wise manner. Therefore, in Section 2.4, a general framework for the development of SMS in AM is proposed, which serves as the guideline of the following chapters.

2.2 Geometric deviation modeling in Additive Manufacturing

2.2.1 Geometric approximation errors

The investigation of geometric approximation errors is motivated by the fact that current AM technologies do not work directly on the original CAD model, but use the

STL file as input, in which the nominal part surface is approximated as a triangular mesh representation. Therefore, a “chordal error” is introduced during the translation from CAD to STL, and is defined as the distance between the STL surface patch and the CAD surface, as can be seen from Figure 2.3(a). Besides, a “staircase error” takes place due to slicing of the STL file when building the part layer-by-layer, as shown in Figure 2.3(b). The average chordal error and maximum cusp height have been adopted to estimate the two errors respectively.

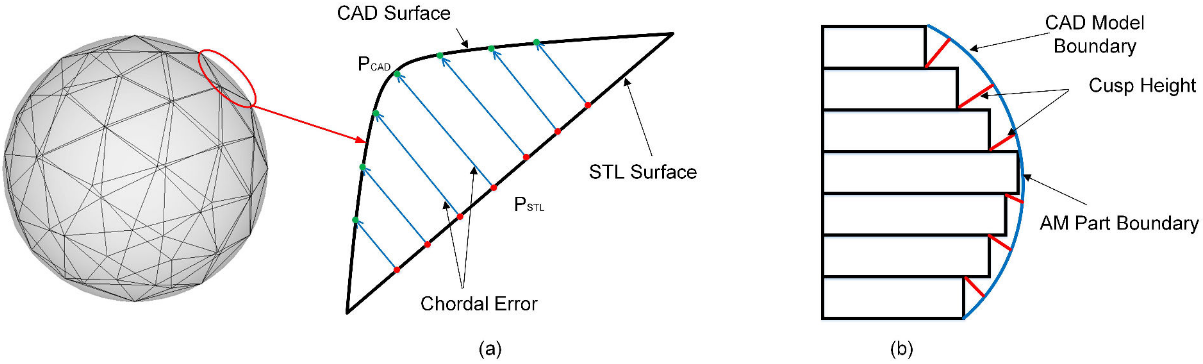

Figure 2.3: 2D illustration of (a) the chordal error (b) the staircase error

To reduce the chordal error, the Vertex Translation Algorithm (VTA) is proposed by Navangul et al. [NPA13], in which the chordal error is computed as the distance between selected points on the STL facet and their correspondences on the NURBS patch of the CAD surface. In each facet, the point with maximum chordal error is identified and translated to the CAD surface. By connecting the translated point with the facet vertices, three new triangle facets are then generated and updated in the STL file, while the original facet is deleted, as shown in Figure 2.4. This algorithm aims at improving the STL file quality by modifying the facets iteratively until chordal errors are minimized. However, to meet the predefined tolerance criteria, a large number of iterations may be expected, each requiring significant computational cost. The STL file size will also be increase with the newly added facets. Similarly, the Surface-based Modification Algorithm [ZA15] modifies the STL file by adaptively increasing the facet density at individual part surfaces whose average chordal error and cusp height error are above a threshold. Whereas, the possibility to induce exponential growth of file size makes it only preferable for high-accuracy part models.

Another solution proposed by Kunal [Sha14] attempts to minimize the errors by

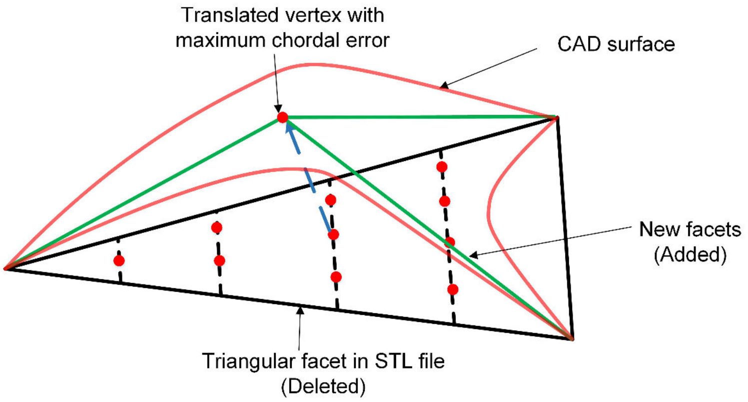

Figure 2.4: Illustration of the VTA algorithm

modifying 2D contours obtained by slicing the STL model. Chordal points are sampled on each chord of the 2D slice contour and the chordal error is evaluated as the distance between such points and their nearest counterparts on the NURBS surface. If the chordal error is above the predefined threshold, related chordal points are shifted to the NURBS surface. This process is iterated until the chordal error falls below the threshold, and new slice contours are constructed by linking the new points. This method quite resembles a 2D version of the VTA algorithm, but operates directly on the slice geometry and achieves a manufacturing-level modification. As an alternative to the de-facto STL file format, new file formats are emerging that support the representation of curved surface patches and manage to achieve more accurate approximation to the CAD surface with reduced chordal errors. Typical representatives of such formats are the Steiner patch [PA15] and the Additive Manufacturing Format (AMF)[ISO16].

The reduction of staircase error has been approached with different adaptive slicing methods. Instead of the traditional practice which applies a uniform slice thickness on the whole part, adaptive slicing conducts slicing with variable slice thicknesses in order for improved surface quality and reduced build time. In [SPA15], a method termed as Modified Boundary Octree Data Structure is used to convert the STL file of an object to an Octree structure, by iteratively subdividing a universal cube enclosing the STL file into small node cubes according to the defined subdivision conditions. The heights of the final cubes can then be identified as slice thicknesses. Within a virtual manufacturing framework, the ability of this method in improving geometrical accuracy of the manufactured part has been proved. However, the lack of direct support for adaptive slicing in current AM machines has limited its application. Regarding this limitation, a clustered adaptive slicing approach is introduced in [PPA14]. The whole part model is subdivided into subparts stacking on top of each other along the build direction. A uniform slice thickness is calculated for each subpart and the appropriate thickness values are determined using a KD-tree structure. The local adaptive slicing strategy also facilitates the convenient mitigation and evaluation of GD&T errors.

The aforementioned approaches mainly focus on improving the quality of input file to reduce shape deviations, so they are independent from any specific AM process and can be applied in the early design stage when no process information is available yet and only digital models are at hand. Nevertheless, they cannot provide a analytical form of geometric deviations and an appropriate criterion for modification is difficult to choose due to the costly trial and error process. In this thesis, since the deviation modeling problem will be tackled based on the STL model directly and the objective is to derive a complete model of the geometric deviations in AM, the approximation error will not be considered.

2.2.2 Machine error and process parameters

Tong et al. [TALJ03, TLJ04, TJL08] propose a parametric model of the repeatable errors in SLA and FDM machines. The model parameters are estimated through regression on measurement data gathered at specific points of the manufactured part surface. The model allows for the prediction of systematic geometric deviations, and appropriate compensations can be made on the input files (STL or slice file) to mitigate the deviations. However, since only a small number of points are considered for model estimation, the continuity may not be guaranteed when the model is applied to the whole part surface. Dantan et al. [DHG+17] consider the deviations resulting from different types of machine errors as a set of deviation modes. For a cylindrical part, the 'ellipse mode' and 'rounded rectangle mode' are used to describe the effects of machine movement control errors, and the 'gap mode' is used to describe the gap in the machine moving axis. These modes are mutually independent and correct identification of them would facilitate the understanding of the machine errors.

In metallic AM processes, the shrinkage behavior has been investigated with respect to process parameters. The overall shrinkage is measured by the shrinkage ratio along the x,y and z coordinates axes, and is represented as the dimensional changes in the manufactured part compared to the nominal dimension. Non-linear models of the shrinkage ratio are studied with respect to the hatch length [NWF05] and scan speed parameters [NWFL06] in direct metal laser sintering (DMLS). Through optimization of the models, more homogeneous sintered material properties and improved part quality can be obtained. In [RP07, SPR08, SPR09a, SPR09b], the relationship between shrinkage ratio and various SLS process parameters is investigated. A linear function combining the considered parameters as well as their interactions is proposed and analysis of variance (ANOVA) is conducted to identify the most significant parameters. In a similar manner, an empirical model of the cylindricity and flatness is developed in [SPR12] considering laser power, scan speed, powder bed temperature, part size and build orientation. These approaches bypass the black box of the potential mechanical or physical mechanisms in AM, but directly correlate the observed deviations with machine and process parameters through experiments. Though the shrinkage ratio alone cannot capture the detailed deviations at specific locations of part surface, the results of such approaches help to gain an insight of the effects from process parameters and lay the foundation for experimental studies involved in this thesis.

2.2.3 Quality issues from material behavior

Another major research force is from the researchers in quality control for AM, with the aim to build analytical models of shape shrinkage through statistical analysis of manufactured parts. A series of studies conducted by Huang et al. [XHSD13, SWHT14, HNX+14b, SDH+14, HZSD15a] have been dedicated to developing a predictive shape deviation model that is able to learn from the deviation data obtained from a small number of test product shapes and accordingly make compensation on new and untested shapes. Since AM is a layer-wise building process, the shrinkage deviations occur both inside each 2D layer and along the build direction. Therefore, they subdivide the overall deviation into in-plane and out-of-plane deviation. The in-plane case deals with the shrinkage of the 2D shape in a single fabricated layer and the out-of-plane deviation denotes the deviation of a layer along the build direction.

The work initiates in modeling the in-plane shrinkage for the mask-image-projection-based Stereolithography (MIP-SLA) and FDM processes. To develop this model, a Polar Coordinate System (PCS) is established on the 2D layer and the deviation is defined as the difference between nominal shape and the actual shape in different polar angles. By observing the distribution of deviation along the shape profile, a parametric function is "prescribed" and the function parameters are estimated using Bayesian inference based on measurement data. This idea is first validated on circular shapes with different sizes, and further extended to polygonal shapes by adding an extra "cookie-cutter" component [HNX+14a]. The applications on free-form shapes [LH15] and metallic AM process [LGCH19] are also exploited. However, these methods are formulated in a shape- and process-specific way, and therefore cannot be well generalized to other shapes or identical shapes manufactured in a different process setting. Especially, if the target shape has internal features or is not convex, multiple PCSs need to be established and coordinated, thus increasing the model complexity. Cheng et al. [CTW17] further improve the in-plane model with a statistical transfer learning perspective that decomposes shape deviation into shape-specific and shape-independent components, the knowledge acquired from the latter could be transferred across different shapes. On the other hand, in order to enrich the in-plane model with the consideration of process parameters, a statistical model is developed by Cheng et al. [CWT18] that formulates the deviation of the 2D shape profile manufactured by the FDM process with two influential factors: part size and infill percentage.

With the foundations of in-plane deviation modeling, the out-of-plane deviation problem is tackled in a similar way by introducing the Spherical Coordinate System (SCS) established on the whole part body with the z-axis along the build direction [JQH15, JQH16, JJH16]. Then outer boundary of the product shape is divided into vertical cross-sections and the out-of-plane deviation is represented as the displacement of points on the cross-section contour in the build direction. For cylindrical shapes, the cross-section is a rectangular shape and the model derived for in-plane deviation can be easily adapted here.

The classification of in-plane and out-of-plane deviation is justifiable when considering the layer-wise working mechanism of AM. The initiative to use PCS for in-plane deviation modeling enables the convenient and generic parametrization of deviation, without having to incorporate extra shape-related parameters. The main challenge, however, is the limited transferability between different shapes and the lack of consideration for process conditions. These approaches have significantly motivated this thesis work, the same classification is made in this thesis and new methods have been proposed on this basis aiming at overcoming the weaknesses of current methods.

2.2.4 FEA-based deviation simulation

Finite Element Analysis (FEA) methods have been extensively investigated regarding different AM processes. The geometric deviations on AM parts mainly result from the thermal and mechanical effects in the building and cooling process. An FE model of the FDM process is developed in [ZC06], in which the 'element activation-deactivation' technique is used to simulate the extruder movement over time. The temperature and displacement fields of the part are then calculated. This model is further applied in a parametric study [ZC08] to investigate the effects of process parameters on the resulting part deviations. It is revealed in this study that the scan speed, layer thickness as well as bead width are the major influential factors. The curl distortion on parts manufactured by the SLA process is investigated in [BCLO95] with an FE model. The curl distortion denotes the deviation of the fabricated layer towards the build direction and is induced by the shrinkage of the resin after solidification. It can be treated as a kind of out-of-plane deviation and according to this research, its magnitude is closely related to the part size and layer thickness. Whereas, the major research attention has focused on powder bed-based AM processes with the aim to derive efficient FE models for prediction of residual stress and part distortion. Most works adopt thermo-mechanical models. Given material properties and process parameters, the transient temperature field of the whole part is calculated, following which mechanical calculations are performed to derive the stress and distortion [DIM14, MZD17]. Multi-scale models are also proposed which sequentially investigate the melt pool at micro-scale, the layer temperature history at meso-scale and the stress/distortion field at macro-scale [LFGF16, LLG17]. Though current research on FEA of AM processes is still limited due to assumptions made on the physical conditions and simplified geometries used for model validation, as indicated in [BS18], they could be used in the design stage to provide preliminary information about the possible geometric deviations of AM parts.

The methods mentioned above mainly come from the academic world, some of which are further integrated in commercial AM simulation tools for industrial applications, for example Amphyon® [KNXP13] and Netfabb® [MMP+14]. Apart from the flexibility in building parts with different geometric complexities, the industry is more concerned with the gaps between as-designed and as-built part introduced in the AM process. To allow for improved geometric accuracy and optimized process parameter selection and to assess the effect of process parameters on part behavior, multiple AM simulation tools have been released by different companies across the world. In this section, a review of these tools is provided and a comparison is made regarding their key characteristics.

Mainstream AM simulation tools conduct simulations based on FE analyses considering characteristics of AM processes. Apart from traditional FEA software, for example Abaqus, other companies are rapidly growing and new software tools are developed in collaboration with academia. Table 2.1 and 2.2 give a comprehensive overview of 6 AM simulation tools, in which the input, output, simulation model and some other characteristics are summarized. Mainstream AM simulation tools mainly focus on metal-based AM processes and share a similar workflow. Starting from the CAD model or STL file of the part, a discretized Finite Element mesh model is generated. Based on specified process parameters, build orientation and support structures that are manually or automatically generated, the simulation procedure is conducted typically by activating inactive mesh elements layer-by-layer according to the predefined scanning strategy, which resembles the sintering or melting effect of lasers or electron beams. The residual stresses and part deformations are the main concerns of the simulation process since they have significant influence on the performance and geometrical accuracy of the end-part. To make an accurate prediction of them, different FEA methods are adopted in these tools. Multi-scale and multi-physics models are used to take into account the thermal, metallurgical and mechanical effects in either micro-, meso- or macro-scale. The simulation result provides information about the part distortions and a compensated geometry of the part is automatically generated in some tools. Figure 2.5 shows the general procedures of an AM simulation tool.

In this thesis, data-driven models are proposed combining statistical learning methods to obtain reliable deviation models. Data-driven methods pose a need for large amounts of observation data. However, considering the time-consuming manufacturing and measurement process even for just one part, a tremendous effort may be anticipated for data collection from the real manufacturing process. In this context, AM simulation tools make it possible to conduct quick and easy-to-control virtual manufacturing of numbers of parts with simple settings of related parameters. And the results are given in a regular data structure from which meaningful in-process and post-process informa-

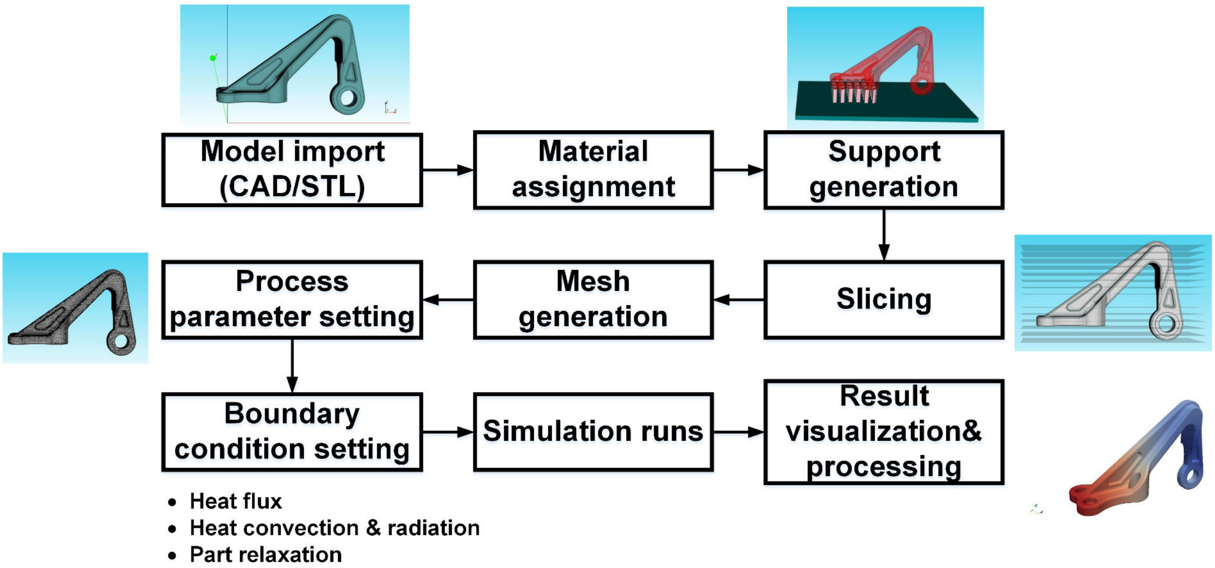

Figure 2.5: General procedures of an AM simulation[Geo18]

tion could be conveniently retrieved. In addition, a unique benefit of AM simulation is its ability to predict the deviation of internal part structure, which is impossible or quite difficult to be obtained from real manufactured parts. Therefore, AM simulation will be used in several topics of this thesis to provide deviation data for analysis.

Solution	*Provider*	*Process*	*Input*	*Mesh*	*Hatching*	*Simulation routine*
Virfac [Geo18]	GeoNX	SLM,LMD	CAD model	FE mesh (hexahedral elements)	Predefined Customized	Progressive activation of 'inactive' elements by a selection box along the path
Ansys Additive (Exasim) [ANS18]	Ansys (3DSIM)	Metal based	STL file	FE mesh (hexahedral elements)	Predefined Customized	N/A (Not available)
Simufact [Com18]	MSC software	Metal based	CAD model	FE mesh (hexahedral elements)	Customized	N/A
Netfabb (Project Pan) [Aut18]	Autodesk (Pan Computing)	Powder bed Wire-fed	STL file	FE mesh (Hex8 elements)	Customized	Progressive activation of 'inactive' elements using a hybrid inactive element activation method
Abaqus [3DS18]	Dassault Systems	Metal based	CAD model	FE mesh	Customized	Progressive activation of 'inactive' elements according to the machine code
Amphyon [Wor18]	Additive Works	LBM,SLM,DMLS	STL file	FE mesh	Predefined	N/A

Table 2.1: Comparison of commercial AM simulation solutions: Part 1

Solutions	*Simulation model*	*Geometry compensation*	*Output*	*Research partner*
Virfac	FE solver Morfeo, coupling thermal, metallurgical and mechanical analyses	No	Displacement of mesh nodes in X, Y and Z direction	Erlangen Univeristy (Germany)
Ansys Additive	Thermal and mechanical solvers	Yes	Displacement of mesh nodes in X, Y and Z direction, compensated STL file	N/A
Simufact	MSC's MARC solver, thermal-mechanical coupled transient analysis	Yes	Displacement of mesh nodes in X, Y and Z direction, compensated CAD model	Renishaw (UK)
Netfabb	Moving source sequential thermo-mechanical FEA analyses	Yes	Deformed and compensated STL file	Pennsylvania State University (USA)
Abaqus	Simulation of heat convection, conduction and radiation	Yes (RSO Tool)	Compensated STL file	Oak Ridge National Laboratory (USA)
Amphyon	Thermal-mechanical solver	Yes	Deformed and compensated STL file	Altair (USA)

Table 2.2: Comparison of commercial AM simulation solutions: Part 2

2.3 The Skin Model Shapes

Looking back at the reviewed deviation modeling methods, it can be seen that they respectively have a specific application scope and their transferability is limited when being used for other applications. A unified framework combining the miscellaneous methods will significantly assist different activities in the AM process chain. The SMS, as a new paradigm for geometric deviation modeling that has gained active development in the past decade, is a promising choice for this framework. It has the ability to model both 2D and 3D deviations either by prediction based on assumptions, or by learning from observation data of manufactured or simulated samples, thus covering multiple stages of the AM process. This section is dedicated to a general introduction to the SMS, together with a discussion on the challenges in its extension to AM.

2.3.1 The Skin Model Shapes concept

The ISO GPS (Geometrical Product Specifications) standards are based on a model/ language description of the actual shape of the mechanical parts and a set of operations to geometrically specify constraints and requirements for design, manufacturing and metrological control. Although these standards have led to unambiguous descriptions and better communication between the various actors in the product life cycle, digital modelling and simulation tools do not yet allow an accurate geometric representation of the real shape of mechanical parts, thus contributing to very restrictive or even incomplete studies of the real behavior of complex mechanical systems.

GeoSpelling is proposed by Mathieu and Ballu [BM96] as a univocal language that could be used across design, manufacturing, and inspection to communicate geometric information and requirements along the product life cycle [SAMW14]. In Geospelling, a geometric specification is defined as "a condition on a characteristic defined from one or between several geometric features", as shown in Figure 2.6. Multiple operations, namely partition, extraction, filtration, association, collection and construction are defined to extract certain ideal or non-ideal geometric features, among which the non-ideal features refer to features obtained from the Skin Model. Table 2.3 and Figure 2.7 shows the operations defined in the GPS standard [17411].

The Skin Model refers to the interface, or skin of the part that separates its material from the surrounding environment. This Skin Model conveys the designer's idea about

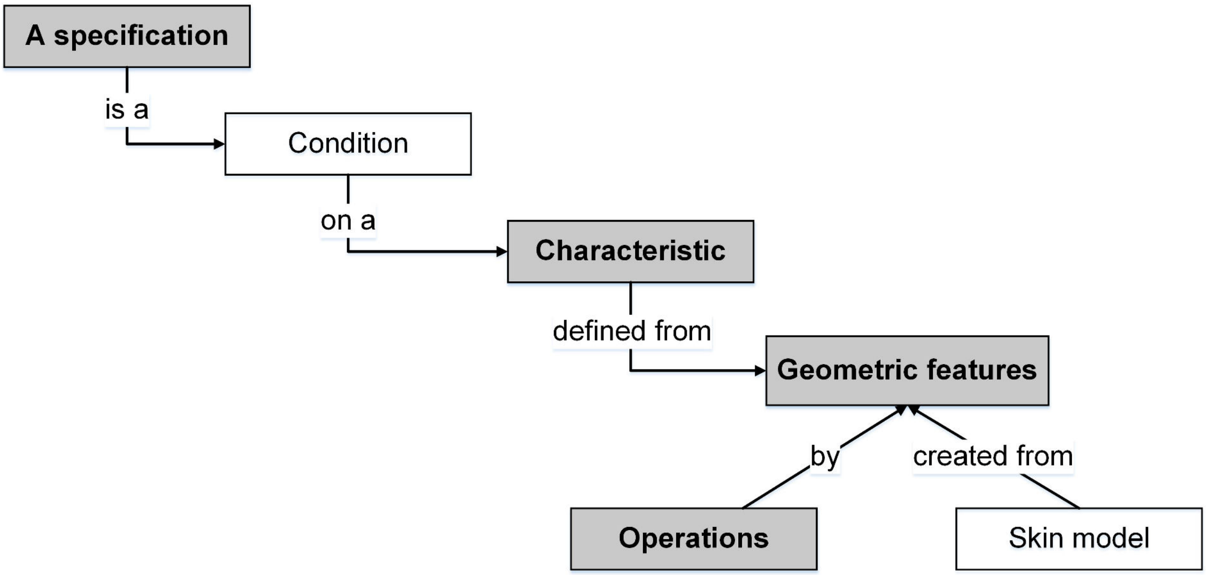

Figure 2.6: The Geospelling concept [DBM08]

Operations	*Explanation*
Partition	To identify bounded features from ideal/non-ideal features
Extraction	To identify specific points from a non-ideal feature
Filtration	To create a non-ideal feature by reducing the level of information
Association	To fit ideal features to non-ideal features
Collection	To consider more than one features together
Construction	To build ideal features from other ideal features with constraints

Table 2.3: Operations defined in the GPS standard [ZAMZ11]

all the possible defects on the nominal geometry. This surface model of non-ideal geometry is not unique and can take on an infinite number of forms and representations. It is also considered as a continuous surface consisting of an infinite number of points [22411]. Whereas, driven by the need for computation and processing of the Skin Model for engineering applications, a finite representation has to be developed, thus the idea of SMS has been introduced as finite Skin Model representatives composed of a finite number of geometric parameters or points [SAMW14].

The generation of SMS is typically divided in two stages: the 'Prediction stage' refers to the design stage when geometric deviations are not yet observable and therefore an 'a-prior' model has to be developed according to knowledge or by making assumptions on systematic and random deviations; the 'Observation stage' refers to the more detailed design stage when information of geometric deviations is made available through process

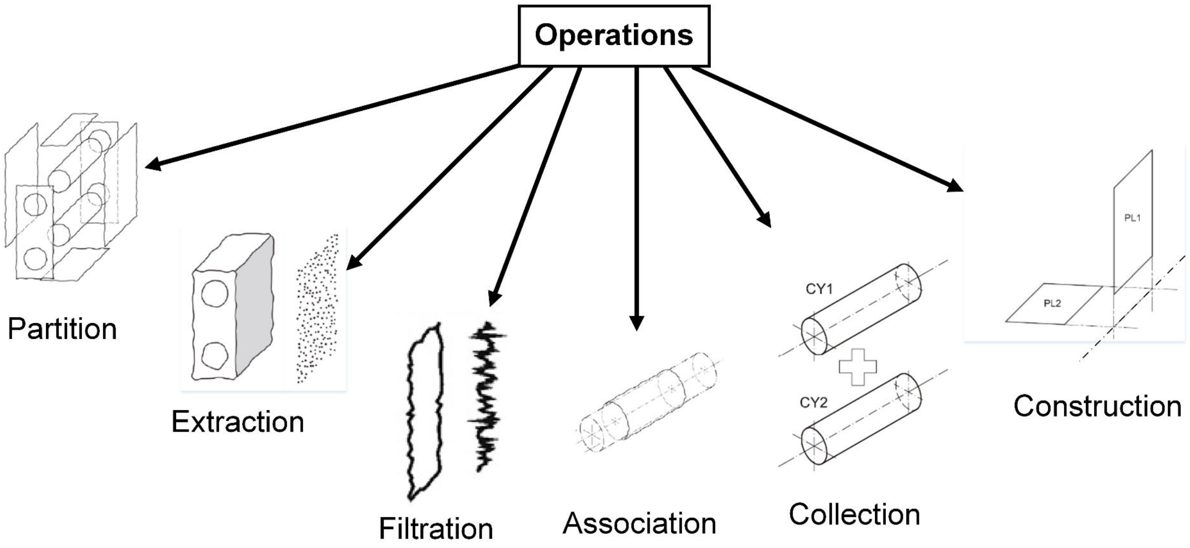

Figure 2.7: The operations defined in Geospelling [DBM08]

simulations or measurement of manufactured samples. Such information is further used either to calibrate the deviation models in the prediction stage, or to derive statistical models to generate deviations of new samples [SWW+12, SAMW14, ASMW14]. The generated SMSs, however, do not necessarily conform to the tolerance specifications. Therefore, the deviations on features of SMSs need to be evaluated and consequently scaled with respect to the specified tolerances [SW15b].

2.3.2 Geometric representation of Skin Model Shapes

Discrete geometry based on point clouds and polygonal meshes has been adopted to facilitate representation of SMS in computer systems, due to its convenient accessibility from CAD tools and manufacturing data as well as the ability to flexibly approximate surfaces. As shown in Figure 2.8, the representation scheme of SMS starts from the nominal CAD model of a part. A tessellation procedure is conducted to convert the CAD model to a point cloud or triangular mesh that serves as representative of the external part surface. In order to consider geometric deviations with respect to tolerance specifications, geometric operations such as partition and extraction are executed on the tessellated model to extract the specific toleranced features, on which geometric deviations are simulated using different deviation modeling methods. Thereafter, these deviated features are combined with other features through collection and association operations to obtain the non-ideal part geometry. This procedure is called deviation simulation. Furthermore, by assessing the deviated geometry with respect to the nominal part model, visualization techniques at different scales can be utilized to illustrate the magnitude and distribution of deviations on the part surface.

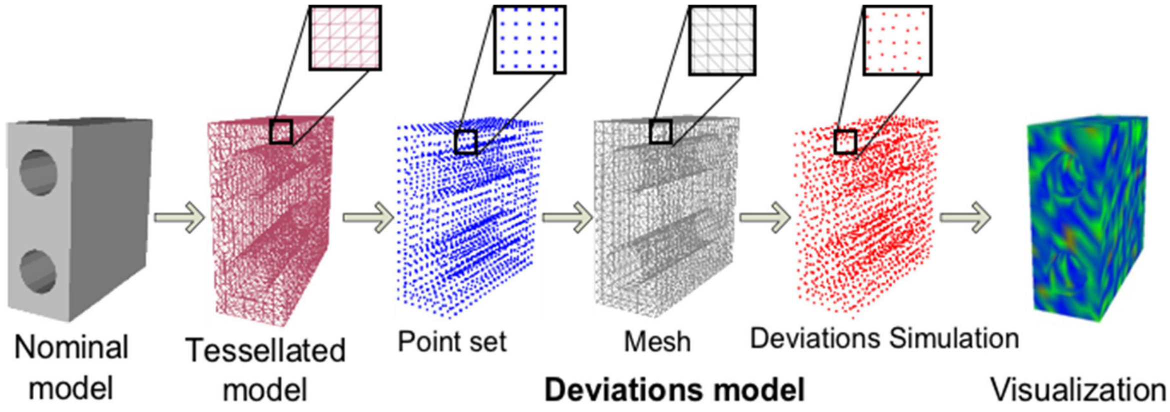

Figure 2.8: Skin Model Shape creation process [ABM13]

2.3.3 Deviation modeling in Skin Model Shapes generation

Modeling of geometric deviations is the core of SMS representation. In this section, deviation modeling methods in the two respective stages as mentioned above will be summarized.

2.3.3.1 Modeling deviations in the prediction phase

In the prediction phase, due to lack of knowledge, assumptions have to be made on systematic and random deviations. Systematic deviations denote deviations that can be observed in a majority of parts manufactured under the identical or similar manufacturing conditions, and show repeatable patterns. Whereas, random deviations result from unpredictable factors in the manufacturing process such as tool wear and unexpected changes in the surrounding environment.

Modeling systematic deviations

Based on the experience that most observable systematic deviations of a planar feature can be represented by a single second-order shape or a superposition of multiple such shapes, Zhang et al. [ZAS+13] and Schleich et al. [SAMW14] proposed to model systematic deviations following a general equation of second-order shapes shown as Equation 2.1, in which x, y and z are coordinates of surface points and $f_i(x, y, z)$ is the function of a typical second-order shape. According to the calculated deviation values, each point is deviated in the direction of vertex normal to obtain the deviated geometry.

$$\delta(x, y, z) = \sum_{i=1}^{N} a_i f_i(x, y, z) \tag{2.1}$$

Common second-order shapes are cone, cylinder, paraboloid, ellipsoid and sphere, each corresponding to a different set of coefficients in Equation (2.1). The value of these coefficients can be determined according to experience. Figure 2.9 illustrates the variation of a nominal plane with four typical second order shapes.

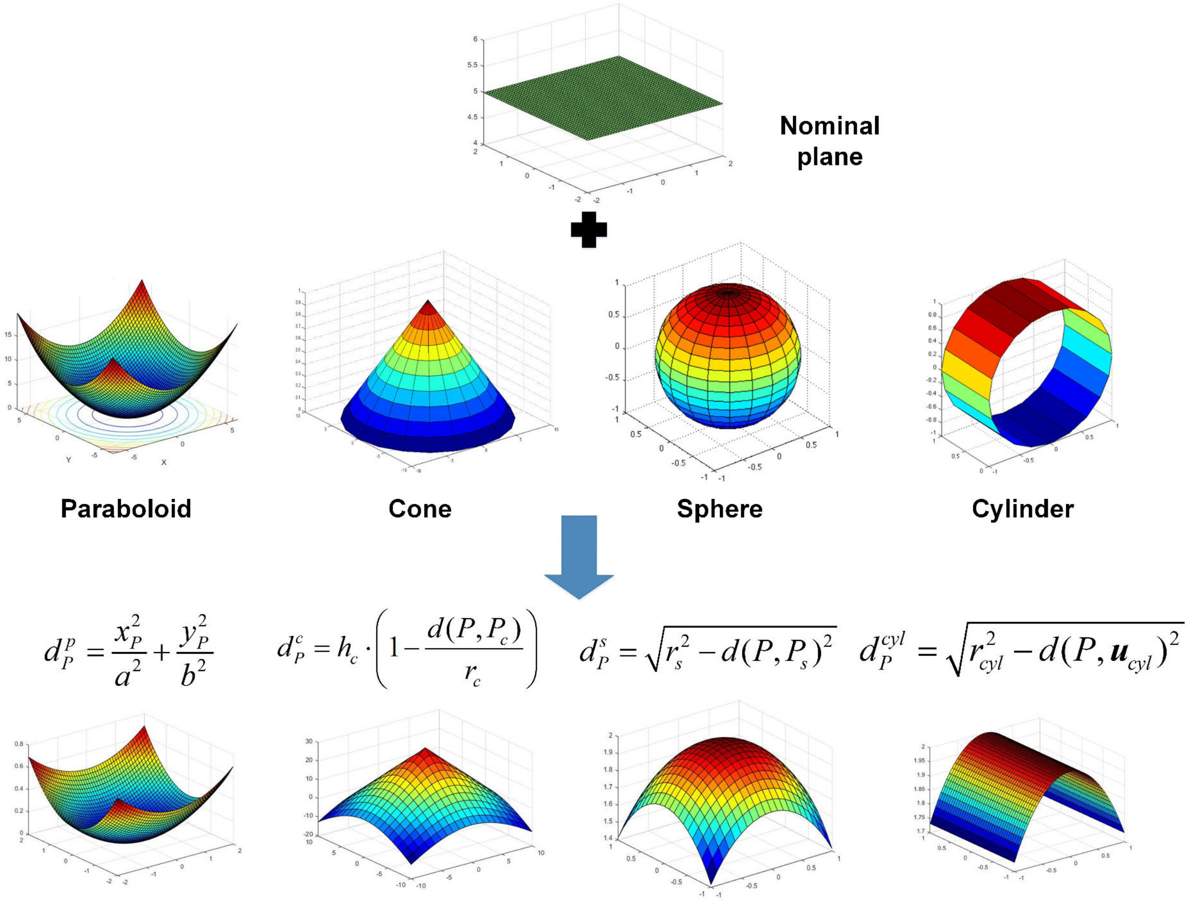

Figure 2.9: Variation of a nominal plane with typical second order shapes

Mode-based methods, such as Zernike polynomials [YB18a, ZLDS18] and Discrete Cosine Transform (DCT) [LZDS18], are also introduced to model systematic deviations of planar features. The Zernike polynomials are specifically used to represent typical form deviations of spherical or annular shapes with a combination of basis functions defined on the associated polar coordinate system (PCS), while the idea of DCT is to decompose the deviation of a rectangular planar feature into a set of cosine functions with varying spatial frequencies. Figure 2.10 illustrates a subset of deviation modes identified by DCT. The basis functions with fixed functional forms reflect the systematic property of both methods. In practice, the weighted sum of a subset of basis functions is sufficient to represent the overall deviations, where the weighting coefficients can be determined from historical data through fitting algorithms. In this thesis, the DCT method will be involved in the study of out-of-plane deviation in AM.

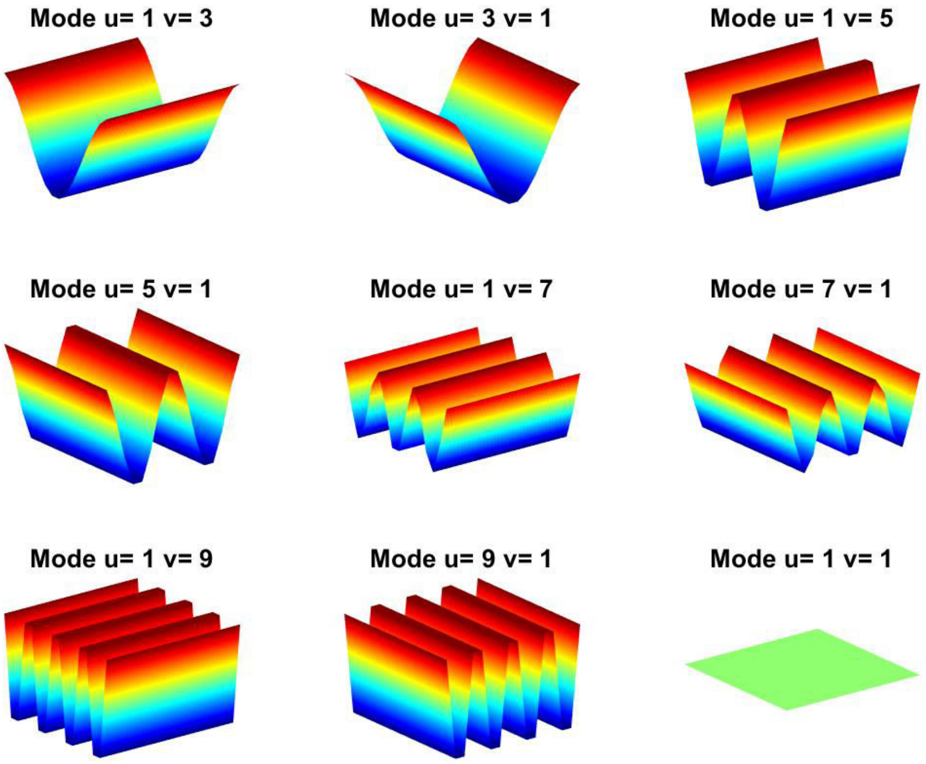

Figure 2.10: DCT modes identified from the deviation of a planar surface

Wu et al.[WQZA19] develop a new systematic deviation modeling method specifically for cylindrical features. The curvilinear coordinate system is adopted to represent the nominal cylindrical surface and a deviation dimension is added along the vertex normal of the surface to model the associated deviations. Taking into account typical errors in the machining process, Hermite polynomials and Fourier Series are combined to achieve a unified expression of deviations.

$$\delta(z,\theta) = \sum_{i=0}^{u} H_i(z)[\sum_{j=0}^{v} a_{ij}cos(j\theta) + \sum_{j=0}^{v} b_{ij}sin(j\theta)] \tag{2.2}$$

As shown in Equation 2.2, δ is the deviation of the non-ideal surface, $H_i(z)$ is the Hermite polynomial as a function of the height z and u is its order, a_{ij}, b_{ij} and v are the coefficients and order of Fourier series. Therefore, the deviated position of a point on the cylindrical surface can be represented in the curvilinear coordinate system as

$$r(z,\theta) = r_0 + \delta(z,\theta), \tag{2.3}$$

where r_0 is the nominal radius of the cylindrical feature. This combined Hermite-Fourier polynomial can be flexibly customized in a matrix form to represent multiple patterns of geometric deviations introduced by the manufacturing process, such as cutting force error, spindle motion error, fixture error, error caused by tool wear and thermal factors, etc. Figure 2.11 illustrates three kinds of systematic deviations in the manufacturing process of a cylindrical feature modeled by the proposed method.

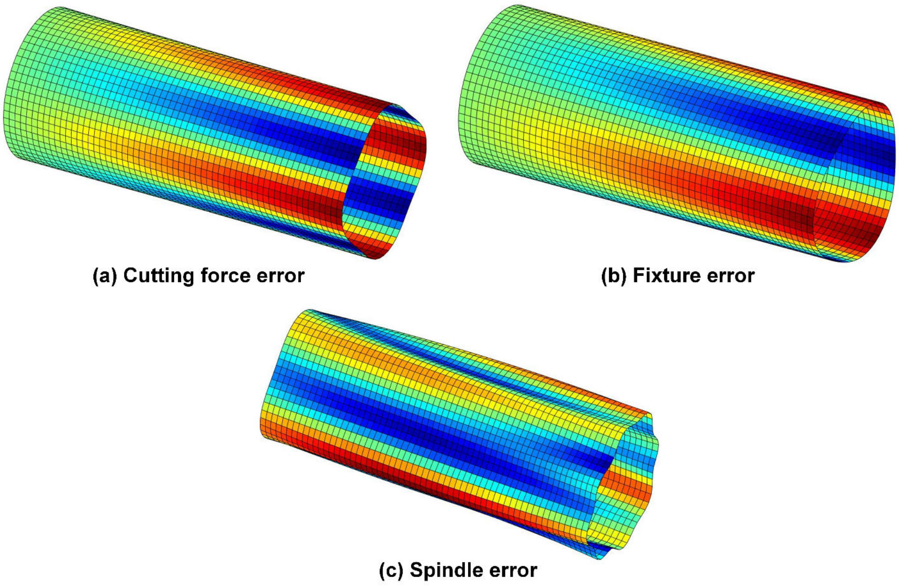
(a) Cutting force error

(b) Fixture error

(c) Spindle error

Figure 2.11: Three kinds of systematic deviations modeled by the Hermite-Fourier polynomials

In the Cartesian Coordinate System (CCS), Homri et al. [HGLD17] develop a Metric Modal Decomposition (MMD) method for form defect modeling of cylindrical parts. Three classes of modes are identified as rigid mode, rippled mode and mode of section. The functional forms of the modes are developed and their applications in assembly simulation and tolerance analysis are discussed.

Modeling random deviations

The modeling of random deviations have been investigated using several statistical methods, among which the 1D Gaussian distribution, multi-Gaussian distribution and Gibbs sampling methods were proposed by Zhang et al. [ZAMZ11] based on the hypothesis that the random deviations follow Gaussian distributions. The 1D Gaussian method is to randomly generate a deviation value in the vertex normal of each point following a univariate Gaussian distribution $d \sim N(\mu, \sigma^2)$ centered at the nominal point position. The variance of the distribution is set to control the magnitude of the generated deviation. While the 3D Gaussian method is to simultaneously generate deviations in the x, y and z directions following a tri-variate Gaussian distribution $\boldsymbol{d} \sim N(\boldsymbol{\mu}, \Sigma)$. Figure 2.12 illustrates the principle of these two methods. Instead of independently sampling random deviations for each point, the Gibbs method allows sequential sampling of deviations from the joint probability distribution of the whole point set based on Markov Chain Monte Carlo (MCMC) algorithms.

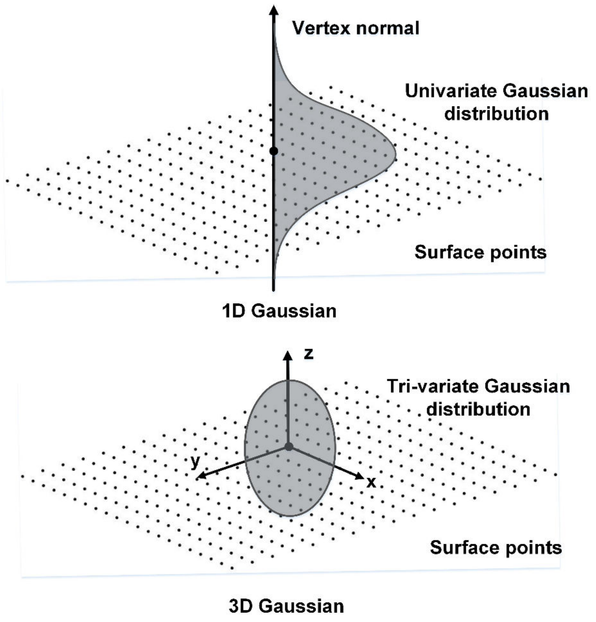

Figure 2.12: Principle of the 1D Gaussian and 3D Gaussian method [ZAMZ11]

It should be noted that the above-mentioned methods model random deviations in a point-wise manner, while overlooking the spatial correlation between points, which may cause inconsistency in the resulting shape, especially when large differences occur in the deviations of adjacent points. To overcome this weakness, the random field method that has been widely used in geology and earth sciences to sample spatially correlated random variables is adopted by [SAMW14]. A random field can be seen as a generalized stochastic process with multi-dimensional input variables (e.g. Cartesian coordinates). Through discretization, an approximation of the random field can be expressed as:

$$\boldsymbol{\delta}(\boldsymbol{x}) = \boldsymbol{\mu} + \boldsymbol{\sigma} \cdot \boldsymbol{M} \cdot \boldsymbol{N}^{\mathbf{1/2}} \cdot \boldsymbol{\varepsilon}, \tag{2.4}$$

where $\boldsymbol{\mu}$ and $\boldsymbol{\sigma}$ are the mean value vector and standard deviation matrix of the random field; $\boldsymbol{N}$ and $\boldsymbol{M}$ are matrices composed of the k largest eigenvalues and their corresponding eigenvectors of an auto-correlation matrix $\boldsymbol{C}$; $\boldsymbol{\varepsilon}$ is a vector of random variables following the standard normal distribution. $\boldsymbol{C}$ is determined by

$$\boldsymbol{C}_{ij} = se_{ij} = e^{\left(\left\|\boldsymbol{x_i} - \boldsymbol{x_j}\right\|^2 / l_\rho{}^2\right)} \tag{2.5}$$

, where se_{ij} is the squared exponential correlation function defined between two points $\boldsymbol{x_i}$ and $\boldsymbol{x_j}$; l_ρ is the correlation length to determine the strength of correlation and could be calibrated through analysis of experimental data. Similarly, the calculated random deviations are incorporated by deviating points in the nominal geometry in the vertex normal direction. Figure 2.13 shows four sample SMSs of a planar surface generated using the random field method.

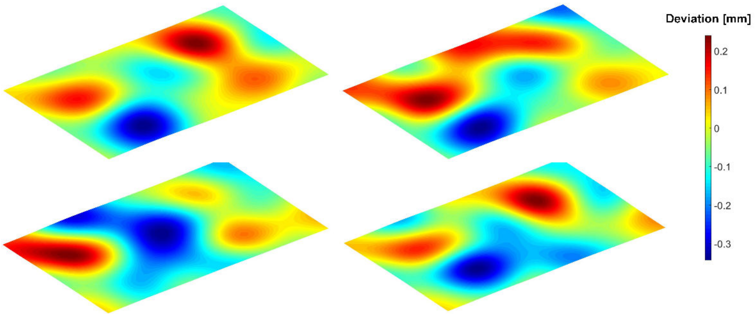

Figure 2.13: Samples of a planar surface generated with random fields [SWW+12]

2.3.3.2 Modeling deviations in the observation phase

In the observation phase, based on a training set consisting of sample shapes gathered from measurement data or manufacturing process simulation results, the objective of deviation modeling is to conduct statistical shape analysis (SSA) on the training set and establish a statistical shape model (SSM) that could analyze the statistical distribution of points on the sample shapes and therefore generate new samples following the deduced distribution. To achieve this goal, an SSM that combines Kernel Principal Component Analysis (KPCA), Kernel Density Estimate (KDE) and the Point Distribution Model (PDM) has been developed by [SAMW14]. Following the idea of PDM, each shape $\boldsymbol{X}_i, i = 1, \cdots, n$ in the training set is represented by a mean shape $\overline{\boldsymbol{X}} = \sum_{i=1}^{n} \boldsymbol{X}_i / n$ combined with variation of the shape around the mean shape along multiple main variation modes $\boldsymbol{\phi}$:

$$\boldsymbol{X}_i \approx \overline{\boldsymbol{X}} + \boldsymbol{\phi} \boldsymbol{s}_i. \tag{2.6}$$

, in which $\boldsymbol{\phi}$ are identified by applying KPCA and $\boldsymbol{s}$ are scores of the modes whose distribution can be estimated using KDE. Therefore, new SMSs can be generated by sampling new scores from their distribution through inverse transform sampling. The new samples also imply the consideration of systematic and random deviations, which are embodied in the mean shape and variation modes respectively. Figure 2.14 illustrates the SSA process. In this thesis, a new PDM-based statistical method will be discussed in the modeling of ot-of-plane deviation.

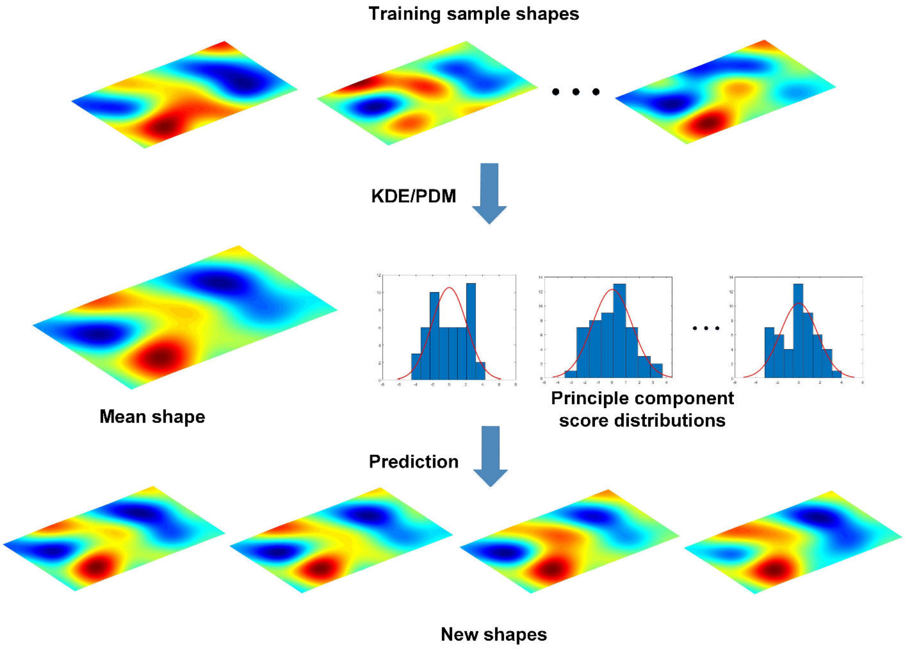

Figure 2.14: The statistical shape analysis process [SWW+12]

Another FEA-based approach has been proposed in [LB17], in which an SMS of a surface feature is developed from a small number of measured discrete sample points obtained from coordinate metrology. Based on the sampled points, a best substitute geometry of the feature is fitted following the least-squares principle. Thereafter, the geometry is parameterized and the deviations of sampled points from the geometry are calculated by comparing with their nearest corresponding points on the geometry, thus forming a 3D parameter space $\boldsymbol{u}, \boldsymbol{v}, \boldsymbol{d}$, where $\boldsymbol{u}, \boldsymbol{v}$ are parameters defining the substitute geometry and $\boldsymbol{d}$ denotes the deviations. An iso-parametric finite element modeling method is then used to resolve a continuous function of the manufacturing errors which enables to propagate the geometric deviations of sample points to the whole surface. The output of the method is an SMS that preserves the deviation patterns, and the function can be reused for prediction purposes for new manufactured parts. The weakness of this approach, however, is the lack of statistical insight on the measured deviations, which may hinder its application due to generalization issues.

2.3.4 Engineering applications of the Skin Model Shapes

The generated SMS are the building blocks for different engineering applications. The non-ideal product shape conveyed by the SMS has numerous advantages over the nominal shape. In this section, the current applications of SMS will be discussed.

2.3.4.1 Tolerance modeling

The generation of SMSs using the deviation modeling methods introduced in the previous section didn't take the dimensional and geometrical specifications into account. As a consequence, invalid SMS samples may be yielded that violate the design intent. Therefore, before applying SMSs for downstream applications, especially tolerance analysis, the generated samples need to be evaluated with respect to the tolerance design and modifications need to be performed on invalid ones. A general guideline for this process has been indicated in [SW15b] as:

- If a datum reference frame (DRF) exists, determine the associated least-squares feature of each non-ideal datum feature.
- Compute the tolerance zone of the toleranced non-ideal feature according to the tolerance type. If a DRF exists, the computation is done with respect to the associated features derived in the previous step.

- Compare the size of the tolerance zone with the specified tolerance value. If the specification is violated, either drop the current sample and redraw a new valid sample [SAMW14], or scale the geometric deviation of the toleranced feature until the specification is respected [SW15b].

The exhaustive 'drop-and-redraw' process would be time-consuming and computationally intensive for large-scale SMS. Therefore, the scaling operation is preferable due to its ability to preserve the deviation patterns while ensuring the conformance to specification. The actual scaling operation differs when it comes to different tolerance types. For form tolerance, scaling is to proportionally reduce the deviation values as projected to the associated feature. For orientation tolerance, scaling is to find an appropriate quantity of rotation of the toleranced feature such that the rotated feature shall lie within the tolerance zone. And scaling for position tolerance should consider both optimal translation and rotation of the toleranced feature. Since all the scaling methods are actually based on affine transformations of the non-ideal toleranced feature, the intrinsic characteristics of deviations stay unaffected.

Different evaluation and scaling methods have been developed for dimensional and geometrical tolerances following the guideline. Figure 2.15 illustrates the evaluation of tolerance zones of three types of tolerances.

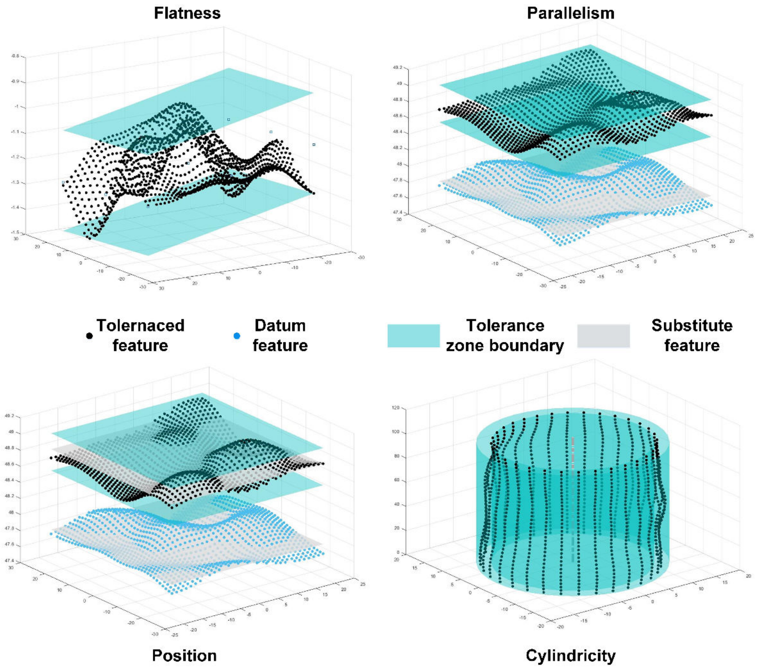

Figure 2.15: Evaluation of tolerance zone for four types of tolerances

2.3.4.2 Assembly simulation

The nominal CAD product model has been extensively adopted in mainstream CAD systems for assembly simulation. However, the effect of geometric deviations on the assemblability and functionality of the final product is non-trivial [SAMW15]. Minor deviations on components may be accumulated and propagated to the key characteristics, resulting in large discrepancies from the functional requirement. Therefore, the use of SMS in assembly simulation will enable the designer to gain an insight of possible outcomes of such effects.

The investigation on assembly of SMSs was initiated in [SAMW15]. Since SMSs are represented as point clouds or surface meshes, the assembly of two SMSs can actually be formulated as the registration of two sets of points belonging to mating features of the SMSs, in which one is denoted as the reference feature that stays still and the other is the target feature to be positioned relative to the reference. Two major constraints should be satisfied when implementing the registration algorithm: the distance between any corresponding point pairs on the two features should be minimized, and the two point sets shall not interpenetrate each other.

Following this principle, a constraint registration algorithm is proposed in [SAMW15, SW15a, SW18]. This algorithm aims at finding an optimal rigid-body transformation of the target feature $\boldsymbol{S}_a$ to best fit with the reference feature $\boldsymbol{S}_b$ while ensuring non-interference between the features. A transformation vector is defined as $\boldsymbol{\alpha} = (\boldsymbol{\alpha}_t, \boldsymbol{\alpha}_r)$, where $\boldsymbol{\alpha_t}, \boldsymbol{\alpha_r} \in R^3$ are the translation and rotation vectors defined with respect to the coordinate system origin and axes respectively. Suppose $\boldsymbol{S}'_a$ is the transformed target feature given $\boldsymbol{\alpha}$, it can be derived that $\boldsymbol{S}'_a = q(\boldsymbol{\alpha}, \boldsymbol{S}_a) = \boldsymbol{S}_a + \boldsymbol{\alpha_t} + \boldsymbol{\alpha_r} \times \boldsymbol{S}_a$. With this goal, an optimization problem is formulated as Eqn.(2.7), where $f(\cdot)$ is the objective function to be minimized and $g(\cdot)$ is the constraint function.

$$\begin{aligned} &\min_{\boldsymbol{\alpha}} f(\boldsymbol{\alpha}; \boldsymbol{S}_a, \boldsymbol{S}_b) \\ &s.t. g(\boldsymbol{\alpha}; \boldsymbol{S}_a, \boldsymbol{S}_b) \leq 0 \end{aligned} \tag{2.7}$$

Several metrics exist for the choice of the objective function, including Hausdorff distance, sum of squared distance, sum of signed and unsigned distance, etc., among which the sum of absolute signed normal distance metric has been validated in [SW18] as a practical choice specifically for this purpose. This metric measures the sum of absolute signed distance between one point $q(\boldsymbol{\alpha}, \boldsymbol{p}_a), \boldsymbol{p}_a \in \boldsymbol{S}_a$ on the transformed target feature and its corresponding point $\boldsymbol{p}_b$ on the reference feature $\boldsymbol{S}_b$ as projected on the normal $\boldsymbol{n}_{\boldsymbol{p}_a}$ of $\boldsymbol{p}_a$, as shown in Equation 2.8. Figure 2.16 provides a 2D illustration of this metric.

$$f(\boldsymbol{\alpha}; \boldsymbol{S}_a, \boldsymbol{S}_b) = \sum_{\boldsymbol{p}_a \in \boldsymbol{S}_a} |(q(\boldsymbol{\alpha}, \boldsymbol{p}_a) - \boldsymbol{p}_b) \cdot \boldsymbol{n}'_{\boldsymbol{p}_a}| \tag{2.8}$$

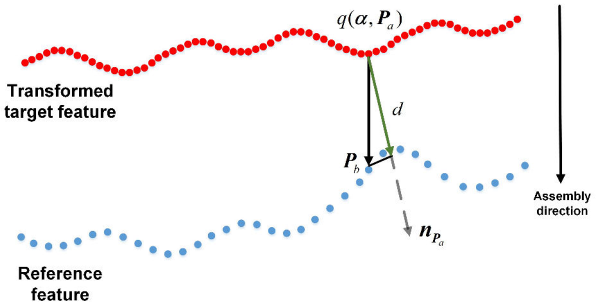

Figure 2.16: The absolute signed distance metric used in the objective function

The non-interference constraint can be interpreted as a set of inequalities ensuring that the aforementioned signed distance holds a negative value for each corresponding point pairs, as seen in Equation 2.9.

$$\forall \boldsymbol{p}_a \in \boldsymbol{S}_a, g(\boldsymbol{\alpha}; \boldsymbol{S}_a, \boldsymbol{S}_b) = (q(\boldsymbol{\alpha}, \boldsymbol{p}_a) - \boldsymbol{p}_b) \cdot \boldsymbol{n}'_{\boldsymbol{p}_b} \leq 0 \tag{2.9}$$

A prerequisite for both the objective function and the constraints is to determine the correspondences between points of the two features. Dynamic calculation of the correspondence during each iteration of the optimization process may be computationally costful, therefore, it is determined at a pre-defined relative position of two features. For each $\boldsymbol{p}_a$ of the target feature, the point on $\boldsymbol{S}_b$ with minimum projected distance on $\boldsymbol{n}_{\boldsymbol{p}_a}$ is deemed as its corresponding point, as shown in Equation 2.10.

$$\begin{gathered} \forall \boldsymbol{p}_i \in \boldsymbol{S}_b, \boldsymbol{p}_b = \boldsymbol{p}_j, \\ j = \arg\min_i(||(\boldsymbol{p}_i - \boldsymbol{p}_a) \cdot \boldsymbol{n}_{\boldsymbol{p}_a}||^2) \end{gathered} \tag{2.10}$$

An intuitive difference surface method is also proposed in [SW15a, SW18]. The difference surface $\boldsymbol{S}$ of two mating features is defined at x- and y- coordinates of the target feature points as the distances between each pair of corresponding points projected on the assembly direction $\boldsymbol{\omega}$, namely $\boldsymbol{S} = (\boldsymbol{x}_{\boldsymbol{S}_a}, \boldsymbol{y}_{\boldsymbol{S}_a}, \boldsymbol{d})$. The idea of this method is quite straightforward: the final contact position of the target feature should be the position where the convex hull of $\boldsymbol{S}$ intersects the driving assembly force imposed on a point $\boldsymbol{p}_a$

of $\boldsymbol{S}_a$ in the assembly direction. Finding the intersection triangle on the convex hull and registering points of $\boldsymbol{S}_a$ to the triangle vertices, the final target feature position is determined. It should be mentioned that, in the discussion of both methods, the registration has been conducted on mating features, the derived rigid-body transformation effects, however, are actually applied on the whole SMS where the features are associated in order to achieve the positioning of parts.

A similar approach has been adopted in [LZDS18] which treats the assembly of two non-ideal features as the assembly of a rigid perfect feature and the difference surface established from these features, as can be seen in Fig. 2.17. Instead of considering the difference surface as a rigid body in [SW15a], the local surface deformations along the assembly direction is modeled by the Boundary Element Method. Under the assumption of frictionless non-adhesive contact, physical properties including assembly force and material elasticity, are incorporated in the assembly model and the elastic displacement (the displacement is assumed in the z-direction here) of the discrete points can be calculated as:

$$u_{i,j} = \sum_{k=1}^{M} \sum_{l=1}^{N} K_{i-k,j-l} p_{k,l} \tag{2.11}$$

, where M and N represent the number of discrete points in x- and y- directions respectively; p is the contact force on each discrete point; and K denotes the matrix that collects the influence coefficients, which can be calculated as:

$$\begin{aligned} & K_{f,g} \\ & = \frac{2}{\pi E'}[y_m \log(x_m + \sqrt{x_m^2 + y_m^2}) + x_m \log(y_m + \sqrt{x_m^2 + y_m^2}) \\ & - y_m \log(x_p + \sqrt{x_p^2 + y_m^2}) - x_p \log(y_m + \sqrt{x_p^2 + y_m^2}) \\ & - y_p \log(x_m + \sqrt{x_m^2 + y_p^2}) - x_m \log(y_p + \sqrt{x_m^2 + y_p^2}) \\ & + y_p \log(x_p + \sqrt{x_p^2 + y_p^2}) + x_p \log(y_p + \sqrt{x_p^2 + y_p^2})] \end{aligned} \tag{2.12}$$

, where $x_m = x_f + \Delta x/2$, $x_p = x_f - \Delta x/2$, $y_m = y_g + \Delta y/2$, $y_p = y_g - \Delta y/2$, Δx and Δy represent the distance between two adjacent discrete points in the x- and y- directions; E' denotes the effective composite elastic modulus, and can be obtained by:

$$\frac{2}{E'} = \frac{1-\nu_1^2}{E_1} + \frac{1-\nu_2^2}{E_2} \tag{2.13}$$

, with E_1 and E_2 being the Young's moduli of elasticity and ν_1 and ν_2 being the Poisson's ratios for the two contacting non-ideal features.

To ensure that there is no penetration between the two surfaces and the discrete points do not bear negative forces, the following restrictions should be fulfilled:

$$\begin{cases} c_{i,j} \leq 0, p_{i,j} \leq 0 \\ \quad c_{i,j} p_{i,j} = 0 \end{cases} \tag{2.14}$$

, where $c_{i,j}$ represents the gap distance between the corresponding points on the two surfaces, and it is determined by $u_{i,j}$; $p_{i,j}$ represents the contact force on each point. Based on the principle of minimizing the total complementary potential energy, the calculation of a contact problem can be transformed into a quadratic programming problem, which can be expressed as:

$$\begin{aligned} &\min W(\boldsymbol{p}) = \boldsymbol{c}^T \boldsymbol{p} + \boldsymbol{p}^T \boldsymbol{K} \boldsymbol{p}/2 \\ &s.t. \quad c_{i,j} \leq 0, p_{i,j} \leq 0, c_{i,j} p_{i,j} = 0 \end{aligned} \tag{2.15}$$

Comparing with FEA calculation, BEM is far more efficient while ensuring the calculation accuracy. The interactions between SMS and local surface deformations hence provide a novel strategy for non-rigid assembly simulation.

In order to tackle more complex assembly structures involving multiple components and physical effects from internal and external loads, an improved assembly simulation approach is proposed in [YB18b]. As a complement to the non-interference constraint considered in previous works, the internal reaction forces, external forces and torques as well as the balance of internal and external loads are newly added as boundary conditions.

2.3.4.3 Tolerance analysis

Traditional Computer-Aided Tolerancing (CAT) systems rely on nominal CAD models and ignore the effects of form deviations [ASG+07], which doesn't fully conform to GD&T standards [SAZ+14] and may give unrealistic results. In this context, tolerance analysis based on SMSs offers the potential to gain more reliable results.The research in assembly of SMSs lays a solid foundation for the downstream application on tolerance analysis [LZDS18, YB18b, SW15a, SW18, ZQA16]. A three-stage tolerance analysis routine is developed in [SAMW15] as:

- *Pre-processing.* Following the methodologies explained in Section 2.3.3, SMSs are

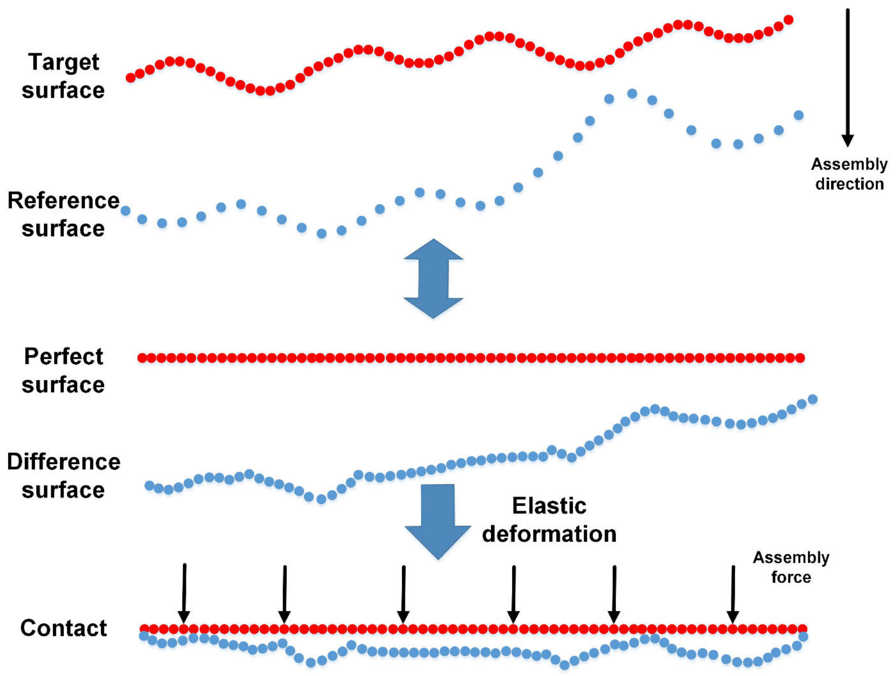

Figure 2.17: The difference surface considering assembly force and material elasticity

generated for each part of the assembly to be analyzed. The generated SMSs are checked with respect to the tolerance specifications, and due scaling or re-drawing operations are conducted to gather a given number of valid assembly samples.

- *Processing.* Guided by the predefined assembly process plan, the SMSs of parts in each assembly sample are assembled using the simulation techniques explained in 2.3.4.2.

- *Post-processing.* Given the final position of SMSs, the key characteristics (KCs), such as clearances, gaps or angles between features in concern, are evaluated for each sample. As a result, a sufficient number of KC values are obtained, from which statistical distribution is drawn and sensitivity analysis is done to provide significant information about the potential effects of the tolerances.

SMS has also been combined with other tolerance models to enhance their ability in dealing with form defects. The polytope is a classical 3D tolerance analysis method that represents the geometric, contact or functional specification with a set of constraints limiting the variation of a feature relative to the reference [HTB15]. Though the polytope-based method has demonstrated effectiveness in modeling the propagation of geometric variations, the fact that it lacks consideration of form deviations has motivated the effort to combine it with the SMS in [LPA+19]. Identifying all toleranced features in the assembly chain, the SMSs of these features are generated. Substituting the nominal features with non-ideal features conveyed by the SMS, modified polytopes are obtained and the Minkowski sum or intersection of these polytopes is calculated to derive the accumulated error at the KCs.

2.3.4.4 Challenges in extension of SMS to AM

As the name "Skin Model Shapes" suggests, current methods within the SMS framework focus on the deviation of the 'skin', namely the part surface, since the effects of manufacturing errors are directly reflected on the external surface in traditional subtractive manufacturing processes. Whereas in AM process, the deviations are actually an outcome of the accumulated deviation of each layer. For example, the undesired displacement of machine axes or energy sources, may cause slight shifting of the shape of the fabricated layer with respect to the machine coordinate system, and material shrinkage due to thermal effects may cause local variations of shape from its nominal form. The stack-up of these deviated shapes will undoubtedly overlay the deviations and as a result affect the overall product form. Moreover, the residual stresses may induce a warpage or deflection of the layers in the build direction, and the effect exhibits a decreasing tendency from bottom layer to top layer. Such issues pose new challenges to the extension of SMS to AM, motivating new methodologies to be developed shifting the current paradigm from part-level to layer-level, as illustrated in Figure 2.18. In the next section, a new deviation modeling framework will be introduced as an extension of current SMS framework with consideration of the new challenges.

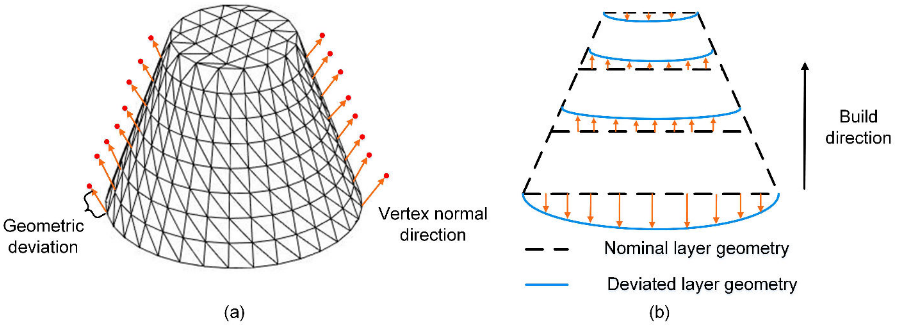

Figure 2.18: Deviation modeling from (a)part-level, (b)layer-level

2.4 New AM deviation modeling framework

In face of the new challenges, the classification of in-plane and out-of-plane deviation as mentioned in Section 2.2.3 is followed, thus reducing the 3D modeling problem to 2.5D. In-plane (x-y plane) deviation denotes transformation of the nominal 2D shape of the layer due to material behavior or machine errors. While the out-of-plane is to account for deformation of the in-plane shape toward the build direction. Figure 2.19 demonstrates these two types of deviation on one layer of the cylindrical part. It can be observed that the in-plane deviation causes contraction of the nominal circular shape to its center. The stack-up of layers will accumulate these deviations and as a result affect the form of side surfaces. The out-of-plane deviation captures the upward bending of the in-plane shape. This effect, after accumulation, will result in the overall curling of the part, especially at the top and bottom surfaces. Compared to those works dedicated to modeling of the global shrinkage factor which applies on the entire part [RP07, SPR09b, SPR12], this classification conforms to the layer-wise nature of AM processes and could facilitate local investigation of individual layers.

Figure 2.20 illustrates the general work-flow of the new SMS framework. To start with, the CAD part model is converted to an STL model, since it is the de-facto input format of most AM processes. To obtain the nominal shape of each layer, the STL is then sliced with a plane that is perpendicular to the build direction and located at corresponding layer heights. The result of the slicing procedure is a set of layer contour points. By connecting these points consecutively in counter-clockwise direction, the layer contour is reconstructed representing the nominal shape of the layer. The deviation models will be developed based on the nominal layer shapes.

According to the definition of in-plane deviation, it can be treated as the variation of the nominal 2D contour. In this regard, the PCS becomes a suitable choice for deviation representation, since it enables the formulation of 2D shapes as a single function. Empirical models proposed by existing works can be readily adopted for predicting in-plane deviations without process knowledge. Further, by analyzing observed deviation data, new models can be developed by mapping effects of error sources to the systematic transformation of the nominal shape. Moreover, statistical methods could be adopted to derive more reliable models from a number of manufactured samples.

Instead of the layer contour, the out-of-plane is more concerned with the variation

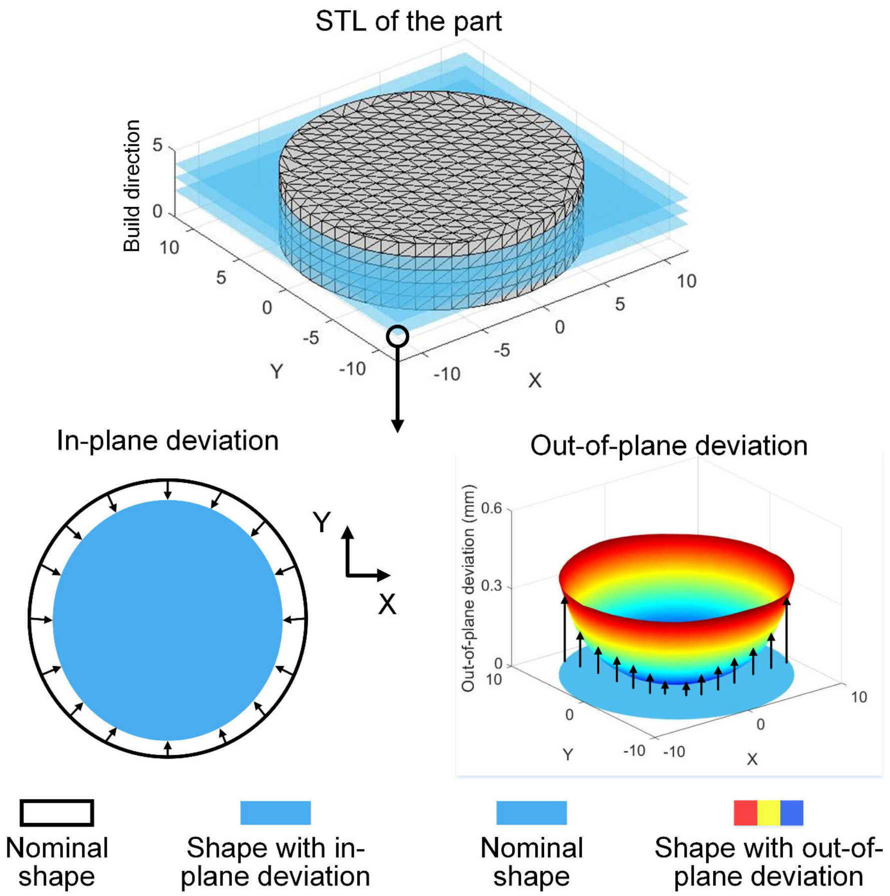

Figure 2.19: Illustration of in-plane and out-of-plane deviations of the shape of one layer

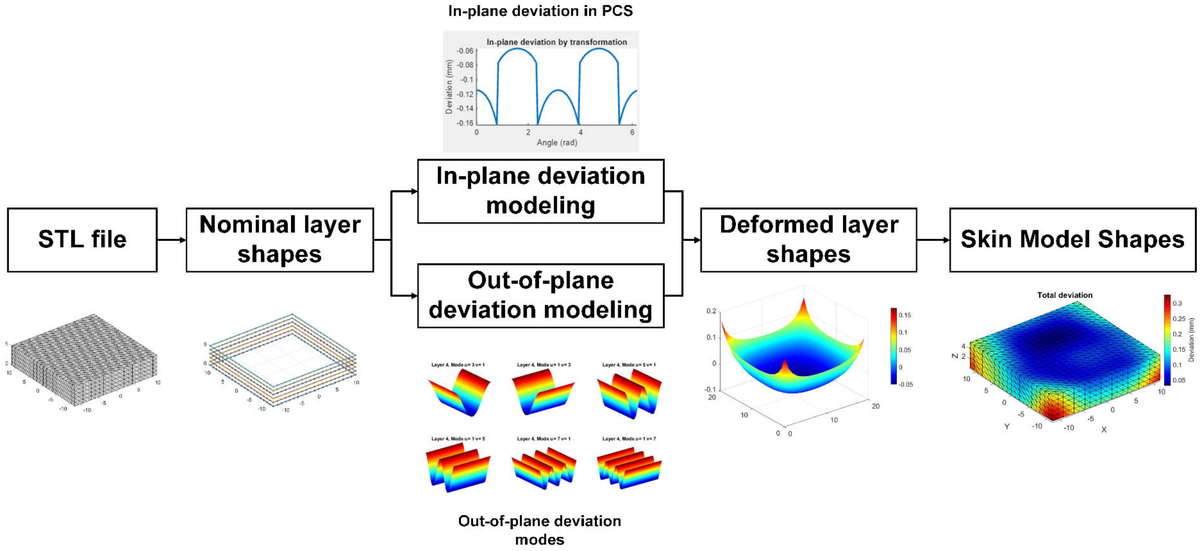

Figure 2.20: AM Deviation modeling framework based on SMS

of the whole internal layer geometry. Some research outcomes on the warpage or curling effects can provide a preliminary vision of the out-of-plane deviation at bottom and top layers. Through mesh deformation techniques, such as Free-form Deformation, the local deviations can be propagated to all the layers. Though the accuracy of such methods remains to be improved, they could be applied for deviation prediction when no process knowledge or manufactured samples are available. The deviations that occur on the internal layer shape of a manufactured part are difficult to obtain with common measurement devices. Hence, AM simulation becomes a preferable means of deviation data collection. To realize parameterization of out-of-plane deviation data gathered from simulation results at discrete points of each layer, modal analysis techniques can be used, which reduce the modeling problem to the characterization of some significant deviation modes. These modes inherently correspond to certain types of deviation patterns and their significance varies under different process conditions. Based on a number of simulated deviation data, through identification of deviation modes and prediction of their significance, the out-of-plane deviation of a layer can be effectively predicted.

In the modeling process of both types of deviations, the consideration of the prediction and observation stage is implicitly conveyed. The empirical models used for the early prediction of deviations correspond to the definition of prediction stage in SMS. While the statistical models are built with support of observation data gathered from measurement or simulation, thereby conforming to the observation stage in SMS. Meanwhile, the model structures are designed in consistency with the assumption of systematic and random deviations, as will be introduced in the following chapters.

Based on the derived deviation models, the nominal layer shapes are deformed. Whereas, the topological information is lost after slicing the surface model to independent layers. To reconstruct the surface, a layer connection strategy is used to find a triangulation plan between each pair of adjacent deformed layers. Finally, a new surface is generated incorporating both the in-plane and out-of-plane deviations, which represents an SMS of the part.

The general procedure of this framework is as follows: starting from the nominal product model consisted in the STL file, slicing is conducted with a given slice thickness to obtain the nominal shape of each 2D layer. This process differs from the traditional SMS in that the deviation modeling problem is now treated on separate layers instead of individual surface features. Thereafter, in-plane and out-of-plane deviation models are derived and used to deform the layer geometry. In this process, either empirical models can be used or new statistical models are proposed by learning from simulation and measurement data. The idea inherently involves the consideration of the prediction and observation stage, since empirical models are applied when no manufacturing data are available, while statistical models are built with support from observation data. Furthermore, the model structures are designed in consistency with the assumption of systematic and random deviations. The deformed layer geometries are finally consecutively connected to reconstruct a triangular mesh representing an SMS. The generated SMSs can be further developed for different applications as a realistic model of AM products. Figure 2.20 provides an illustration of the proposed framework. It inherits some key concepts of the existing SMS paradigm and covers the AM process chain.

2.5 Conclusion

Effective characterization of geometric deviations is the key to modeling SMS for AM. To facilitate understanding of the research problems in AM deviation modeling, existing methods are reviewed based on three main categories. The geometric approximation errors are studied by investigating the errors brought by conversion of the part geometry from the CAD model to the input model of the process. These methods are process-independent and can be applied prior to the manufacturing process. The study on machine errors and process parameters aims at capturing their effects on the resulting deviations through parametric functions. The findings suggest the significant contribution of some key process parameters in powder-bed based processes, including laser power, layer thickness and scan speed, thus providing the evidence for experimental design in this thesis. In some works related to modeling material-related shape deviations, the novel classification of in-plane and out-of-plane deviations is made, which is well suited to the layer-wise building strategy of AM and substantially motivates the new SMS framework developed in this thesis.

Driven by the demand for a comprehensive AM deviation modeling framework, the extension of SMS to AM is proposed. The traditional deviation modeling methods for generation of SMS are discussed, some of which are inherited in the new framework. The random field method enables the consideration of random deviations while maintaining the correlation between surface points. The SSA method is a powerful tool to identify the deviation modes among a set of manufactured samples. Though the new challenges in AM shift the modeling strategy from part-level to layer-level, these methods can be adaptively customized to model deviations on the layers.

The aim of this chapter is to provide the context and motivation for development of the SMS framework for AM. With all such background, a detailed explanation to the work-flow of the framework is made at the end of this chapter, which serves as the guideline for the following chapters.

Section 2.2 of this chapter is based on a published work included in *Advances on Mechanics, Design Engineering and Manufacturing* as a presentation in the *International Joint Conference on Mechanics, Design Engineering and Advanced Manufacturing* (JCM 2016) [ZKA+17].

Chapter 3

In-plane geometric deviation modeling for AM

Contents

3.1 Introduction

The modeling of in-plane deviations aims at capturing the variability of the 2D shape of each layer in AM processes. In order to provide an analytical formulation of the deviations, previous works have focused on deriving shape-dependent parametric functions based on the PCS established in 2D space, as reviewed in Section 2.2.3. In face of their weaknesses regarding transferability across shapes, in this chapter, new in-plane deviation methods will be discussed aiming at more general models that can be used independently from the specific in-plane shape. The PCS is still adopted since it facilitates the analytical representation of common 2D shapes with a single function.

Since in-plane deviation is defined as difference between the nominal input shape and the actual shape resulting from AM process, the modeling problem can be tackled by investigating the two shapes. The nominal shape of a layer can be obtained by slicing the STL model at the corresponding layer height and connecting the contour points to form a nominal contour. Similarly, the actual shape of each layer can be obtained either from AM simulation results or by slicing the triangulation of point clouds gathered from measurement data of manufactured samples. Therefore, in Section 3.2 of this chapter, methods that are dedicated to the parameterization of in-plane deviations are introduced and their respective characteristics are discussed. The weakness of these methods, however, is the large number of parameters needed to approximate the in-plane shape, which mitigates their performance on complex shapes. The shape-dependence of such methods also motivates the development of more general methods.

Therefore, to incorporate more consideration of process-related factors, a new shape transformation based method is proposed in Section 3.3. The effects of potential error sources are mapped to the transformation of the in-plane shape. Deviations are then parameterized with three kinds of transformation parameters in the PCS. The parameterization is investigated for different shapes, including simple cylindrical shapes and arbitrary polygonal shapes. The estimation of parameters is discussed based on the least-squares principle and a case study is presented to justify the validity of the transformation perspective.

Moreover, to account for the uncertainties in model estimation, a statistical learning method is presented in Section 3.4.1 which applies Bayesian inference to derive the distribution of each transformation parameter based on measurement data. The capability to provide both the mean prediction and the prediction interval enhances the transformation-based model in explaining the deviation data of more samples. Nevertheless, The local deviations along the shape boundary can hardly be captured by the transformation parameters that are derived for the global shape. Their patterns also vary among different shapes. To characterize these patterns and increase prediction performance, in Section 3.4.2, a multi-task learning model is added to the transformation-based model to enable simultaneous learning from deviation data of multiple shapes and improve the prediction performance for all shapes.

3.2 Parameterization of in-plane deviations

In this section, the parameterization of in-plane deviations is discussed in two ways: (1) parametrization of nominal and actual in-plane shapes and calculation of their difference, (2) analytical parametric modeling based on observed deviations. The former way is implemented using Fourier descriptors and Fourier series expansion in preliminary research, as introduced in Section 3.2.1 and 3.2.2. The latter way has been studied in several existing works using prescriptive methods for different shapes and will be briefly discussed in Section 3.2.3.

3.2.1 Fourier descriptors based method

For 2D shapes with closed contour, the Fourier Descriptors (FD) enable their parameterization with convenient and compact representations [ZL$^+$02]. Being invariant to rotation, translation and scaling, and less sensitive to the location and number of contour points, FDs have been extensively investigated in computer vision for shape recognition, classification and retrieval. In this research, FDs are used to describe the in-plane shape of AM products, and to derive a parametric representation of the shape deviations in 2D.

In the FD representation, a closed 2D shape is parameterized as a one-dimensional function known as the shape signature that uniquely defines the shape. Different signatures have been proposed including complex coordinates, centroid distance, contour curvature, etc. [ZL04], among which the cumulative bend angle signature is used in this research.

Given an arbitrary closed shape composed of m vertices $V_0, ..., V_{m-1}$ arranged in clockwise sequence, with the length of each arc (V_{i-1}, V_i) as Δl_i, then the change in angular direction at vertex V_i is $\Delta\varphi_i$, the total arc length is given by $L = \sum_{i=1}^{m} \Delta l_i$ and the elapsed arc length at V_i is $l = \sum_{i=1}^{k} \Delta l_i$, as illustrated in Figure 3.1. The shape signature is thereby defined as $\varphi(l) = \sum_{i=1}^{k} \Delta\varphi_i$ denoting the amount of angular bend between V_i and the starting point where $l = 0$ [PF77]. To obtain a desired periodic representation, we note that $\varphi(0) = 0$ and $\varphi(L) = 2\pi$, so a normalization can be done by replacing l as t, where t is the normalized elapsed arc length: $0 \leq t = 2\pi l/L \leq 2\pi$, and $\varphi^\star(t) = \varphi(Lt/2\pi) - t$.

Performing Fourier series expansion on $\varphi^\star(t)$ gives

$$\varphi^*(t) = \mu_0 + \sum_{n=1}^{\infty} (a_n \cos nt + b_n \sin nt) \tag{3.1}$$

It has been proved that parameters of a truncated form of the above Fourier series containing N terms can be derived as[ZR72]:

$$\begin{aligned}
\mu_0 &= -\pi - \frac{1}{L}\sum_{k=1}^{m} l_k \Delta\phi_k \\
a_n &= -\frac{1}{n\pi}\sum_{k=1}^{m} \Delta\phi_k \sin\frac{2n\pi l_k}{L} \\
b_n &= \frac{1}{n\pi}\sum_{k=1}^{m} \Delta\phi_k \cos\frac{2n\pi l_k}{L} \\
l_k &= \sum_{k=1}^{k} \Delta l_i, n = 1, .., N
\end{aligned} \tag{3.2}$$

The Fourier series can also be transformed into an amplitude/phase angle form as

$$\varphi^*(t) = \mu_0 + \sum_{n=1}^{\infty} A_n \cos(nt - \alpha_n)$$

by combining the trigonometric components, where $A_n = \sqrt{a_n^2 + b_n^2}$, $\alpha_n = \arctan(b_n/a_n)$. (A_n, α_n) are the FDs of the shape.

Based on the FDs, the parametric formulation can be obtained in the frequency domain for an arbitrary closed shape from just the coordinates of contour points. Whereas, in order to represent geometric deviations in the spatial domain, it is also important to know how to reconstruct the original shape from the FDs. A solution exists which

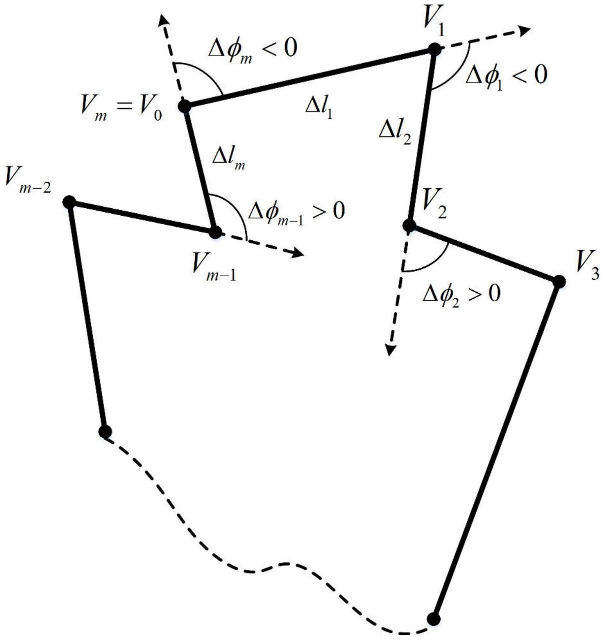

Figure 3.1: Description of a closed curve with respect to edge lengths and vertex bend angles [ZR72]

sufficiently approximates the original shape with N truncated components [ZR72]:

$$\mathrm{P}(l) = P(0) + \frac{L}{2\pi}\int_0^{2\pi l/L} \exp\{\mathrm{i}[-\mathrm{t}+\delta_0+\mu_0+\sum_{k=1}^{N} A_k \cos(kt-\alpha_k)]\}dt \tag{3.3}$$

, where the real and imaginary parts of $P(l)$ denote the x and y coordinates of the point at $l = Lt/2\pi$; $P(0), \delta_0, L$ are the specified starting point coordinates, initial direction and total arc length that should be carefully selected to ensure the reconstruction accuracy.

To use FDs to describe in-plane deviation, in a first step, both the nominal shape and manufactured shape are parameterized with FDs. Denote $FD^n = \mu_0^n, \{A_k^n, \alpha_k^n, k = 1, ..., N^n\}$ as the truncated FDs for the nominal shape obtained by slicing the STL file, and $FD^a = \mu_0^a, \{A_k^a, \alpha_k^a, k = 1, ..., N^a\}$ for the manufactured shape constructed from the observation data, in-plane deviation is defined as the distance between corresponding points on shapes reconstructed from FD^n and FD^a. These corresponding points $(P^n(l_i), P^a(l_i))$ are determined by sampling a series of t_i from the range $[0, 2\pi]$ and inputting $l_i = Lt_i/2\pi$ to Equation 3.3 together with the respective FDs. Based thereon, the deviation is defined as

$$d(t_i) = |P^n(l_i) - P^a(l_i)| \tag{3.4}$$

, note that $P^n(l_i)$ and $P^a(l_i)$ are complex numbers conveying the coordinates of nominal shape points and manufactured shape points respectively.

The challenges of FDs are also worth mentioning. The shape reconstruction procedure inevitably introduces errors that are subsequently confused with the calculated deviations. Therefore, a larger number of truncation terms are required to minimize the reconstruction error, which in turn increases the number of FD parameters. The selection of starting point for Equation 3.3 is also non-trivial, since the correspondence between points of two shapes is established along the shape boundary from their respective starting point. For regular shapes, identifiable features such as corner points can be used as the starting point, while for more complex shapes, registration techniques may be needed. Moreover, the function in Equation 3.4 only provides the deviation as a scalar. When applying this function to predict deviations for a new shape, it is also necessary to know the direction in which the deviation is applied, a provisional solution is to use the tangent normal of shape points.

3.2.2 Fourier-series expansion (FSE) based method

The FD-based method enables the parameterization of in-plane shape in the CCS, however, the representation is not intuitive owing to the fact that a mapping from the frequency domain to spatial domain is required. For closed convex shapes, a more straightforward means is to adopt the PCS and describe the radius of shape as a single function of the polar angle. By translating the nominal and actual shapes into a common PCS, the in-plane deviation is then defined as their radial difference as shown in Equation 3.5 and Figure 3.2.

$$\Delta r(\theta) = r(\theta) - r^{\circ}(\theta) \tag{3.5}$$

$r^{\circ}(\theta)$ is known from the nominal shape, the actual shape function $r(\theta)$ can be further represented as a truncated Fourier series expansion as:

$$r(\theta) = a_0 + \sum_{k=1}^{M} \left[a_k \cos(k\theta) + b_k \sin(k\theta)\right] \tag{3.6}$$

In Equation 3.6, a_0, $\{a_k, b_k, k = 1, ..., M\}$ are shape parameters that can be estimated from observation data. A reasonable choice of M could enable a close approximation to the original shape. Combining Equation 3.5 and 3.6, $\Delta r(\theta)$ can be represented in a polar form as seen in Equation 3.7, in which ϵ_θ is an extra term to account for the

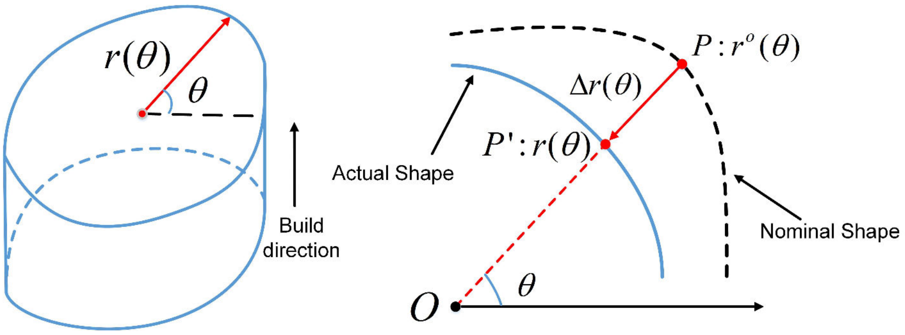

Figure 3.2: In plane shape and in-plane deviation

random noise in deviation data.

$$\begin{aligned}\Delta r(\theta) &= a_0 + \sum_{k=1}^{M} A_k \cos(k\theta - \alpha_k) - r^{\circ}(\theta) + \epsilon_\theta \\ A_k &= \sqrt{a_k^2 + b_k^2}, \alpha_k = \arctan(b_k/a_k)\end{aligned} \tag{3.7}$$

This method provides a continuous representation of in-plane deviation in the PCS and could serve as an empirical deviation model for parts manufactured under the same or similar process conditions. In essence, the Fourier series is a combination of continuous trigonometric terms with varying frequencies, so it is well suited for smooth shapes, for instance, circles. When it comes to a polygonal shape whose radius in the PCS illustrates drastic changes at corner points, more high-frequency terms need to be introduced, thus increasing the model complexity.

3.2.3 Prescriptive analytics

The modeling of in-plane deviation has been extensively investigated by Huang et al. for quality control of different AM processes [HNX$^+$14a, HZSD15b, LH15, Hua16, LH17]. In a series of publications, statistical methods have been adopted to derive predictive in-plane deviation models for shapes ranging from basic cylindrical shapes to complex free-form shapes. In this subsection, a review of such methods will be made as a background for our proposed method. The primary goal of Huang's research is to derive optimal compensation plan on the CAD product model based on analytical in-plane deviation models through analysis of measurement data. For a cylindrical shape manufactured by the Stereolithography (SLA) process, an empirical deviation function is given as

Equation 3.8 in the PCS, in which r^o is the radius of the cylindrical shape [Hua16].

$$f_{cyl}(\theta, r^{\circ}(\theta)) = \beta_0(r^{\circ})^{a_0} + \beta_1(r^{\circ})^{a_1}cos(2\theta) \tag{3.8}$$

An intuitive cookie-cutter based method has been used to extend the deviation function of cylindrical shape to regular polygonal shapes, based on the observation that the deviation profile of a manufactured polygonal shape shows sharp transitions in PCS at the corner points. The idea of cookie-cutter is to treat a polygon as a portion of its circumcircle that can be precisely cut off by designing a cookie-cutter function. Two kinds of such functions have been defined [HNX+14a]:

- *Square wave function.* A square wave is a non-sinusoidal periodic waveform whose amplitude varies with a constant frequency between fixed minimum and maximum values while keeping the same duration at these values. In order to use the square wave function to cut a given polygon off its circumcircle, the period of the function should be set according to the number of edges of the polygon. Therefore, for a polygon with n edges, the function is given as:

  $$c_{wav}(\theta) = sign[cos(n(\theta - \phi_0))/2] \tag{3.9}$$

  , where $sign[\cdot]$ is a sign function, and ϕ_0 is a shifting variable that denotes where the first sharp transitions take place in the PCS and is determined as the smallest angular distance between a polygon vertex and the PCS axis in counterclockwise direction.

- *Saw tooth function.* In a similar manner, the saw tooth function is defined as:

  $$c_{saw}(\theta) = (\theta - \phi_0)mod(2\pi, n) \tag{3.10}$$

  , where $mod(\cdot, \cdot)$ is the modulo operator. Figure 3.3 illustrates a regular hexagon shape and the corresponding square wave function as well as saw tooth function derived from the shape.

Based thereon, the deviation function of a polygonal shape is given as the combination of the cylindrical shape deviation function and an appropriate cookie cutter function:

$$\begin{aligned} f_{pol}(\theta, r^{\circ}(\theta)) &= g_1(\theta, r^{\circ}(\theta)) + g_2(\theta, r^{\circ}(\theta)) \\ &= f_{cyl}(\theta, r^{\circ}(\theta)) + \beta_2(r^{\circ})^{a_2}c(\theta) \end{aligned} \tag{3.11}$$

, here r° is the circumcircle radius of the polygon and $c(\theta)$ is properly chosen between $c_{wav}(\theta)$ and $c_{saw}(\theta)$ or as a combination of the two according to observation of the deviation profile.

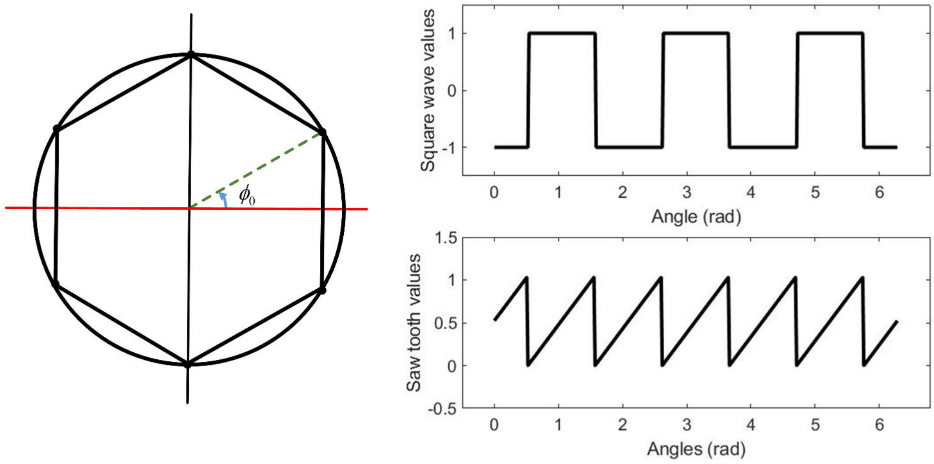

Figure 3.3: Hexagon shape and the corresponding cookie cutter functions

This methodology has been further developed for freeform shapes using a Circular Approximation with Selective Cornering (CASC) strategy [LH17]. The strategy is to approximate the freeform shape with multiple small sectors that share the common PCS origin, each of which has a distinct radius $r_i(\theta_i)$, and the deviation at each sector is represented with Equation 3.8. Since the radii of sectors are mutually different, sharp transitions may be observed between adjacent sectors. These transitions are captured along the shape boundary at corner points where the shared line between two adjacent sectors intersects with the shape. Thereafter, the transitions can be modeled in the same way as the polygon case. Figure 3.4 illustrates the CASC strategy.

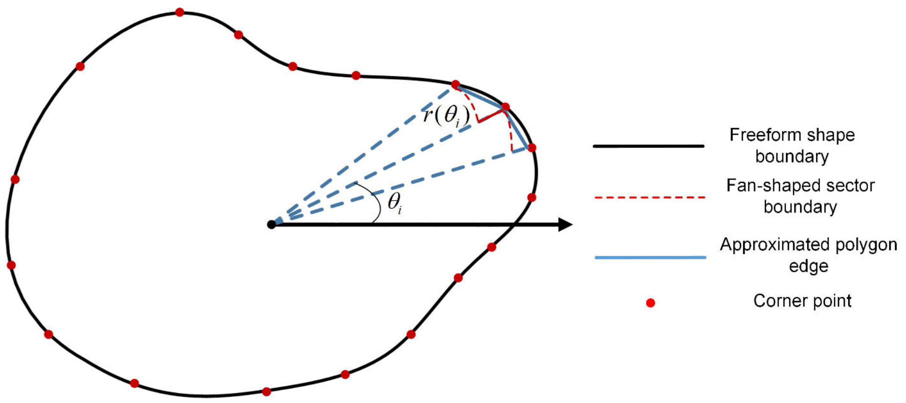

Figure 3.4: The CASC strategy for freeform shape deviation modeling

Following the CASC strategy, the deviation function of a freeform shape is similarly given with two components: $g_1(\cdot,\cdot)$ and $g_2(\cdot,\cdot)$, in which $g_1(\cdot,\cdot)$ is reformulated as:

$$\begin{aligned} g_1(\theta, r^{\circ}(\theta)) = \beta_0(r_i(\theta_i))^{a_0} + \beta_1(r_i(\theta_i))^{a_1} cos(2\theta) \\ \text{for } \theta_{i-1} \leq \theta < \theta_i, 1 \leq i \leq n, \theta_0 = \theta_n \end{aligned} \tag{3.12}$$

, where θ_i is the angular position of the corner points in PCS and $r_i(\theta_i)$ is the radius of the corresponding sector at θ_i. And $g_2(\cdot,\cdot)$ is reformulated as:

$$g_2(\theta, r^{\circ}(\theta)) = \begin{cases} \beta_2(r_i(\theta_i))^{a_2} \frac{\pi(\theta-\theta_{i-1})mod(\theta_i-\theta_{i-1})}{2(\theta_i-\theta_{i-1})}, \text{ if } \theta_{i-1} \leq \theta < \theta_i, 1 \leq i \leq n, \theta_0 = \theta_n, \\ 0, \text{ otherwise} \end{cases} \tag{3.13}$$

The deviation function parameters are estimated based on measurement data using Bayesian inference, and the estimated function can be used to derive optimal compensation plans on the nominal CAD part model in order for improved quality.

3.2.4 Discussion

The aforementioned deviation modeling methods all aim at providing a parametric functional form of the in-plane deviation. The first two methods focus on comparing the parameterized nominal and actual shapes. Both the FDs and the Fourier Series are used to derive a parametric shape function. The difference is that, the former represents deviation as the Euclidean point distance with respect to normalized arc length between 0 and 2π, while the latter represents deviation as the radial difference with respect to polar angles. The FDs-based method doesn't operate on coordinates of shape points, so it is not sensitive to the shape complexity. However, the accuracy is comparatively low, and since integrals needs to be computed for shape reconstruction, the computational cost is high. The FSE-based method is much easier to understand and implement, and the adoption of PCS allows an intuitive representation of deviations. But for complex shapes, more terms of the Fourier Series need to be incorporated, thus increasing the number of function parameters. Figure 3.5 illustrates the representation of a hexagon shape with both methods under a 30-order expansion. A zoom-in view is also provided at one corner to highlight the differences. Apparently, with the same order of expansion, the FSE-based method achieves a higher accuracy of representation than the FDs-based method.

The prescriptive methods directly models the deviations in the PCS, where the actual shape is assumed to be centered with the nominal shape. The title 'prescriptive' comes from the fact that they follow an 'observation-prescription-validation' process for model development. First, by observing the deviation profile from the measurement data, an assumption is made on the global function form which may roughly approximate the observation. Then, detailed local variations along the shape boundary are considered by adding extra terms to the global function. Finally, the function is validated and refined using measurement data of new parts. This methodology is quite effective for the quality control purpose due to its ability to statistically identify patterns in the deviation profile. However, the adoption of PCS in both the FSE method and the prescriptive methods limits their application to convex shapes. It's also important to note that the mentioned works focus on a geometrical view, but lack the consideration of physical contributors to the deviation. In the next section, a new shape transformation based method will be proposed which inherently implies the effects of process- and material-related errors.

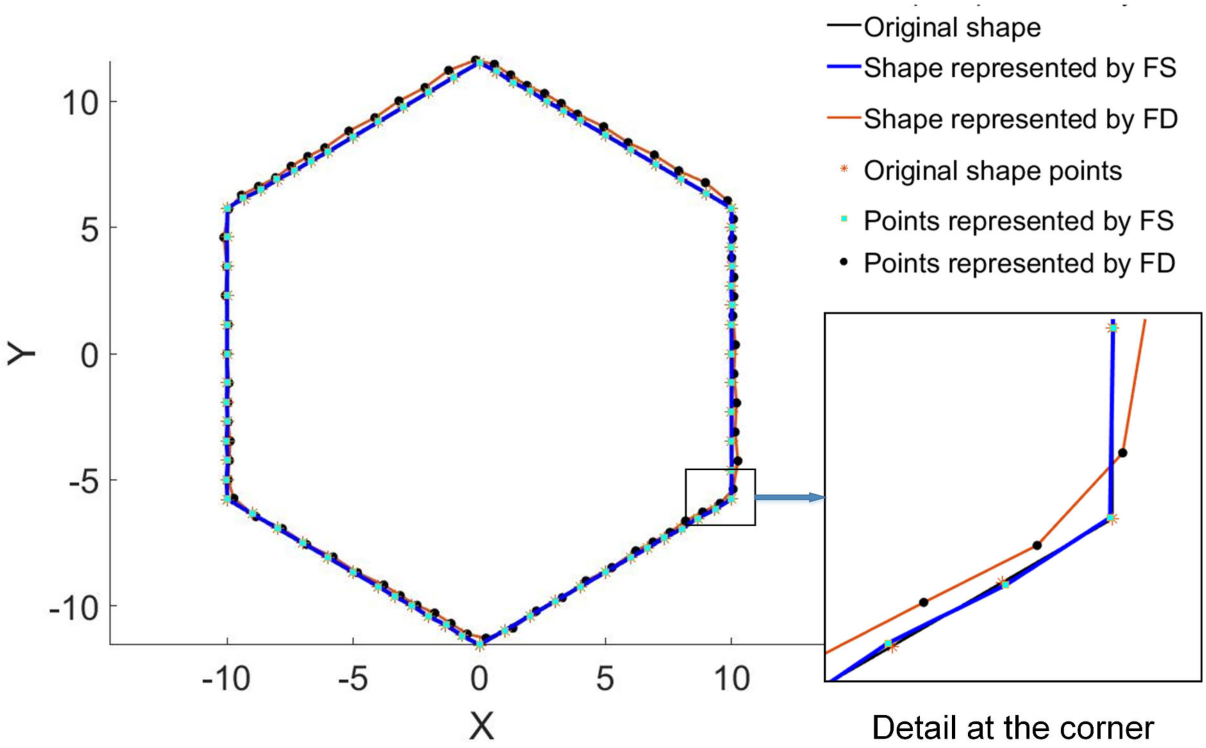

Figure 3.5: Comparison between the representations of a hexagon shape by Fourier Series-based method and the Fourier Descriptors-based method

3.3 Shape transformation perspective for deviation modeling

As major contributors to geometric deviations, the manifold deviation sources in the manufacturing process induce the variations of the nominal in-plane shape. Investigation of the variational effects is critical to the effective modeling of in-plane deviation. In an AM process, on one hand, process-related errors such as unexpected displacement of energy sources or machine axes, may result in slight translation or rotation of shape relative to the machine coordinate system; on the other hand, material-related errors such as thermal shrinkage, may cause deformation of shape from its nominal design. Such variations will be accumulated after the layer-wise building process and as a consequence affect the global product form. Even though it's unrealistic to quantitatively correlate the variations with each deviation source, a reasonable assumption can be made that they could be mapped to the transformations of the nominal shape. In this context, three types of transformations can be defined on the nominal shape as: translations along x- and y-axis $\Delta x, \Delta y$, rotation with respect to the coordinate system origin α and the scaling in x- and y-direction φ_x, φ_y. Figure 3.6 illustrates the respective transformation effects on the nominal shape in an AM process.

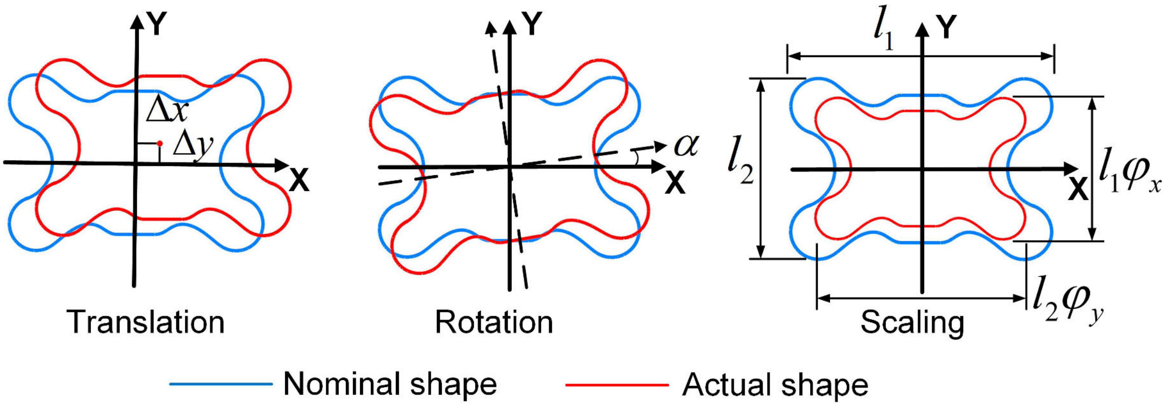

Figure 3.6: Variation of 2D product shape in an AM process

3.3.1 Model formulation

With the defined parameters, the transformation effects could be represented with homogeneous transformation matrices as seen in Equation 3.14, where M_S, M_R, M_T are matrices corresponding to scaling, rotation and translation effect respectively.

$$M_S = \begin{bmatrix} \varphi_x & 0 & 0 \\ 0 & \varphi_y & 0 \\ 0 & 0 & 1 \end{bmatrix} M_T = \begin{bmatrix} 1 & 0 & \Delta x \\ 0 & 1 & \Delta y \\ 0 & 0 & 1 \end{bmatrix} M_R = \begin{bmatrix} \cos(\alpha) & -\sin(\alpha) & 0 \\ \sin(\alpha) & \cos(\alpha) & 0 \\ 0 & 0 & 1 \end{bmatrix} \tag{3.14}$$

The transformation of coordinates between the nominal shape Ω° and the actual manufactured shape Ω^* can thereby be mathematically represented based on the parameter set $\Psi = \{\varphi_x, \varphi_y, \alpha, \Delta x, \Delta y\}$. Denote corresponding points on Ω° and Ω^* as (x°, y°) and (x^*, y^*) in the CCS, the coordinate transformation is then formulated as Equation 3.15, where M_Ψ is the integrated transformation matrix combining M_S, M_R, M_T.

$$(x^*, y^*, 1)^T = M_\Psi (x^\circ, y^\circ, 1)^T \tag{3.15}$$

The reverse transformation is then derived as:

$$(x^\circ, y^\circ) = (h_1(x^*, y^*, \Psi), h_2(x^*, y^*, \Psi)) \tag{3.16}$$

Since we are dealing with the in-plane deviation in PCS, a mechanism needs to be established to map this relationship from the Cartesian Coordinate System (CCS) to PCS. The objective is to have a parametric deviation function with the form shown in Equation 3.17, where $r^\circ(\theta)$ denotes the polar function of the nominal shape and $r^*(\theta; \Psi, r^\circ(\theta))$ the polar function of the manufactured shape approximated by applying transformation on the nominal shape; ε_θ is a noise term to account for the random variation of shape profile and is assumed to be independent and identically distributed (i.i.d) at each θ, with $\varepsilon_\theta \sim N(0, \sigma^2)$.

$$f(\theta; \Psi) = r^*(\theta; \Psi, r^\circ(\theta)) - r^\circ(\theta) + \varepsilon_\theta \tag{3.17}$$

Given a shape that can be analytically expressed by a function CCS, it is convenient to derive both $r^\circ(\theta)$ and $r^*(\theta; \Psi, r^\circ(\theta))$ combining Equation 3.16. In Appendix A, some details are discussed regarding the derivation of in-plane deviation functions for common shapes, including circular shapes (A.1), bi-circular shapes (A.2), elliptical shapes (A.3) and arbitrary polygonal shapes (A.4).

3.3.2 Model estimation

Effective estimation of the model parameters is the key to understanding the actual deviation patterns and the downstream application of this model for prediction purposes. Based on the measurement data gathered from manufactured product samples, the estimation will be conducted following the least-squares principle. The measurement data are provided as point clouds collected from the product surface using a laser scanner. A flowchart of the model estimation procedure is illustrated in Figure 3.7

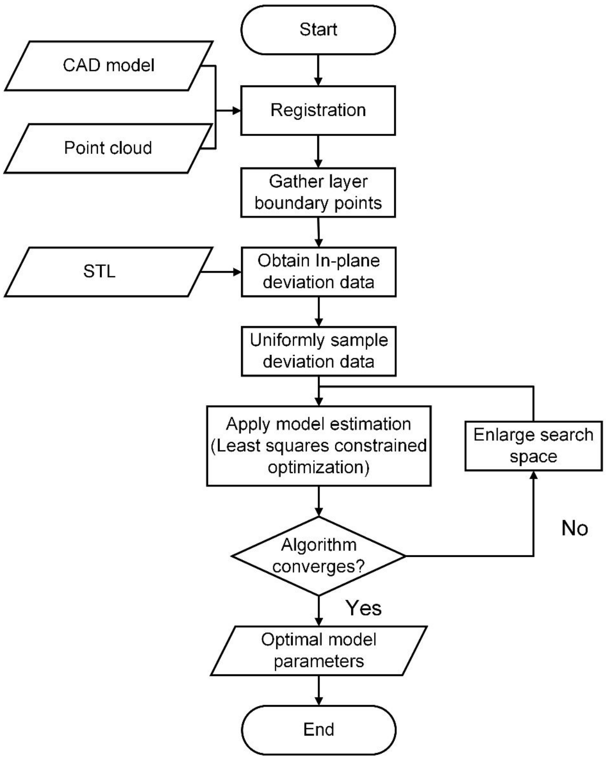

Figure 3.7: Flowchart of the model estimation process

The procedure initiates with the reconstruction of manufactured in-plane shape from boundary points of each layer, which can be extracted from the point cloud according to the layer height determined based on the layer thickness specified for the building process. The extraction is executed as follows:

$$\begin{aligned} &\forall P_m(x_m, y_m, z_m) \in \boldsymbol{P}, \\ &(x_m, y_m) \in \boldsymbol{S}^i, if(h_i - \lambda \leq z_m \leq h_i + \lambda), \\ &i = 1, ..., N_\mathrm{s}; m = 1, ..., M \end{aligned} \tag{3.18}$$

Among all M points in the cloud $\boldsymbol{P}$, the point P_m, whose z-coordinate z_m lies within the bounding zone around the layer height h_i of the i-th layer, is deemed as the layer's boundary point and its x and y coordinates (x_m, y_m) are used to reconstruct the manufactured in-plane shape of the layer. The bounding zone is defined by a threshold value λ that controls the density of collected points in a layer, which should be much smaller than the layer thickness to avoid confusion between data of adjacent layers. After performing the extraction for all N_s layers, each in-plane shape is approximated by connecting the extracted 2D points $\boldsymbol{S}^i$ sequentially. With a sufficiently high collection density, the approximation accuracy can be guaranteed. Thereafter, both the nominal shape and the reconstructed shape are transformed to a common PCS to obtain $(\theta, r^{\circ}(\theta))$ and $(\theta, r^*(\theta))$. Thus the in-plane deviation data are obtained following Equation 3.5.

The collected points, however, are not always uniformly distributed on the boundary, thus adding difficulty to the calculation and comparison of deviations due to the absence of correspondence between points of different layers. As a solution to this issue, the obtained deviation data of each layer are sampled at K angles uniformly distributed within the range $[0, 2\pi]$, denoted as $(\theta_1^u, ..., \theta_K^u)$. Suppose the original data in a layer are evaluated at $L(L > K)$ angles as $(\theta_1^v, \Delta r(\theta_1^v)), ..., (\theta_L^v, \Delta r(\theta_L^v))$, for a sample angle θ_i^u, its two neighboring angles $\theta_j^v, \theta_{j+1}^v$ and the corresponding deviations $\Delta r(\theta_j^v), \Delta r(\theta_{j+1}^v)$ are identified, the deviation at this sample point is thereby linearly interpolated as Equation 3.19. The high density of collected points facilitates the minor loss of accuracy due to interpolation.

$$\Delta r(\theta_i^u) = \frac{\Delta r(\theta_{j+1}^v) - \Delta r(\theta_j^v)}{\theta_{j+1}^v - \theta_j^v}(\theta_i^u - \theta_j^v) + \Delta r(\theta_j^v); \theta_i^u \in (\theta_j^v, \theta_{j+1}^v], j = 1, ..., L-1 \quad (3.19)$$

With the aligned deviation data, the objective now is to derive the optimal transformation parameters $\hat{\Psi} = \{\hat{\varphi}_x, \hat{\varphi}_y, \hat{\alpha}, \hat{\Delta}x, \hat{\Delta}y\}$ that best fit the measured deviations $\{\Delta r(\theta^u)\}$ for each layer of the manufactured part. The least-squares based constrained optimization is adopted aiming at minimizing the squared difference between data and model response, as shown in Equation 3.20. Constraints are imposed on the scaling, rotation and translation parameters using predefined $\delta_s, \delta_r, \delta_t$ in order to limit search range of the optimization algorithm. Since the magnitude of deviation is small in comparison to the product size, limiting the parameters within an anticipated small range could facilitate convergence of the algorithm.

$$\hat{\Psi} = \underset{\varphi_x,\varphi_y,\alpha,\Delta x,\Delta y}{\arg\min} \sum_{i=1}^{K} [f(\theta_i^u;\Psi) - \Delta r(\theta_i^u)]^2 s.t. \begin{cases} \varphi_x, \varphi_y \in [1-\delta_s, 1+\delta_s] \\ \alpha \in [-\delta_r,\delta_r] \\ \Delta x, \Delta y \in [-\delta_t,\delta_t] \end{cases} \tag{3.20}$$

Considering $f(\theta;\Psi)$ is a non-linear function in general cases, the non-linear programming solver *fmincon* of MATLAB® is adopted to implement the optimization. Setting the initial parameter values as $\Psi = (1,1,0,0,0)$, the algorithm iteratively searches within the specified constraints with trial steps aiming to decrease value of the objective function in Equation 3.20. When the current step size is smaller than a predefined step tolerance, convergence is met and the optimal parameters $\hat{\Psi}$ are found.

3.3.3 Case study and comparison with Fourier Series method

In this section, a case study will be presented to validate the proposed transformation perspective with the measured deviation data of a manufactured part. The part is designed as a $5mm$-high regular hexagon shape with its circumscribed radius as $20mm$. A comparison between the proposed method and the FSE method will be made regarding the model complexity and accuracy.

The part is manufactured on a Prusa i3 MK2® FDM printer with $0.2mm$ layer thickness and the rectilinear infill pattern is adopted. The measurement is conducted using the Kreon Aquilon 50 laser scanner. Calibration results indicate that the average measurement error of this scanner in all involved scanning orientations is approximately $0.002mm$, which is negligible compared with the magnitude of geometric deviations and can be attributed to the noise term in Equation 3.7. The point cloud captured from the part surface contains a total sum of 795935 points, from which the layer boundary points are extracted every $0.2mm$ along the build direction with the threshold $\lambda = 0.003mm$ (Equation 3.18). Converting the extracted points to PCS, in-plane deviations are evaluated and subsequently aligned at $K = 360$ uniformly distributed locations along the boundary based on Equation 3.19. The deviation model parameters are estimated for each layer and the fitting result at the 10^{th} layer is provided as an example in Figure 3.8, in which the blue line with dot markers denotes the measured deviation, and red line is the fitted curve given by the proposed method. For better visualization of the result, the noise term is not included in this curve. As a comparison, the Fourier series expansion

(FSE) based method discussed in Section 3.2.2 is also used to fit the same data. Different orders of expansion have been performed and their fitting results can be found as the black curves in Figure 3.8(a), 3.8(b), 3.8(c) respectively. It can be observed from the figure that, the proposed method overcomes the previous FSE method by accurately capturing the patterns in deviation data with much fewer parameters. Especially, in order to approximate sharp transitions of data that take place at corner points of the hexagon shape, plenty of high-frequency terms should be included in the expansion, so even the 35^{th} order expansion can hardly provide a satisfying modeling accuracy.

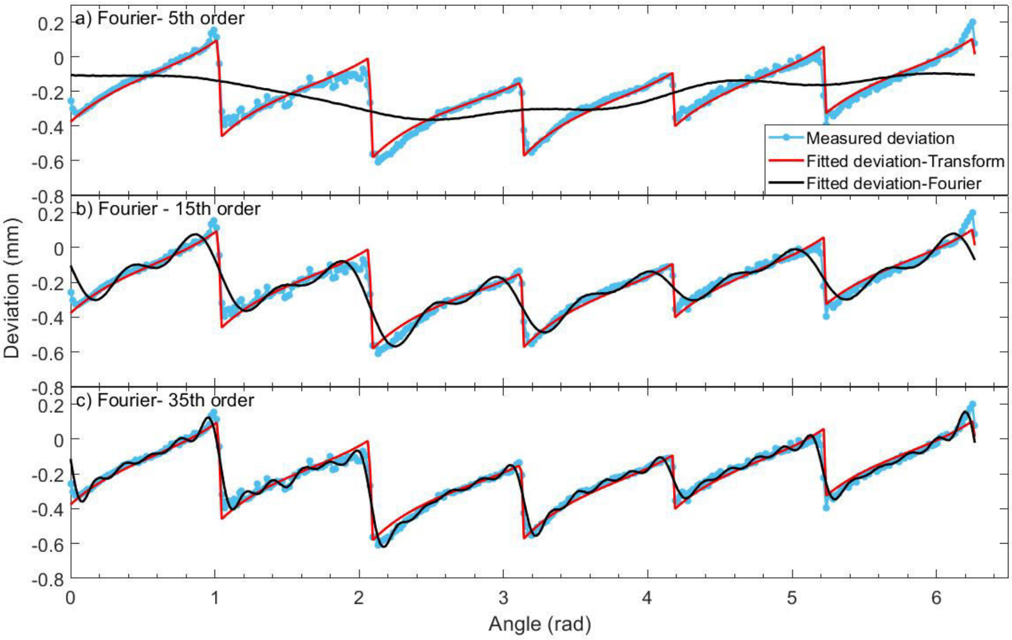

Figure 3.8: Comparison between the results provided by the proposed method and FSE method of (a) 5^{th} order; (b) 15^{th} order; (c)35^{th} order

The modeling accuracy is quantified by the Root Mean Square Error (RMSE) between measured deviations and the fitted values given by the estimated models. Figure 3.9 presents RMSEs of the proposed method and the FSE method evaluated at all layers of the manufactured part, from which it is evident that the modeling accuracy of the proposed method with only 5 parameters, is comparable to the FSE method with more than 35 parameters, thus the model complexity is substantially reduced. Moreover, since the transformation parameters are closely related to physical factors in the manufacturing process, the patterns recognized by the proposed model are more realistic.

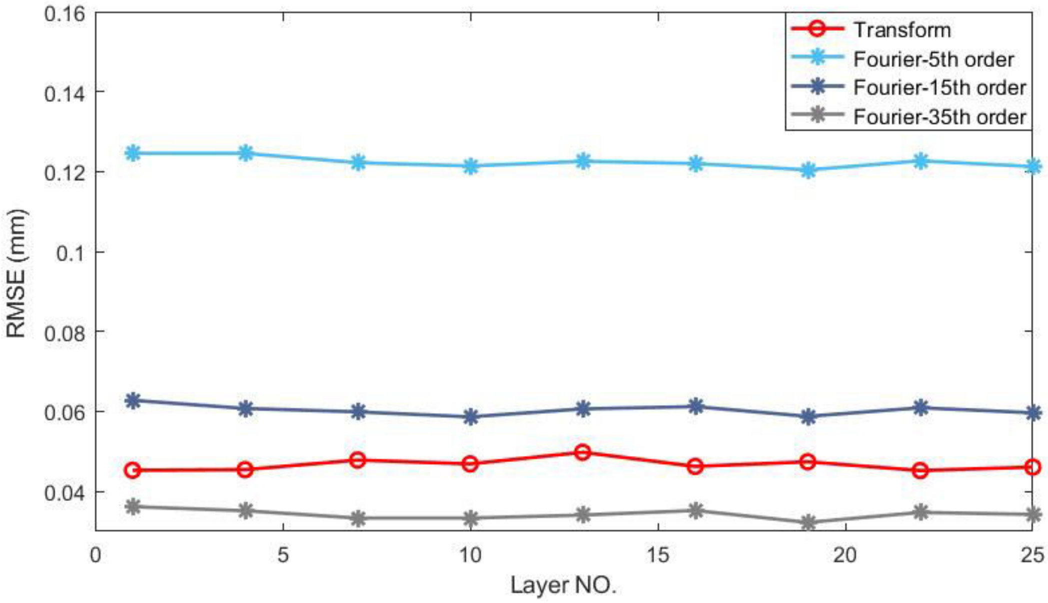

Figure 3.9: Comparison of RMSE of both methods for each slice

3.3.4 Discussion

In this section, in-plane geometric deviations are investigated based on a transformation perspective that maps effects of AM deviation sources to different transformation effects on the nominal shape. Parametric deviation models are formulated for circular and polygonal shapes based on the transformation parameters. This transformation perspective implies the consideration of deviation sources in AM and is based on the geometric information of the designed shape, therefore, compared to the FSE method that approximates the actual shape using high-order Fourier Series, the model generalizes well to different shapes and the model complexity is significantly reduced. Nevertheless, limitations of the method also exist. The transformation parameters are currently treated as constants and applied to the overall shape, thus the model doesn't generalize well for deviations resulted from location-dependent deviation sources. The current model estimation procedure is lacking in a learning capability, so existing parameter settings cannot be effectively reused as knowledge to facilitate the generalization to new process conditions. In the next section, statistical learning methods will be investigated as a complement to the current transformation-based model.

3.4 Statistical learning methods for deviation modeling

3.4.1 Bayesian inference

In the previous section, the least-squares criterion has been adopted to give a point-estimate for the parameters in Equation 3.17. As has been indicated by [GW15], a major weakness of this classic method is that it fails to fully capture the uncertainty within the data, and therefore may yield different parametric models for a set of observation data related to the identical sources of uncertainty. Hence, the Bayesian inference-based method is a desirable alternative in order for improved robustness in parameter estimation. When using Bayesian inference for model estimation, $f(\theta;\Psi)$ in Equation 3.17 is the model structure that provides a function form consisting the parameters $\Theta = \{\Psi, \sigma\}$ to be estimated. Given the measurement data $D = \{(\theta, \Delta r(\theta))\}$, the conditional probability of Θ on f and D is repeatedly assessed by applying Bayes' theorem:

$$\begin{aligned}
\Theta \sim p(\Theta|D,f) &= \frac{p(D|\Theta,f)p(\Theta|f)}{p(D|f)} \\
p(f|D) &= \frac{p(D|f)p(f)}{p(D)} \\
p(D|f) &= \int p(D|\Theta,f)p(\Theta|f)d\Theta
\end{aligned} \tag{3.21}$$

Here Θ is treated as a vector of random variables conditioned on the available data, and instead of estimating fixed parameter values, the idea is to specify the confidence in their values. Equation 3.21 enables us to convert an *a prior* probability density of Θ into a posterior density with evidence of the data D [GW15]. The objective now is to derive a predictive model to infer the distribution of in-plane deviation $\Delta r(\theta^*)$ given new input θ^* based on training data D, model structure f and the parameters Θ, i.e., to determine the posterior predictive distribution of $\Delta r(\theta^*)$ as: $\Delta r(\theta^*) \sim p(\Delta r(\theta^*)|\theta^*, \Theta, D, f)$. Considering the fact that Θ are unknown yet, we aim at marginalizing the probability over the parameter estimates:

$$p(\Delta r(\theta^*)|\theta^*, D, f) = \int p(\Delta r(\theta^*)|\theta^*, \Theta, f)p(\Theta|D,f)d\Theta \tag{3.22}$$

, where $p(\Theta|D,f)$ is the posterior parameter distribution following the form given in Equation 3.21. The solution to the integral in Equation 3.22 and Equation 3.21 is simple for linear model structures since the probabilities are numerically tractable. However, it is obvious from Equation A.1 that our model exhibits a complex non-linear structure, in this situation, the Markov Chain Monte Carlo (MCMC) algorithm provides a possibility to draw samples from the posterior parameter distribution without tackling the complex $p(\Theta|D, f)$. The drawn samples are further used for Monte-Carlo simulation to propagate the uncertainties in parameters to the output of the predictive model while circumventing the analytical evaluation of Equation 3.22 [GW15]. The MCMC algorithm consists the following steps:

- Specify a prior probability distribution for Θ with hyper-parameters Π_Θ.
- Draw from the joint distribution of Θ to obtain a set of sample parameter values $\hat{\Theta}$. Calculate predictions $\hat{\Delta}r(\theta)$ on training data points θ using the model structure $f(\theta; \hat{\Theta})$ and compare $\hat{\Delta}r(\theta)$ with the observed values $\Delta r(\theta)$ using a loss function.
- Evaluate the density of the drawn parameter samples and update the joint distributions of Θ.
- Iterate the sampling and updating steps in search for samples of parameters that are capable of producing better predictions which could reduce the loss function, until a convergence is met where new samples don't contribute to loss reduction.
- MCMC sampling follows the Markov-Chain form, which means the current position of step $n + 1$ is independent of all other steps except for that of its previous step n. The sampler moves around the joint distribution in a semi-random manner and the distance as well as direction of movement is decided by the specific sampling method used.
- After the convergence is met, further iterations are performed to obtain samples for inference of the posterior distribution of parameters. While the process before convergence is called the 'burn-in' process, and the samples drawn in this process will be discarded since they are likely to be poor estimates of the parameter values.

In this research, the Metropolis-Hastings algorithm has been applied for MCMC sampling and the pyMC3 package developed on the Python platform is adopted to implement the Bayesian inference for estimation of parameters in Equation A.1. The details of the algorithm can be found in [Has70] and will not be discussed here. Recall that in the deviation function, we have 6 parameters $\Theta = \{\varphi_x, \varphi_y, \alpha, \Delta x, \Delta y, \sigma\}$. For the first step, prior distributions are assigned for these parameters as Equation 3.23.

$$
\begin{aligned}
\varphi_x \sim N(1, 0.01^2), &\varphi_y \sim N(1, 0.01^2) \\
\Delta x \sim N(0, 0.2^2), &\Delta y \sim N(0, 0.2^2) \\
\alpha \sim N(0, 0.1^2), &\sigma \sim |N(0, 0.05^2)|
\end{aligned}
\tag{3.23}
$$

The mean and standard deviation values specified for each of the parameters are hyperparameters Π_Θ. The in-plane deviation data extracted from measurement are organized as $\{(\theta, \Delta r(\theta))\}$ and serve as the training data. As an example, deviation data at the 10^{th} layer of the manufactured part mentioned in Section 3.3.3 is used to validate the performance of Bayesian inference. Following the MCMC strategy, the parameters are sampled with 6000 draws together with a 500-draw burn-in process [HZSD15a]. The posterior distribution of each parameter is obtained by marginalizing the joint posterior distribution and important statistics, including mean, standard deviation as well as 2.5% and 97.5% quantiles are summarized as Table 3.1. A traceplot of sampling process is shown in Figure 3.10 providing the distribution of drawn samples, in which the samples drawn in the burn-in process have been discarded.

With the estimated parameters, the posterior predictive distribution of in-plane deviation is calculated and compared with the measured deviation data, as illustrated in Figure 3.11. The 95% prediction interval is also indicated which captures most variations of data from the mean prediction. In comparison to the fitting result in Figure 3.8 that gives only a point estimate, Bayesian inference also provides an insight into the uncertainty of data and the estimated model is more robust for prediction purposes.

Parameters	*Mean*	*Standard deviation*	*2.5%*	*97.5%*
φ_x	0.9963	7.01e-4	0.9961	0.9964
φ_y	0.9923	1.44e-3	0.9917	0.9927
α	0.0022	3.99e-4	0.0017	0.0028
Δx	-0.0354	7.41e-3	-0.0386	-0.0341
Δy	-0.0712	1.37e-3	-0.0798	-0.0634
σ	0.0602	2.56e-2	0.0533	0.0670

Table 3.1: Posterior statistics of deviation function parameters

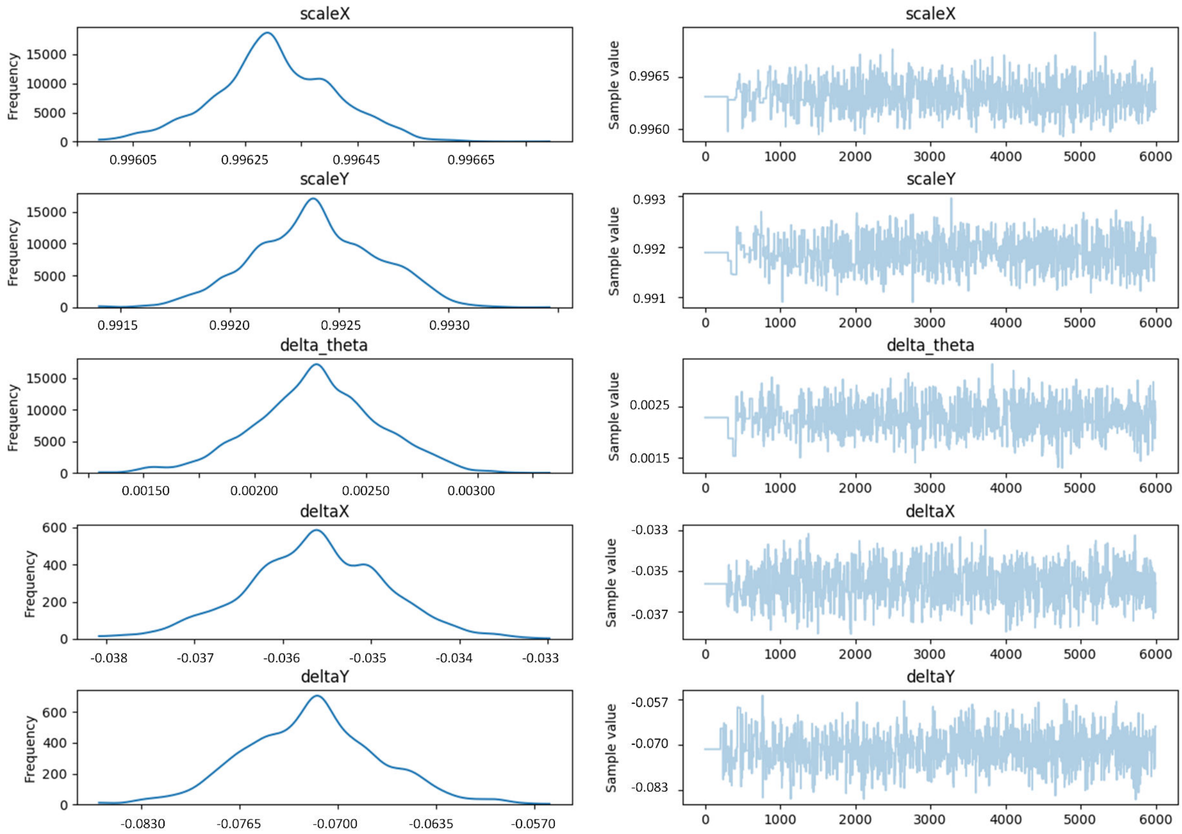

Figure 3.10: Traceplot of the MCMC sampling process

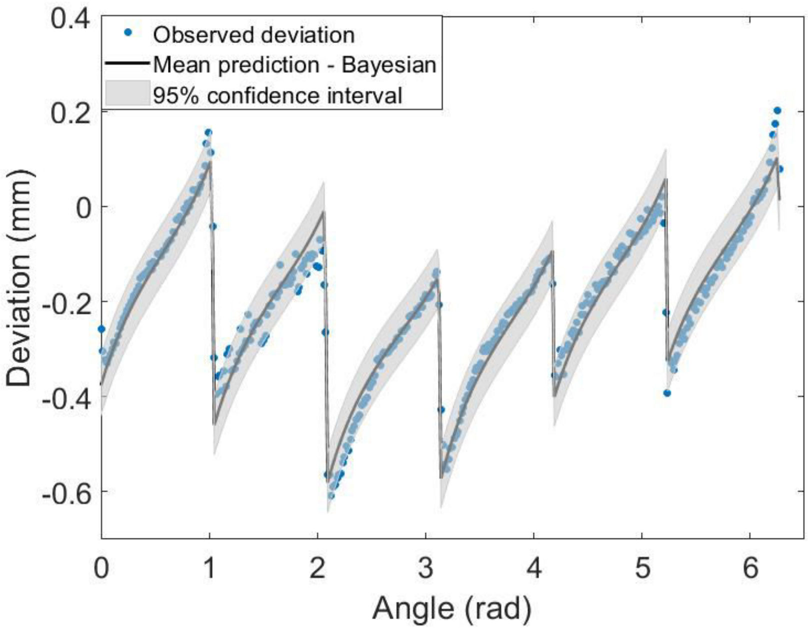

Figure 3.11: Posterior predictive distribution of in-plane deviation

3.4.2 Transfer learning with Multi-task Gaussian process

In Section 3.3, the transformation-based approach has been introduced which applies the transformation parameters in Equation 3.14 to the whole shape and manages to capture the global pattern of in-plane deviation. Whereas, unexplained location-dependent variations still exist around the layer boundary that manifest more complicated patterns. These patterns might be shape-specific and can hardly be interpreted in an analytical way. To obtain an effective characterization of such patterns and increase prediction performance, current model should be enhanced with a learning capability enabling the concurrent learning from deviation data of multiple shapes, sharing the knowledge gained from each shape and providing consistent data-driven predictions for all shapes. With this motivation, a multi-task Gaussian Process (GP) learning algorithm is adopted as an addition to the transformation-based model to cooperatively tackle the deviation modeling problem.

3.4.2.1 Model design

GP is a statistical method widely used in statistics and machine learning due to its ability to capture the intricate non-linear relationship between predictors and responses with limited training data and a moderate number of runs [Ras06, CWT18]. By introducing a new GP component, the new in-plane deviation model aiming at concurrent learning for M objective shapes is presented as Equation 3.24, where $l = 1, ..., M$ is the index of shape. $f_l(\theta; \Psi_l)$ is the transformation-based deviation function of shape l derived by Equation 3.17, as discussed in Section 3.3.1. It's supposed to capture the systematic variations of global shape. $g_l(\theta)$ denotes a zero-mean GP that models the local variation of shape l that cannot be explained by $f_l(\cdot)$. The multi-task learning algorithm will be used to jointly learn from the deviation data of all M shapes and give optimal estimation of each $g_l(\cdot)$, as illustrated in Figure 3.12.

$$y_l(\theta) = f_l(\theta; \Psi_l) + g_l(\theta) \tag{3.24}$$

With this new model, the objective is to predict the deviation at any location θ of a given shape l provided with the knowledge transferred from other shapes manufactured under similar conditions. The knowledge could be process- or material-related, and the transfer mechanism could avoid over-fitting in comparison with GPs trained indepen-

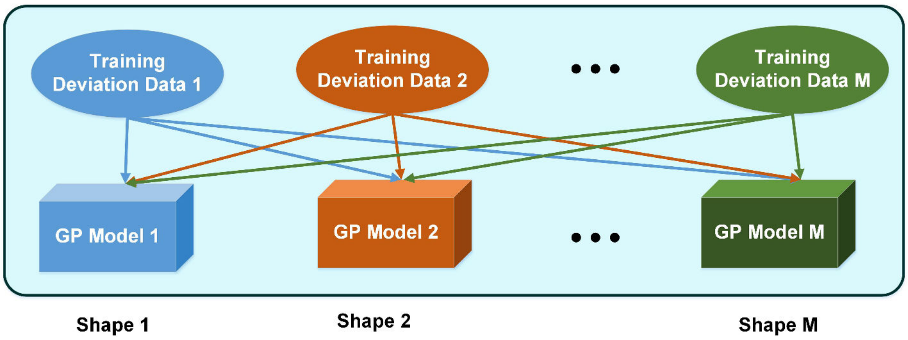

Figure 3.12: Multi-task Gaussian Process learning for multiple shape deviation data [SRW+16]

dently for each shape. Predictions made by the model could also provide an overall understanding of in-plane deviation along the shape boundary.

3.4.2.2 Model Estimation

The optimal parameter values in $f_l(\theta;\Psi_l)$ and the GP models $\hat{g}_l(\theta)$ are estimated based on deviation data extracted from measurement. For each shape, deviations are sampled at N uniformly distributed angles $\boldsymbol{\theta}$ in PCS, thus composing a deviation dataset $\boldsymbol{\Delta} \in R^{N\times M}$. The estimation of $f_l(\theta;\Psi_l)$ is conducted following the same least-squares principle as depicted in Section 3.3.2.

Deviations that remain unexplained by the estimated $f_l(\theta;\hat{\Psi}_l)$ subsequently serve as the training data for multi-task learning. The input for learning is the polar angles $\boldsymbol{\theta}$ and the set of responses corresponding to data of the M shapes are grouped as a vector $\boldsymbol{v} = (v_{11}, .., v_{N1}, .., v_{1M}, .., v_{NM})$, in which $v_{il} = \Delta_{il} - f_l(\theta_i;\hat{\Psi}_l)$ is the unexplained deviation of shape l at θ_i and Δ_{il} is the measured deviation at the same location. The dataset $(\boldsymbol{\theta}, \boldsymbol{v})$ is further randomly subdivided into a training set $(\boldsymbol{\theta}_o, \boldsymbol{v}_o)$ and a test set, and the training-test size can be varied to validate the prediction performance. The trained $\{g_l(\cdot)\}$ is expected to be capable of predicting the unobserved deviation of each shape at any new θ^*. Inspired by the research of Bonilla et al. [BCW08], the multi-task learning for GP is conducted by placing a prior on the latent GP functions $\{g_l(\cdot)\}$ to directly induce correlations between tasks. The zero-mean GP is fully defined by

$$\begin{aligned} \langle g_l(\boldsymbol{\theta}), g_k(\boldsymbol{\theta}')\rangle &= K^g_{lk} k^\theta(\boldsymbol{\theta}, \boldsymbol{\theta}', \gamma) \\ v_{il} &\sim N(g_l(\theta_i), \sigma_l^2) \end{aligned} \tag{3.25}$$

where K^g is a positive semi-definite matrix that specifies the inter-task similarities, k^θ is the correlation function over input data with hyper-parameter γ and σ_l^2 is the noise variance for task l.

The standard GP formulae is followed to infer the mean and variance of the predictive distribution of data. For a new data-point θ^* from the task l, the mean prediction is given by

$$\begin{aligned} \hat{g}_l(\theta^*) &= (k_l^g \otimes k_*^\theta)^T \Sigma^{-1} \boldsymbol{v} \\ \Sigma &= K^g \otimes K^\theta + D \otimes I \end{aligned} \tag{3.26}$$

where $\otimes$ is the Kronecker product, k_l^g is the l-th column of K^g, k_*^θ is the covariance vector calculated with respect to θ^* and training points $\boldsymbol{\theta}_o$, K^θ is the covariance matrix between training points, D is an $M \times M$ diagonal matrix whose (l, l)-th element is σ_l^2 and Σ is an $MN \times MN$ matrix. The hyper-parameters of the model, namely γ of k^θ and the matrix K^g, are learned by maximizing the marginal likelihood $p(\boldsymbol{v}_o \mid \boldsymbol{\theta}, \gamma, K^g)$ with a gradient-based method.

3.4.2.3 Case study

To verify the learning ability of this statistical model, a case study is provided in this section regarding three shapes, including a circular shape, a regular pentagon and a regular hexagon. Each shape is designed with three sizes and manufactured by the same Prusa i3 MK2 printer. The part size, denoting the radius of the circular shape and the circumcircle radius for the two polygonal shapes, are selected as $10mm$, $15mm$ and $20mm$ and the height of all parts is set as $8mm$. The manufacturing process is configured with the layer thickness as $0.2mm$ and the infill percentage as 100%. Figure 3.13 shows a photo of the printed parts.

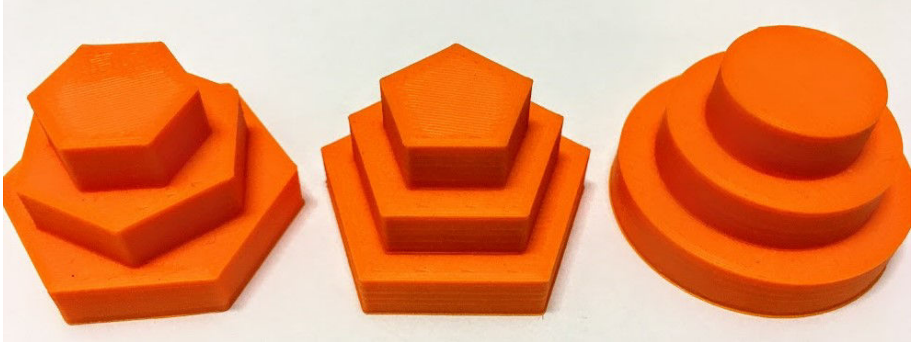

Figure 3.13: Manufactured parts for the case study

The point cloud of each part is obtained by a laser scanner, from which the layer boundary points are extracted with the strategy in Equation 3.18. To ensure point density, a $\pm 0.01mm$ bounding zone is used for extraction. Since all the shapes are manufactured at the center of printer platform, the PCS origin always coincides with the machine coordinate system origin. Hence, the in-plane deviation of each shape is calculated at $N = 360$ uniformly distributed angles as the average value of deviations from all layers observed at these angles.

Following the procedure described in Section 3.4.2.2, first $f_l(\theta; \Psi_l)$ is estimated separately for each shape through least-squares fitting. The derived parameter values are given as Table 3.2.

	TransX (mm)	*TransY* (mm)	*Rotation* (rad)	*ScaleX* (%)	*ScaleY* (%)
Hex R20	0.101	-0.033	-0.020	98.69	98.88
Hex R15	0.050	-0.023	-0.020	98.83	98.45
Hex R10	0.006	0.009	-0.020	97.77	98.25
Pen R20	-0.005	-0.087	0.0035	99.19	98.80
Pen R15	0.009	-0.018	0.0032	99.14	98.72
Pen R10	-0.018	0.010	0.0038	98.41	98.26
Cir R20	-0.056	-0.075	0	99.21	98.98
Cir R15	-0.052	-0.009	0	99.07	98.84
Cir R10	-0.068	0.037	0	98.52	98.36

Table 3.2: Estimated transformation parameters for each shape

As parts are manufactured independently, the positioning error may not be reproduced from part to part. Therefore, the estimated translation parameters are inconsistent between different parts. The rotation parameters, however, exhibit much similarity among parts of the same shape. This phenomenon can be explained by the fact that rotation error is closely affected by the extruder tool-path, the planning of which in turn differs with the specific shape. The scaling parameters clearly indicate the shrinkage of each part in x- and y-direction, thus confirming the assumption of shape transformation on the FDM process. Prediction made by $f_l(\theta; \hat{\Psi}_l)$ on the deviation of three shapes is shown in Figure 3.14, from which it's clear that the main deviation patterns have been explained.

The remaining deviations are grouped into 9 sets of input data for estimation of $g_l(\theta)$, each corresponding to one shape and treated as input for one task. The 9-task GP learning algorithm is then trained respectively on 45%, 60% and 75% of randomly

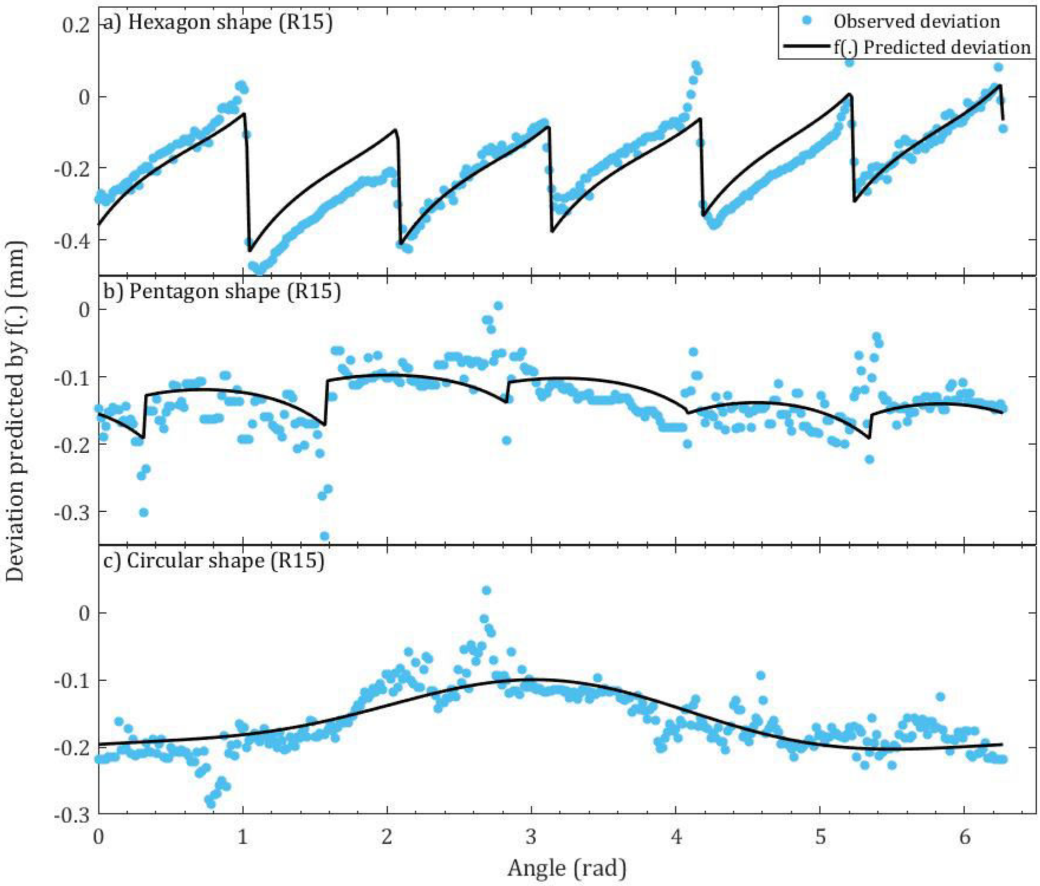

Figure 3.14: Deviation predicted by f(·) for three shapes of size R15

selected training set. The prediction made by the estimated $\hat{g}_l(\theta)$ trained with the 60% training set is shown in Figure 3.15, with regard to the same shapes as in 3.14. It can be observed that $\hat{g}_l(\theta)$ ensures a close prediction of all the deviations even with only 60% of available data.

Moreover, the prediction performance is measured by the R-square of models trained with the three training sets, as seen in Table 3.3. With 45%, 60% and 75% of training data, the model achieves average R-squares as 0.9332, 0.9478, and 0.9716 respectively, thus proving the prediction accuracy of this new model on unobserved data. It is also worth noting that, the model reaches a promising accuracy based upon 45% of training data, which approves its practicality for situations where observed data is insufficient. Multi-task learning enhances the previous model with the ability to simultaneously learn from deviation data of multiple shapes and improve the prediction results on all shapes.

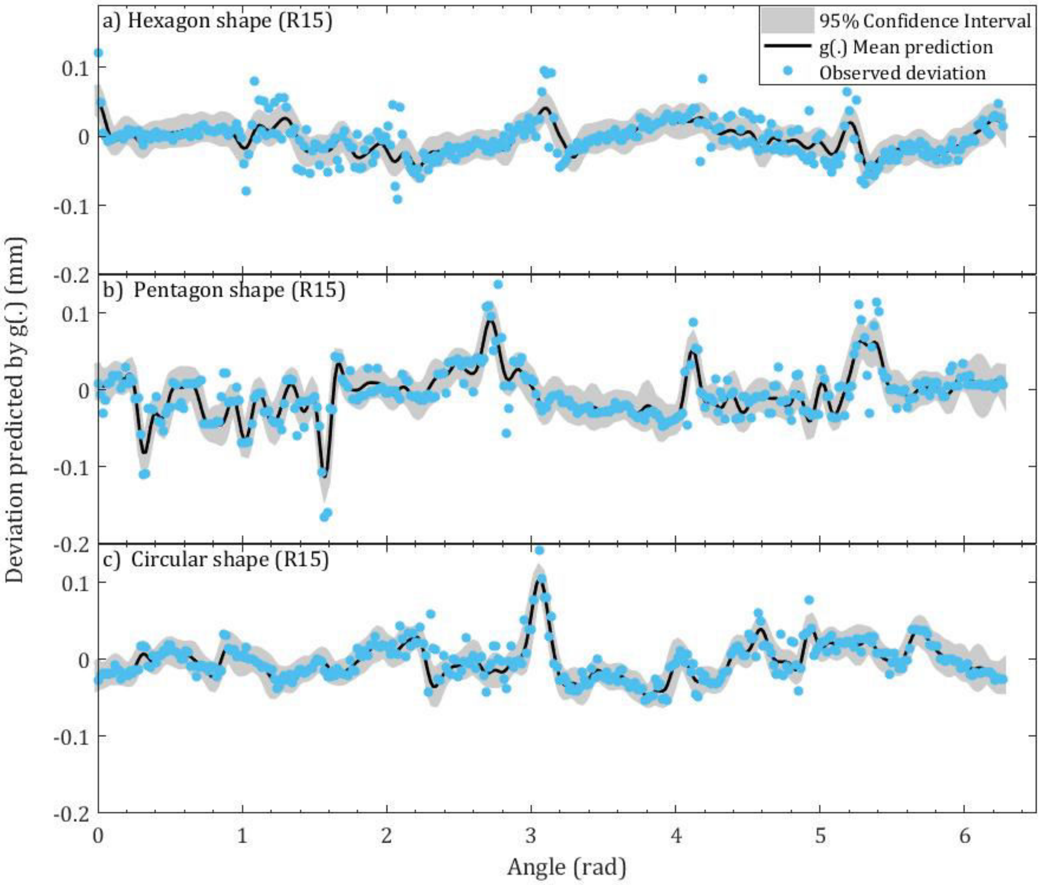

Figure 3.15: Deviation predicted by g(·) for three shapes of size R15

Training set size	45%	60%	75%
Hex R20	0.9765	0.9798	0.9833
Hex R15	0.9674	0.9661	0.9768
Hex R10	0.8749	0.8774	0.9482
Pen R20	0.9747	0.9813	0.9874
Pen R15	0.8982	0.9348	0.9659
Pen R10	0.7937	0.8355	0.9022
Cir R20	0.9897	0.9959	0.9977
Cir R15	0.9356	0.9709	0.9899
Cir R10	0.9883	0.9889	0.9929

Table 3.3: R-square evaluated on training sets of different sizes

3.4.3 Discussion

In this section, statistical learning methods are discussed on the basis of Section 3.3. The transformation-based method captures the global variation of the in-plane shape and can be seen as a systematic deviation model. However, the point-estimate of transformation parameters limits its ability to represent the randomness of deviation data. Therefore, Bayesian inference is introduced to derive the distribution of these parameters based on training data, thus the uncertainty of the estimated model is accounted for. To model the local variations along the shape boundary and to improve the knowledge sharing between different shapes, a multi-task Gaussian process model is proposed as an addition to the transformation-based model. It enables the simultaneous learning from deviation data of multiple shapes and the improvement of prediction performance on all shapes. The limitation of this multi-task learning approach, however, is that it considers only the polar angles as input. So the 'multi-task' actually denotes 'multi-shape'. Further development of this approach can be made regarding 'multi-layer' or 'multi-process condition', thus enhancing the learning ability by considering different layers of a part or parts manufactured under different process conditions.

3.5 Conclusion

In-plane deviation denotes the shape variation of a fabricated layer. The accumulation of in-plane deviations will result in a global effect to the surface form errors, for example, the cylindricity of a cylindrical part. The main concern is to derive a model that could represent variation of the layer contour, so the modeling problem can be reduced to a 2D problem.

In this chapter, approaches for the modeling of in-plane deviations are discussed. Motivated by the awareness that in-plane deviation measures the difference of manufactured shape with nominal shape in a single layer, the parameterization of in-plane shapes is investigated with FDs and Fouriers series with the objective to have a parametric deviation representation. With this basis, considering the weaknesses of such methods and the importance to account for physical deviation sources in AM, a transformation based model is newly introduced which manages to capture deviation patterns regardless of the complexity of shape. To enhance model capability and robustness, statistical methods are developed enabling both the learning for single shape and the knowledge transfer between shapes. The discussed methods are mainly based on the PCS to provide more intuitive understanding of the deviation patterns along the shape boundary. Whereas, current methods are only validated on convex shapes. When dealing with concave shapes or shapes with internal holes where more than one point may exist along one polar angle, multiple PCSs have to be established to collectively model the concave segments or the boundary of holes. When using these deviation models for SMS building, the nominal in-plane shape is deformed with the predicted deviations in the PCS and then transformed back to the CCS, since the SMS are always represented in CCS.

Some sections of this chapter include published works, including Section 3.2.2 published in *27th CIRP Design Conference* [ZAM17], Section 3.3 in *15th CIRP Conference on Computer Aided Tolerancing* [ZAM18] and Section 3.4.2 in the journal *CIRP Annals - Manufacturing Technology* [ZAHM18].

Chapter 4

Out-of-plane geometric deviation modeling for AM

Contents

4.1 Introduction

The modeling of in-plane deviation focuses more on how the contour of in-plane shape varies in independent layers. For out-of-plane deviation, there are new issues that need special attention when developing the model. Since out-of-plane deviation is defined as the deformation of layer in the build direction, the internal layer geometry should also be considered, which is different from the in-plane case where only the external boundary is concerned. Especially for building the Skin Model Shapes, deviations on points of the top and bottom part surface have to be modeled. Therefore, the PCS is no longer a suitable choice. The out-of-plane of one layer may be affected by other layers due to the inter-layer propagation of thermal and mechanical effects. The accumulation of deviations from previous layers also has an impact on the current layer, so the modeling problem should be dealt with in a layer-wise manner.

The warpage effect that has been investigated in a number of studies can also be treated as a kind of out-of-plane deviation, since the effect causes deflection of layers in the build direction, especially at the part bottom. In the first section of this chapter, some analytical out-of-plane deviation models will be summarized. The cross-section-wise method introduced in Section 4.2.1 and the warpage models in Section 4.2.2 aim at developing analytical functions based on measurement data to describe deviation. The derived functions can be used as systematic models to predict deviations on the part surface. As a complement, the random field method is introduced in Section 4.2.3 to account for randomness of deviation while ensuring the topological consistency. However, such methods operate only on the whole part surface and therefore are insufficient to meet up with the demands posed by the new concerns mentioned above.

Data-driven methods have received increasing attention in research related to AM, especially in the study of process effects on the different phenomena in AM, including shape shrinkage [CWT18], thermal field distribution [LJY18], melt-pool depth [Kam16], etc. Based on experimental data collected from a number of Finite Element simulations, these methods allow for building statistical models to predict the concerned responses given the process parameters under which experiments are conducted. Motivated by the challenges in out-of-plane deviation modeling and the multiple advantages offered by data-driven methods, a new method is proposed in Section 4.3 focusing on a layer-wise investigation of out-of-plane deviation patterns in AM parts, with respect to some key influential parameters. The identification of deviation patterns is approached with two methods: Discrete Cosine Transform and Statistical Shape Analysis, both being able to extract the most significant modes from deviation data. The effect of design and process parameters on the identified modes is further characterized with a statistical model. By training the model with observation data collected from experimental parts simulated with designed combinations of process parameters, this model is able to make effective predictions of out-of-plane deviations of new parts. A case study is presented in Section 4.4 to validate the proposed methods and a comparison of the two modal analysis methods is made in Section 4.5 based on results of the case study.

4.2 Modeling out-of-plane deviation from external surface

4.2.1 Prescriptive deviation model in Spherical Coordinate System

In a series of works by Huang et al. [JQH15, JQH16, JJH16], the out-of-plane deviation has been modeled with prescriptive methods based on the Spherical Coordinate System (SCS). Figure 4.1(a) illustrates the representation of out-of-plane deviation for a cylindrical part in the SCS. The central axis of the SCS is parallel to the build direction and any point on the part surface is represented with the coordinate $(r^\circ, \varphi, \theta)$, where r° is the radial distance to the origin, φ is the polar angle and θ is the azimuth angle. Hence, the surface can be subdivided into vertical cross-sections by specifying θ. The boundary points of a cross section at θ can then be represented in an associated PCS, and the deviation $f_z(r^\circ, \varphi|\theta)$ is defined as the displacement of points in vertical direction, as shown in Figure 4.1(b). Therefore, for each cross-section, the deviation can be modeled in a similar way to that of the in-plane case as discussed in Section 3.2.3. The difference is that, in-plane deviation is modeled along radial direction while out-of-plane deviation is along the vertical direction [JQH15], and the latter illustrates different patterns from the former due to inter-layer reactions and gravity [JJH16]. With such considerations, a predictive deviation function for each cross-section θ is derived as:

$$\begin{aligned} f_z(r, \varphi|\theta) &= g_1(\varphi', r^\circ(\varphi')|\theta) + g_2(\varphi', r^\circ(\varphi')|\theta) \\ \varphi' &= mod(\pi/2 - \varphi, 2\pi) \end{aligned} \tag{4.1}$$

, where $g_1(\varphi', r^\circ(\varphi')|\theta)$ is the cylindrical basis function transferred from Equation 3.8 to consider deviation in vertical direction and to incorporate inter-layer interaction effect, and $g_2(\varphi', r^\circ(\varphi')|\theta)$ is the refined cookie-cutter function combining both saw-tooth and square wave forms to fully describe the transition of deviation along the cross-section shape boundary.

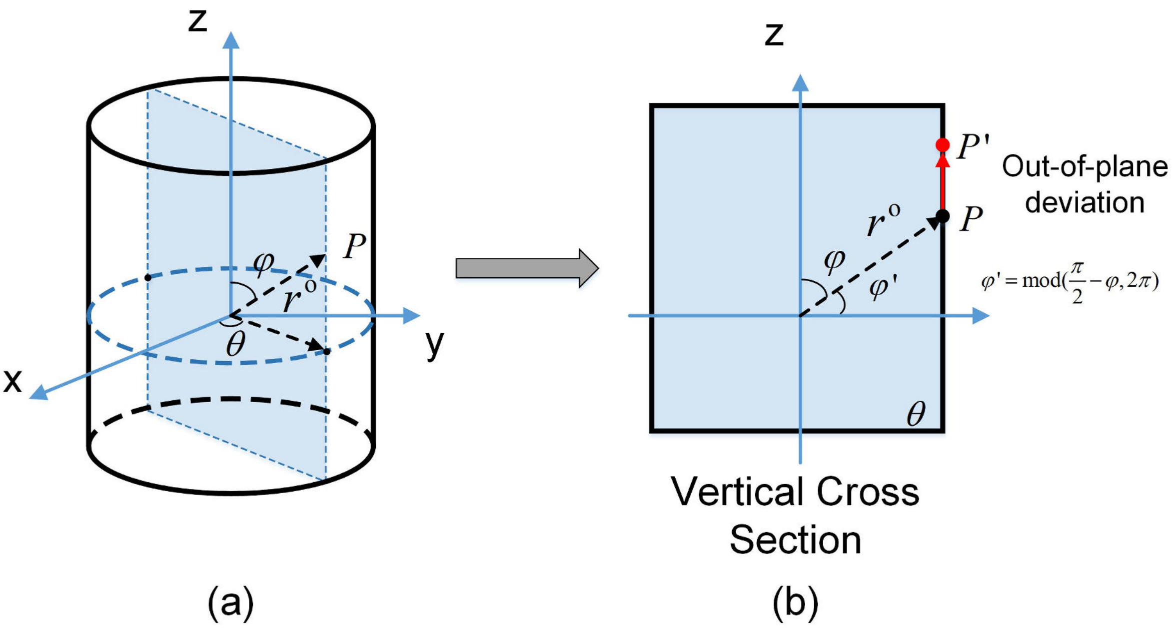

Figure 4.1: The out-of-plane deviation represented in (a) the Spherical Coordinate System; (b) the vertical cross-section [JQH16]

This predictive function has been validated with experimental data of cylindrical and simple polygonal shapes manufactured by the SLA process. However, this work is limited to only a specific process setting, since no process parameters are taken into account in the model. Moreover, the fact that this function is derived for single cross-sections hinders its performance on complex shapes that are not rotation symmetric.

4.2.2 Systematic model of warpage deviation

The warpage distortions that are commonly observed on flat and thin additive manufactured parts, can be deemed as a visible effect of the out-of-plane deviation. Warpage could be attributed to the shrinkage occurring inhomogeneously across the part volume in the AM process [SZZ16], or to the bending distortion when part is removed from the platform and thermal stresses are released [ABC18]. The modeling of warpage behavior has been approached to by researchers regarding different AM processes. In [SZZ16], the warpage effects in AM are classified into the following categories:

- *Curling effect*, denoting the bending of the peripheral regions in the build direction due to residual stresses induced by heterogeneous shrinkage of individual part layers.

- *Trapezoid deformation* occurring at part edges as a consequence of internal force transition between fabricated layers.

- *Blocked shrinkage*, which is usually observed in powder-based AM processes as a result of the resistance of enclosed loose powder against the shrinkage of part geometry.

- *Pincushion effect* denoting the contraction of external planes where the binder solidifies more quickly than internal regions, commonly observed in binder jetting processes.

Among all the effects, the curling effect is the most significant contributor to out-of-plane deviation. Figure 4.2 illustrates the curling effect on a manufactured thin-plate rectangular part, from which it can be seen that the deviation occurs in z-direction and is parameterized with three factors [SZZ16, SBJ+16]: affected length d, deviation of the bottom surface δ_b and the top surface δ_t. By measuring these factors, reverse compensation is conducted on the CAD model in order for improved geometrical accuracy of the manufactured part. However, no mathematical representation of the warpage deviation was investigated with respect to the mentioned factors in this work.

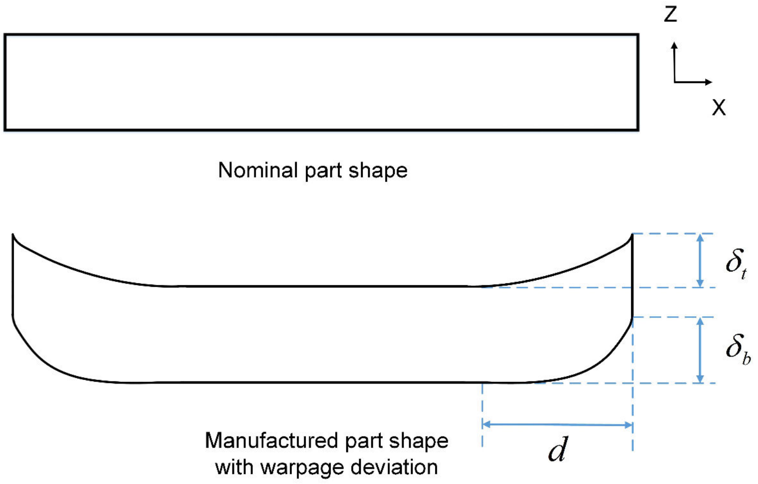

Figure 4.2: Depiction of the curling effect on a manufactured thin-plate part

In [ABC18], a function of the warpage deviation in FDM process is derived through experimental studies. Variables including part geometry, material property and process parameters are taken into account and test artifacts are manufactured with different combinations of the variables. Similarly, the designed artifacts are flat rectangular plates. In this research, warpage is interpreted as the flatness error of the top surface evaluated from the point cloud collected by a 3D scanner, as denoted by δ_t in Figure 4.2. Since the experimental part is a thin plate, it is assumed that $\delta_b \approx \delta_t$ and the function is given as:

$$\begin{aligned}
\delta_b &= \frac{3}{4}\alpha(T_g - T_c)\frac{l^2 m\Delta h}{h^2}(1 - \frac{m\Delta h}{h})f(h, \Delta h, m, a) \\
f(h, \Delta h, m, a) &= \begin{cases} 1, & \text{if } a \geq \frac{4}{3} \\ 1, & \text{if } a < \frac{4}{3}, h \geq \frac{3m\Delta h}{2-\sqrt{4-3a}} \\ 1 - \frac{1}{4}(2+c)(1-c)^2, & \text{if } a < \frac{4}{3}, h < \frac{3m\Delta h}{2-\sqrt{4-3a}} \\ c = \frac{a-b}{3b(1-b)}, & b = \frac{m\Delta h}{h} \end{cases} \\
a &= \frac{\sigma_Y}{E\alpha(T_g - T_c)}
\end{aligned} \tag{4.2}$$

, where α is coefficient of thermal expansion, T_g is the glass transition temperature, T_c is temperature of the heated chamber; l, w, h denote the length, width and height of part, Δh is the layer thickness; a measures the thermo-mechanical properties of the material and is a function of yield point σ_Y, Young's modulus E, α, T_g and T_c. This model, though comprehensive, only gives an empirical estimation of the deviation value and therefore cannot be used to predict deviation at specific locations of the geometry.

Another empirical model is reported in [WXJ07] which considers both the inter-layer and intra-layer warpage deformation. The model is given as:

$$\delta_b = \frac{n^3 \Delta h}{6\alpha(T_g - T_c)(n-1)} \times \left\{1 - \cos\left[\frac{3\alpha L}{n\Delta h}(T_g - T_c)\frac{n-1}{n^2}\right]\right\} \tag{4.3}$$

, where $T_g, T_c, \Delta h$ share the same definition as in Equation 4.2; L denotes the stacking section length and n is the number of deposited layers. The two functions, namely Equation 4.2 and Equation 4.3, can further be combined with Figure 4.2 to determine where and how the nominal surface could be deformed.

However, the warpage effect is represented as a single scalar and validated on simple thin-plate parts in these empirical models, and only the top and bottom layers are considered. Therefore, they can hardly capture the precise information about deviation of the whole part surface. Nevertheless, they provide some geometrical and physical insights into how the part surface varies due to the warpage effect. Based on the surface geometry and warpage value calculated from the models, a polynomial deviation function can be fitted as $\Delta z(x, y) = f(x, y)$, which could serve as a systematic deviation function for modeling out-of-plane deviations when no observation data are available. The function can also be used to predict deviations on certain control points, and with the help of Free-form Deformation (FFD), the deviation on all points of the part surface can be known.

4.2.3 Random deviation modeling with random field

Apart from the systematic deviations that can be analytically modeled, the unexpected deviations should also be considered in order to achieve more realistic approximation to the reality. The random field method introduced in Section 2.3.3.1 to model the random deviations of SMS is well suited for this purpose. Instead of calculating the random deviation values on vertex normals of the whole geometry, the random out-of-plane deviation is considered for contour points of layers in the vertical build direction, as illustrated in Figure 4.3(a) and (b). To begin with, the contour points at each layer are obtained by slicing the STL representation with horizontal planes at corresponding layer heights, resembling the procedure in obtaining the nominal in-plane shape. The obtained points together form a point cloud, whose coordinates are treated as random variables of the random field. With an assumed covariance function and correlation length, the correlation matrix is calculated following Equation 2.5. With the eigenvectors and eigenvalues derived from the correlation matrix, the random deviation associated with each point is calculated with Equation 2.4. Finally, the slice contour points are displaced in the vertical direction with the amount of deviation values.

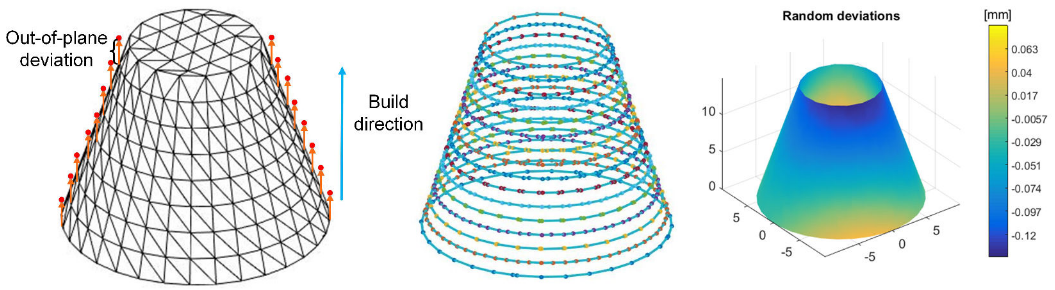

(a) STL representation (b) Slice contour points (c) Random deviations calculated with random field

Figure 4.3: Generation of random deviations on nominal part model with random field

The correlation matrix measures the impact of one point on its neighboring points, either within the same layer or in adjacent layers, thus capturing the intra-layer and inter-layer random effects between points. Figure 4.3(c) shows the generated random deviations for the cone surface, where the deviation values are displayed with a color map.

4.2.4 Deformation of nominal model with Free-Form Deformation (FFD)

In this section, the FFD-based method will be introduced aiming at integrating the above-mentioned deviation models to obtain the out-of-plane deviation on part surface. Originally presented in [SP86], free-form deformation (FFD) is a technique that enables the transformation of a geometric model by deforming the cube or hull that encloses the model. Instead of performing deformations directly on the object, FFD bypasses the intra-object interactions and brings more efficiency benefits [LFC$^+$18]. To begin with, a parallelepiped volume is constructed that fully wraps the geometric model. The volume is further subdivided into a lattice structure which is composed of tricubic Bezier hyperpatches specified by a 3D grid of control points P_{ijk}. Each hyperpatch defines a volume of space parametrized by the three parameters u,v, and w, where $u, v, w \in [0, 1]$. Any point (x, y, z) inside the volume can be represented as Equation 4.4:

$$FFD(x, y, z) = \sum_{i=0}^{l} \sum_{j=0}^{m} \sum_{k=0}^{n} B_i^l(u) B_j^m(v) B_k^n(w) P_{ijk} \tag{4.4}$$

, where $B_i^l(u)$,$B_j^m(v)$ and $B_k^n(w)$ are Bernstein polynomials of degree l,m and n, for example $B_k^n(w) = \frac{n!}{k!(n-k)!} w^k (1-w)^{n-k}$; $l+1$,$m+1$ and $n+1$ denote the number of control points along the coordinate axes. By deforming the control points, the deformations are further applied to each point enclosed in the volume through Equation 4.4. A larger number of control points implies a more precise control of the local deformations. The generation of an SMS from the nominal STL model using FFD consists of the following steps:

- Construct the parallelepiped volume enclosing the STL model. According to level of control on the accuracy, specify the number of control points P_{ijk} on each dimension of the bounding volume and obtain the lattice structure.

- For each point $M_{nom}(x, y, z)$ of the STL model, assign the corresponding parameters (u, v, w) according to its relative position in the lattice that it lies in.

- Calculate the out-of-plane deviations ΔP_{ijk} of each control point according to the empirical models and obtain the deviated control point as $P'_{ijk} = P_{ijk} + \Delta P_{ijk}$.
- Calculate the deviated coordinates $M_{dev}(x, y, z)$ of the STL points by replacing P_{ijk} with P'_{ijk} in 4.4.

4.2.5 Application

As an example, the modeling of out-of-plane deviation is demonstrated on a square part with $L = 40mm$ side-length and $h = 10mm$ height. The STL representation as well as its bounding volume can be found in Figure 4.4(a). A number of 10 control points are specified on x and y dimension of the bounding volume, together with 2 points on z dimension representing the bottom and top layer, thus defining the lattice structure as seen in Figure 4.4(b). Following Equation 4.3, the warpage deviations are calculated at the bottom and top layer, denoted as δ_b and δ_t that are illustrated in Figure 4.2. The control points at corners of the two layer, colored with blue and red in Figure 4.4(b), are deformed in z direction with the distance δ_b and δ_t respectively. The affected length d is selected as $d = L/2$, which means the center point of the layer remains undeformed. Under the constraints of the center and corner control points, two cubic polynomial deviation functions $\Delta z_b(x, y) = f_b(x, y)$ and $\Delta z_t(x, y) = f_t(x, y)$ are fitted respectively for the bottom and top layer, and used to deform other control points. The deformed points are shown in Figure 4.5(a) as compared to their original positions.

According to the deformed control points, FFD is performed on all points of the STL and their original coordinates are replaced with the deformed ones. Figure 4.5(b) shows the STL representation of the part incorporating the out-of-plane deviations, where the magnitude of deviation values is visualized with a color map.

The random out-of-plane deviations are calculated with the random field method. With no available experimental data, here an assumption is made on the random field parameters by setting the mean as $\mu = 0$, the standard deviation as $\sigma = 0.05$ and the correlation length as $l_\rho = 10$. The calculated values are added to the z-coordinate of each STL point, and finally the part model with both systematic and random out-of-plane deviations is obtained. Figure 4.6(a) shows the calculated random deviations and 4.6(b) shows the final part model.

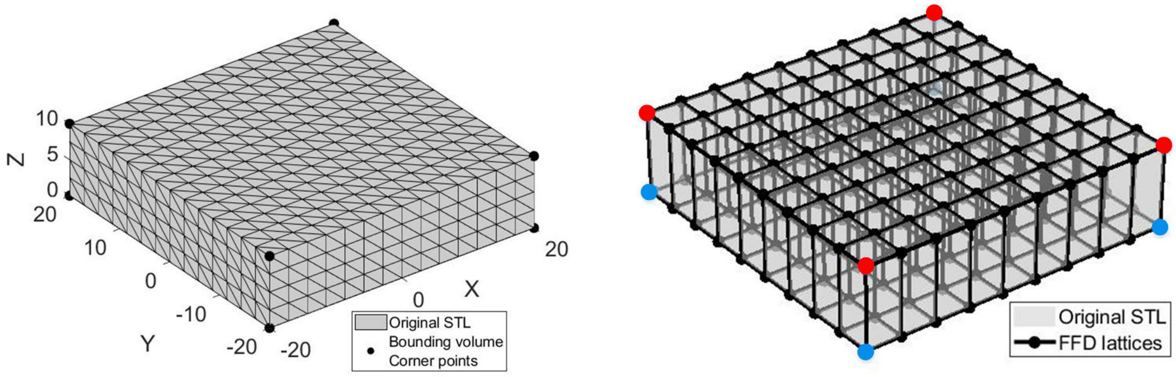

(a) Nominal STL representation and the bounding volume

(b) FFD lattice structure defined on the bounding volume

Figure 4.4: STL representation of the part and the FFD lattice structure defined on its bounding volume

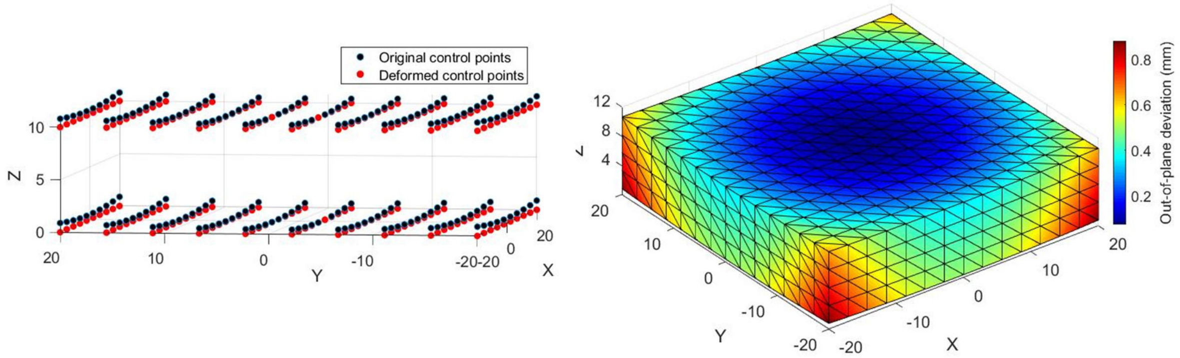

(a) Deformation of control points

(b) Out-of-plane deviation of part surface calculated by FFD

Figure 4.5: Deformation of control points and the deformed STL incorporating the calculated out-of-plane deviations

4.2.6 Discussion

In this section, some empirical out-of-plane deviation models are discussed. The prescriptive method operates on the SCS by subdividing the whole part model into vertical cross sections. Bayesian inference is adopted to fit a parametric function that represents deviations at each cross section. The obvious limitation is that it could only be applied to parts that have uniform vertical cross sections. And the deviation function has to be completely redesigned if the cross section shape changes. On the other hand,

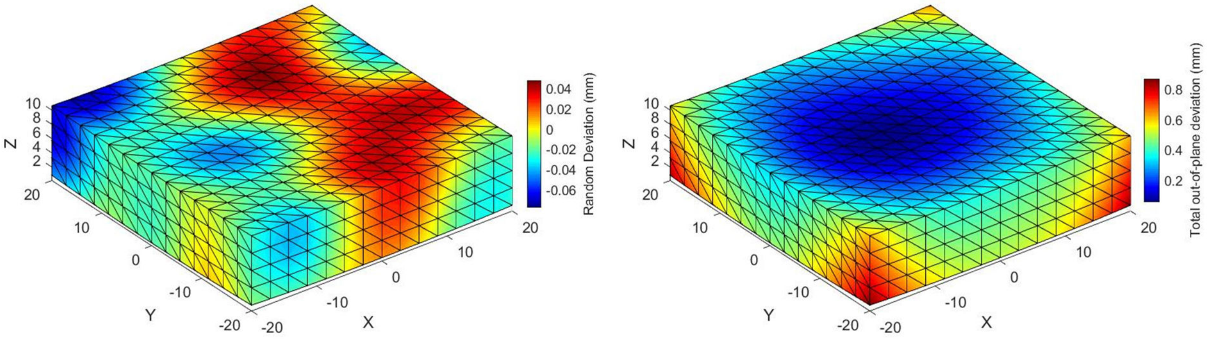

(a) Random deviations calculated on part surface using random field

(b)Total out-of-plane deviations

Figure 4.6: Random deviations calculated by random field and the total out-of-plane deviation on part surface

some existing works that focus on modeling the warpage effects provide a systematic solution to modeling the out-of-plane deviations. The empirical functions describing the warpage considering process parameters and material properties can be used to predict the systematic deviations at local sections of the part surface, such as the top and bottom layers. Through FFD, the local deviations are propagated to the whole product surface. Moreover, the random field method is used to model the random deviations at each layer. The combination of systematic and random deviations realizes the early prediction of out-of-plane deviations for the whole part surface in the design stage.

4.3 Layer-wise modeling of out-of-plane deviation by statistical modal analysis

The previous section discussed the approaches to modeling of systematic and random out-of-plane deviations. They can be used in the Prediction Stage as empirical predictive models but are limited to simple shapes and fixed process conditions. With varied objectives, the studies focus on deviation of the overall external part surface with thin-plate rectangular shapes or rotation symmetric shapes. However, it is important to realize that the geometric deviations are actually a result of accumulated deviation of each layer, a deeper investigation into the layer-wise behavior could facilitate understanding of the deviation patterns. On the way to this goal, a data-driven approach will be proposed in this section to model the out-of-plane deviation of the SLM process based on FEA and statistical modal analysis (SMA). The method enables the layer-level deviation prediction with consideration of the effects from part and process parameters. A case study is presented to validate performance of the method.

4.3.1 The framework

To conclude from current research status, the major challenges in out-of-plane deviation modeling can be stated as follows:

- The deviation of a fabricated layer can hardly be observed from the measurement data, since the internal layer geometry is neither visible nor accessible with common measurement devices.
- The pattern and magnitude of out-of-plane deviation may vary among parts manufactured under various process settings and among different layers of one part [CWT18, RP07]. On the other hand, as the part size varies, the magnitude of deviations also demonstrates substantial difference [CWT18, SPR12]. Hence, a high-fidelity predictive model should account for these effects.
- The complex deviation sources hardly allows for an analytical deviation model respect to the concerned process parameters.

In face of such challenges, we propose to use FEA to obtain the internal layer deviation data and derive a layer-level data-driven model considering effects of design and process parameters. As shown in Figure 4.7, the proposed method starts from an experimental design procedure, in which a number of parameter combinations $\boldsymbol{p} = (p^1, p^2, p^3, p^4)$ are selected for the design and manufacturing of experimental parts. In this thesis, the considered process parameters are layer thickness (p^1), laser power (p^2) and scan speed (p^3). The size of part is denoted by p^4 and the layer height h is used to identify the different layers of a part. The choice of these parameters is made based on reports about their effects on part distortions. The main contributor to the out-of-plane deviation is the high tensile residual stresses induced by the thermal effects [LLG17]. Within the powder-bed AM process, both the laser power and scan speed has an impact on energy density of the laser beam and consequently the thermal gradient of the part [SPR12]. The significant influence of layer thickness on residual stresses of the SLM process is also reported in [LLG17, MZD17]. These parameters are shape-independent and applied in the simulation model as a global setting, which makes them well-suited to be included in a statistical model. Other parameters, for example those related to the scanning strategy, need to be considered together with the specific scan patterns at each layer. Therefore, they are not included in this research and are kept as constants for all simulated parts.

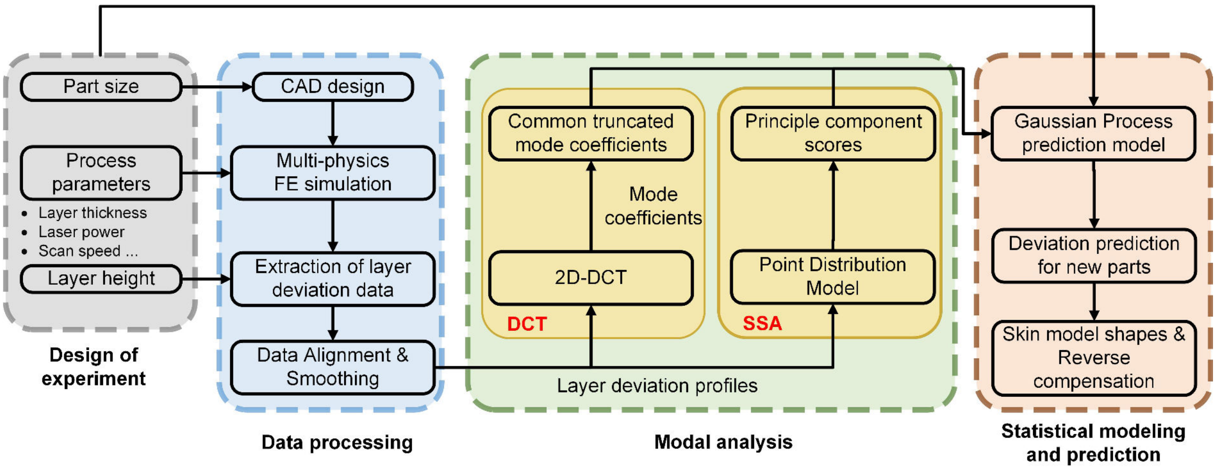

Figure 4.7: General framework of the proposed deviation modeling approach

Next, in the data processing stage, to obtain reliable deviation data of each fabricated layer, thermo-mechanical FEA is conducted on a proprietary AM simulation package following the parameters selected in experimental design. The layer-wise out-of-plane deviation data are extracted from the simulation results at specific layer height h and further organized as deviation profiles that describe the out-of-plane deviation of each layer.

To account for discontinuities in part geometry and to align the deviation profiles to a uniform structure, data smoothing should be performed. Based thereon, the patterns within these deviation profiles are identified through modal analysis. To this end, two approaches are investigated, namely Discrete Cosine Transform (DCT) and Statistical Shape Analysis (SSA). The identified deviation modes are represented by mode indicators, e.g., mode coefficients in DCT and principle component scores in SSA. Both of these approaches have been discussed in literature with respect to geometric deviation modeling [HC02, MCHR10, LLH10, HLC+14] and the SMS [ZAS+13, SAMW14, LZDS18], but rare attempts have been made to study the effects of process parameters on the identified deviation modes, especially in the scope of AM. Therefore, a Gaussian Process (GP) model is proposed to statistically characterize these effects. The parameter sets selected through experimental design as well as the derived mode indicator values compose the data for training the GP model, leading to a predictive model that could make predictions on new part deviations.

The method enables layer-level deviation prediction with consideration of the effects from part size and process parameters, and can be used for modeling the layer-per-layer out-of-plane deviation of SMS and through reverse compensation, the geometrical consistency between design and manufacture part can be significantly improved.

4.3.2 FE simulation of AM process

Data-driven methods pose a need for plenty of observation data for statistical modeling training. However, the time-consuming manufacturing and measurement process even for a single part hardly allows for massive data collection from real manufactured parts. Meanwhile, AM simulation offers the possibility to conduct straightforward virtual manufacturing given settings of machine and process parameters. Most solutions transform the STL into an FE mesh containing hexahedral elements, also known as voxels, to facilitate computation. So the simulation results are provided in a regular data structure, from which users could extract important in-process and post-process information. Besides, since the simulated deviation data are associated with each element of the FE mesh, the deviation of internal layer geometry is also accessible.

Therefore, AM process simulation is conducted on a proprietary software package Ansys Additive® for data collection. Through experimental design, N_p parameter combinations $\boldsymbol{p} \in R^{N_p \times 4}$ are selected for the simulation of a specific shape, then CAD models of parts of this shape are designed with the selected sizes p^4 and the tessellated STL files are obtained as simulation input. The process parameters (p^1, p^2, p^3) are set following the selected combinations. In the simulation process, the triangular mesh in STL is converted into a voxel representation with a specified voxel size, on which thermo-mechanical analysis is conducted. The simulation outputs are provided in a binary file consisting the coordinates of voxel points and the resulting deviations along x, y and z at each voxel point. The layer-wise out-of-plane deviation data are collected from this file as $\Delta z(x, y)$, where (x, y) is the 2D coordinate of voxel point on a layer, to which Δz is associated. Suppose for each simulated part, N_l layers of deviation data are extracted at varying layer height h, a total number of $N_{pl} = N_p * N_l$ deviation data can be obtained, corresponding to different combinations of $(\boldsymbol{p}, h)$.

4.3.3 Deviation profile smoothing with Discrete Smooth Interpolation

For parts of different sizes, the obtained deviation data may be distributed at varied number of voxel points. Figure 4.8(a) shows the out-of-plane deviation data of two example parts obtained from the simulation result, in which the color intensity indicates the magnitude of deviation values on voxel points. To enable correspondences for modal analysis, especially for performing DCT, data of all involved layers are mapped to a uniform $M \times N$ grid structure, regardless of the actual size and shape of layer geometry. For a specific layer, this is done by finding an axis-aligned bounding rectangle that fully encloses all the voxel points and subdividing the rectangle with M nodes along x-dimension and N nodes along y-dimension. The out-of-plane deviation values on these nodes are obtained based on the known values on voxel points, as shown in Figure 4.8(b). Suppose the distance between grid points in both x and y direction is set as $\delta_x = \delta_y = 1mm$, this grid structure can be seen as a 2D shape. Adding the sampled out-of-plane deviations to points of the 2D shape in z direction, the deviation profile is obtained as $(x_m, y_n, \Delta z(x_m, y_n)); m = 0, \cdots, M-1; n = 0, \cdots, N-1$, as shown in Figure 4.8(c). This profile enables an intuitive perception of how deviations are distributed on the layer and can be treated as a "shape" of deviations.

Whereas, the geometry of an AM fabricated layer is always complex and the resulting voxel structure is not regular enough to assign values on all points of the rectangular grid, thus causing non-continuity issues at empty grid points that may result in undesired modes and add to the difficulty in identifying the most significant modes that we are concerned with. For instance, in Figure 4.8(a), a clear discontinuity can be observed in the deviation profile of the cylindrical part at the boundary of square shape. In addition, the grid interval may not be consistent with the voxel side length, making it difficult to realize one-to-one mapping between the voxel data and grid data, as seen in Figure 4.8(b). Therefore, before performing modal analysis, a pre-processing procedure is needed to interpolate each grid point (x_m, y_n) of the deviation field with appropriate deviation values $\Delta z(x_m, y_n)$, given the data $(x_0, y_0, \Delta z_0(x_0, y_0))$ obtained from the simulation result. At the same time, in order to guarantee sufficient smoothness, this procedure can be justifiably treated as a surface modeling problem by transforming

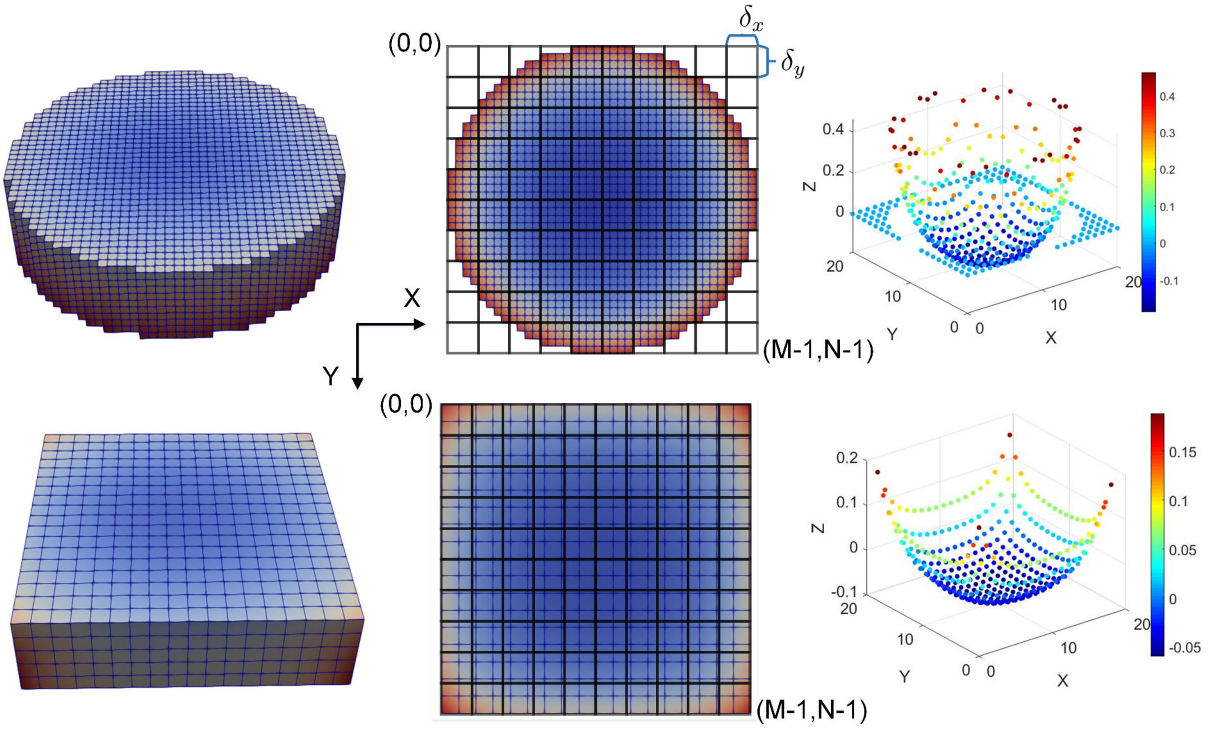

(a) Simulation Output- Z deviation

(b) Sampling layer-wise deviation data with the grid

(c) Out-of-plane deviation profile on grid

Figure 4.8: Deviation profile extraction from simulation results

the target deviation profile into a surface S whose points are $(x_m, y_n, \Delta z(x_m, y_n))$. The connectivity between points is obtained through Delaunay triangulation and represented as $F(S)$. As a surface modeling algorithm that has been widely used in geometric modeling and geology, Discrete Smooth Interpolation (DSI) has demonstrated good performance in dealing with discontinuities [Mal89], thus will be adopted in this thesis for smoothing the deviation profile. DSI treats the surface as a 2D graph and smoothly interpolates the surface nodes based on their graph connectivity $F(S)$ and geometric constraints [Mal92]. Specific to our problem, two kinds of geometric constraints are available: for grid points that are coincident with the voxel points, the deviation values are directly known (known point constraint); for other grid points, their values can be interpolated from $P(x_0, y_0, \Delta z_0(x_0, y_0))$ as control points (control point constraint).

Denote Ω as the graph nodes of S, the out-of-plane deviation of the nodes is defined by a set of functions $\eta(k), k = 1, ...K$, where $K = M * N$ is the number of nodes. According to the first constraint, Ω can be further divided into two subsets: Ω^0 and Ω^1, where the deviations $\eta(\Omega^0)$ are known and $\eta(\Omega^1)$ are to be interpolated. Among all sets of possible functions $\eta(k)$ for Ω, DSI attempts to find one that minimizes a generalized roughness criterion defined as:

$$R^*(\eta) = \sum_{k\in\Omega} \mu(k)R(\eta\,|k) + \sum_{i} \omega_i \rho(\eta\,|\Lambda_i) \tag{4.5}$$

, where $R(\eta|k)$ denotes a local roughness function at node k and is measured with respect to the neighboring nodes of k; $\rho(\eta|\Lambda_i)$ measures the degree of violation of $\eta(k)$ with respect to linear constraints Λ_i; $\mu(k)$ is a positive parameter that modulates the contribution of $R(\eta|k)$ and ω_i s a positive 'certainty factor' weighting the relative importance of each constraint. Both $\mu(k)$ and ω_i are set as 1 to assign equal importance to the geometric information. The components $R(\eta|k)$ and $\rho(\eta|\Lambda_i)$ respectively account for the aforementioned geometric constraints and their mathematical formulation is given as:

$$\begin{aligned} R(\eta\,|k) &= \left| \sum_{\alpha\in N(k)} v^\alpha(k)\eta(\alpha) \right|^2 \\ \rho(\eta\,|\Lambda_i) &= \left| \sum_{\alpha\in\Omega} A_i(\alpha)\eta(\alpha) - b_i \right|^2 \end{aligned} \tag{4.6}$$

, where $N(k)$ are the neighboring nodes of node k that could be retrieved from graph connectivity $F(S)$, and $v^\alpha(k)$ is the weighting parameter calculated from the neighborhood. (A_i, b_i) are coefficients that fully define Λ_i, which is specified following the control point constraints. As shown in Figure 4.9, for a given control point P and a given direction D, a triangle $T(\eta(\alpha_0), \eta(\alpha_1), \eta(\alpha_2))$ can be found on S that intersects with the line containing P and parallel to D. And the control point constraint is to ensure that during the interpolation process, the intersection point p shall be coincident with P. Therefore, numbers of control point constraints can be imposed and the directions are determined as the positive or negative z-direction according to the relative position between the control points and the surface. The details of the control point constraint and the calculation of coefficients (A_i, b_i) can be found in [Mal89].

According to Mallet et al., a unique solution η^* exists that minimizes the generalized roughness function if the following conditions are met [Mal89]:

- Ω^1 is a non-empty set.
- $\begin{cases} v^\alpha(k) > 0, \forall\alpha \in N(k) \\ v^k(k) = -\sum_{\alpha\in N(k)} v^\alpha(k) \end{cases}$, where $N(k)$ are the neighboring nodes of node k that

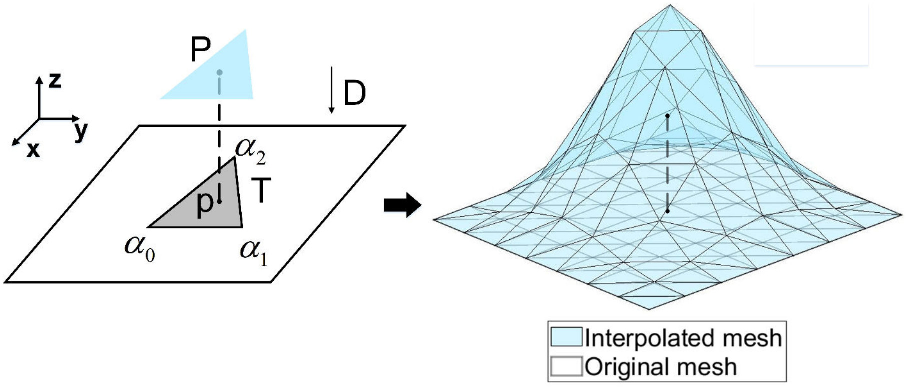

Figure 4.9: The control point constraint in DSI

could be retrieved from graph G.

- $\begin{cases} \mu(k) > 0, \forall k \in \Omega \\ \omega_i > 0, \forall i \end{cases}$

Apparently Condition 1 and 3 are already met. Condition 2 can also be satisfied by setting an appropriate form of $v^{\alpha}(k)$. With all the defined concepts, the solution to an optimum interpolation is achieved if $\partial R^*(\eta)/\partial\eta(k) = 0$ for all $k \in \Omega$, yielding the following equation:

$$\eta(k) = -\frac{G(k) + \Gamma(k)}{g(k) + \gamma(k)} \tag{4.7}$$

, where $G(k), g(k)$ are dedicated to the minimization of the local roughness at node k and $\Gamma(k), \gamma(k)$ to the minimization of violation of the control point constraints imposed on k. The complete form of these functions can be referred to in [Mal97], and will not be discussed in detail in this thesis.

As illustrated in Algorithm 1, the final deviation values of unknown nodes are determined by iterating Equation 4.7 starting from an arbitrary initial solution. This iterative process has been proved to converge to the unique solution if the conditions of uniqueness are satisfied. As illustrated in Algorithm 1, the final locations of unknown nodes are determined by iterating Equation 1 on all the unknown nodes starting from an arbitrary initial solution. This iterative process has been proved to converge to the unique solution if the conditions of uniqueness are satisfied.

After implementing DSI on all the N_{pl} layers of deviation data, a smooth deviation profile is achieved for each layer in which all points of the rectangular grid have been assigned meaningful deviation values so that modal analysis could be more efficiently conducted. Figure 4.10 shows an example of the application of DSI on a planar surface

Algorithme 1 DSI algorithm

```
Inputs: deviation values of known nodes $\eta(\Omega^0)$, connectivity graph $G$, coefficients $\mu(k), v^\alpha(k))$
Outputs: interpolated deviation values on unknown nodes $\eta(\Omega^1)$
$\eta(\Omega^1) \leftarrow$ arbitrary initial solution
while more iterations are needed do
    for all $\alpha \in \Omega^1$ do
        $\eta(\alpha) = -\frac{G(\alpha)+\Gamma(\alpha)}{g(\alpha)+\gamma(\alpha)}$
    end for
end while
```

composed of a triangulated grid structure. It can be observed that, following the control point constraints, the planar surface has been smoothed with all the points assigned appropriate deviation values.

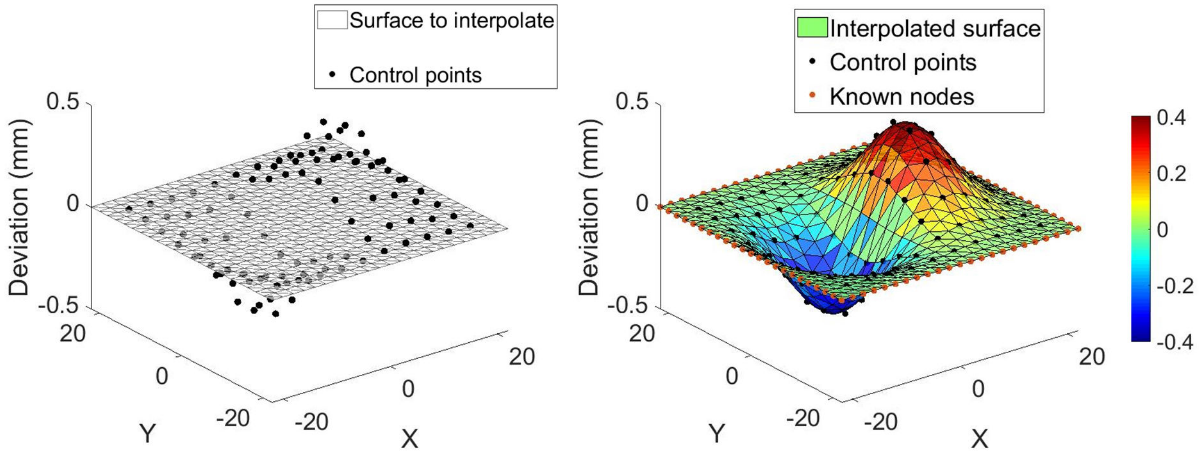

(a) (b)

Figure 4.10: (a) DSI control points and the surface before interpolation; (b) the surface interpolated with DSI

4.3.4 Identification of deviation patterns with modal analysis

In this section, the obtained N_{pl} deviation profiles are processes by modal analysis methods, including DCT and SSA, to identify the deviation modes. The identified modes are expressed with mode indicators that measure the mode significance. In the following, the principles of both methods and the derivation of mode indicators will be explained.

4.3.4.1 Modal analysis with DCT

DCT is a technique that represents a finite sequence of data points as an accumulation of cosine functions with different frequencies [ANR74] and has been massively applied in image and audio processing. In terms of manufacturing variation modeling, the DCT was originally introduced by Huang et al. [HC02] to develop a general form deviation model by identifying the most significant deviation modes. The out-of-plane deviation of an AM-fabricated layer, denoting deviation of the layer from the nominal plane in the build direction, can actually be treated as a form deviation.

Thus, the out-of-plane deviation field $f(m,n) = \Delta z(x_m, y_n)$ can be similarly defined at sample points $(x_m, y_n) = (m\delta_x, n\delta_y)$ distributed on a regular grid along x and y axes of the nominal layer plane, where δ_x, δ_y denote the sampling density and should be adaptively set with respect to the actual size of shape. $m = 0, .., M-1; n = 0, .., N-1$ is the location of the sample point on the grid. Two assumptions are made to simplify the DCT modeling process [HC02]:

- *Smoothness assumption*: the deviation of the layer plane is highly spatially correlated, thus guaranteeing a sufficient smoothness of the deviation field signal, and high-frequency components within the signal (such as surface roughness or waviness) are small enough to be ignored.
- *Height field assumption*: the deviation can be expressed as a single-valued height field function that is defined within the 2D domain, as we did in defining $f(m,n)$.

By performing DCT, the sampled deviation data are transformed into the spatial frequency domain, from which a series of deviation modes can be identified, each representing a typical form of deviation pattern. Likewise, an inverse transformation can be conducted to reconstruct the original deviation data from the identified modes. The forward and inverse transformation routines are given as:

$$\begin{aligned}
&C(u,v) = \sum_{m=0}^{M-1}\sum_{n=0}^{N-1} f(m,n)g(m,n,u,v), f(m,n) = \sum_{u=0}^{M-1}\sum_{v=0}^{N-1} C(u,v)g(m,n,u,v) \\
&g(m,n,u,v) = \frac{1}{\sqrt{M}}\frac{1}{\sqrt{N}}\alpha_u\alpha_v \cos\frac{(2m+1)\pi u}{2M}\cos\frac{(2n+1)\pi v}{2N} \\
&\alpha_{u|v} = \begin{cases} 1, u|v = 0 \\ \sqrt{2}, u|v \neq 0 \end{cases}
\end{aligned} \tag{4.8}$$

, where $C(u,v)$ are DCT coefficients denoting the contribution of an error mode with space frequency (u,v) on the two axes. The advantage of applying the DCT for deviation modeling lies in its ability to parameterize the deviations with mode coefficients, and moreover, through truncation, only a small number of the most significant modes need to be preserved in order to satisfy a specified modeling accuracy. Since the contribution of each mode is measured by the magnitude of its corresponding coefficient, an energy significance mode truncation criterion (ESC) can be defined for a given energy preservation ratio $\delta_E \in [0,1]$:

$$\frac{\sum_{\Psi_E} C^2(u,v)}{\sum\limits_{m=0}^{M-1}\sum\limits_{n=0}^{N-1} f^2(m,n)} \geq \delta_E; (u,v) \in \Psi_E \tag{4.9}$$

, where Ψ_E is a minimum set of significant modes that could preserve δ_E of the energy in the original deviation field. Another truncation criterion is the Hausdorff Distance Criterion (HDC) which conveys more geometric information [HLC+14]. Among all sets of modes, HDC keeps the one Ψ_H that contains the minimum number of modes while ensuring that the Hausdorff distance between the original field $f(m,n)$ and the field $f_{\Psi_H}(m,n)$ reconstructed from these modes falls below a threshold δ_H: $d(f(m,n), f_{\Psi_H}(m,n)) \leq \delta_H$, where $d(\cdot,\cdot)$ is the Hausdorff distance operator. Here a combined criterion is adopted and defined as the intersection between the two sets satisfying ESC and HDC respectively: $(u,v) \in \Psi_C = \Psi_E \bigcap \Psi_H$. As long as this criterion is met, the complete model can be truncated to a subset of deviation modes, and $f(m,n)$ as defined in 4.8 can be approximated as a function of the truncated mode coefficients $\boldsymbol{C} = \{C(u,v)\}_{u,v\in\Psi_C}$. Now the deviation profile of a layer is represented as Equation 4.10, where $\varepsilon(m,n)$ denotes the residuals that are not explained by the truncated modes and can be ignored if a high accuracy of reconstruction is reached.

$$f(m,n,\boldsymbol{C}) = \sum_{u,v\in\Psi_C} C(u,v)g(m,n,u,v) + \varepsilon(m,n) \tag{4.10}$$

Through modal analysis, the deviation profile could be parameterized by the coefficients of a small number of truncated modes on condition that these modes could preserve sufficient information of the original deviation data, and as a consequence, the deviation modeling problem is reduced to the modeling of the mode coefficients $\boldsymbol{C}$, as illustrated in Figure 4.11.

Among all the modes identified from all the N_{pl} profiles, it is possible to recognize a

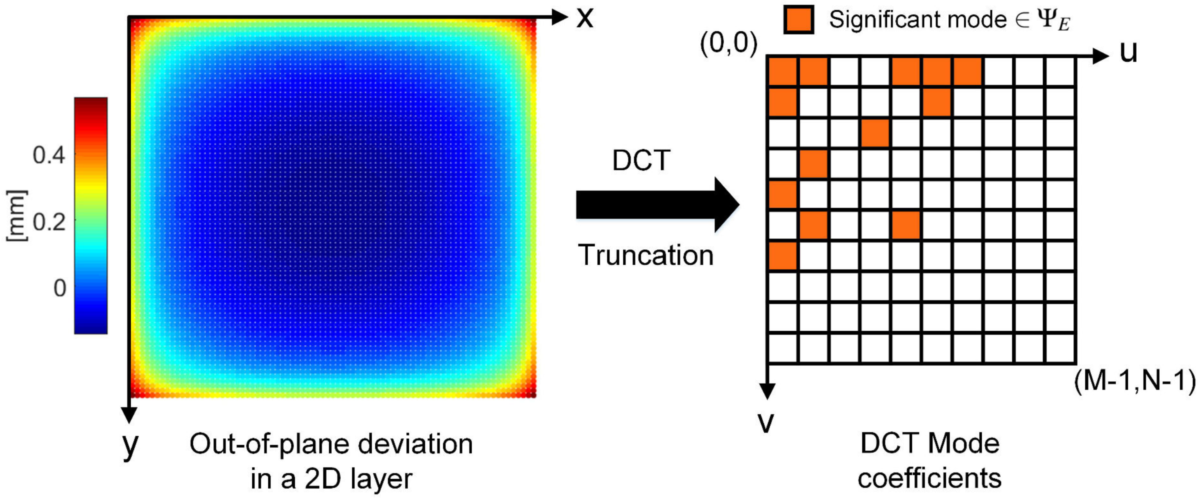

Figure 4.11: Identification of significant modes

common set of modes that are significant across all profiles and some trivial modes that are only significant for individual profiles, thus composing a mode union Π^c containing N_c different modes, as shown in Figure 4.12. The corresponding mode coefficients of Π^c can also be recognized, and represented as a $N_{pl} \times N_c$ matrix whose (i, j)-th entry denotes the coefficient of Mode j on profile i, as shown in Equation 4.11.

$$\boldsymbol{C} = \begin{bmatrix} C_{11} & C_{12} & \cdots & C_{1N_c} \\ C_{21} & C_{22} & \cdots & C_{2N_c} \\ \vdots & \vdots & \ddots & \vdots \\ C_{N_{pl}1} & C_{N_{pl}2} & \cdots & C_{N_{pl}N_c} \end{bmatrix} \tag{4.11}$$

Each column $\boldsymbol{C}_j \in R^{N_{pl}}$ of the matrix contains the coefficients of one mode observed on all the experimented layer deviation profiles and is treated as the response to the $R^{N_{pl}\times 4}$ parameter data set, altogether they compose the training data $(\boldsymbol{p}, h, \boldsymbol{C}_j)$ for the consequent statistical modeling process.

4.3.4.2 Modal analysis with SSA

SSA refers to a set of techniques to investigate the geometrical properties of shapes using statistical methods. It is widely adopted in computer vision and medical image processing. In the engineering domain, SSA has been applied by several researchers to model geometric shape variations [MCHR10, WLLS14]. In the observation stage of SMS, SSA has also been implemented with the KDE-PDM method (2.3.3.2) to capture

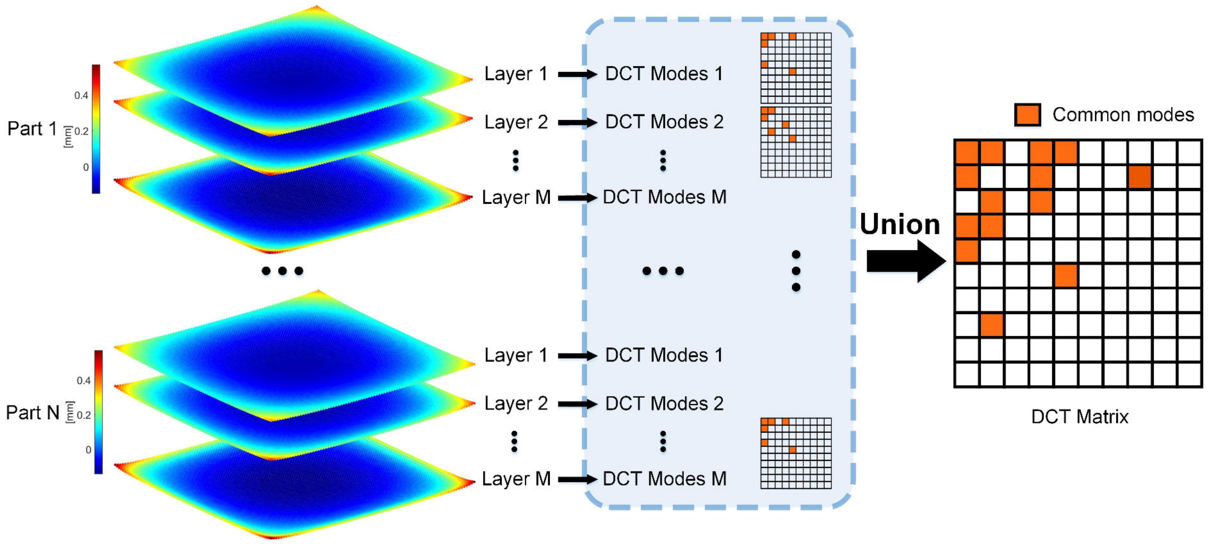

Figure 4.12: Significant mode identification from deviation data of multiple part layers

the statistical distribution of major deviation models within a number of manufactured shapes [SAMW14]. The same Point Distribution Model (PDM) is adopted in this section to conduct modal analysis on the out-of-plane deviation profiles.

In Section 4.3.3, we have obtained deviation profiles for N_{pl} layers of deviation data corresponding to different parameters $(\boldsymbol{x}, h)$. The objective of SSA is to identify the main patterns (or variation modes) within these deviation profiles.

The general procedure of SSA is as follows [SG02]:

- *Training set acquisition.* The deviation profiles to be analyzed are acquired as the training shapes for SSA.

- *Correspondence determination.* The correspondence between training shapes is determined by recognizing and associating corresponding points on each shape.

- *Shape Alignment.* The differences between training shapes in terms of location, scale and rotational effects are corrected. Since all the deviation profiles are based on a common grid structure, the correspondence can be easily determined and alignment is not needed.

- *Statistical Shape Model(SSM).* Based on the aligned training shapes, an appropriate SSM is established for shape analysis. In this paper, the Point Distribution Model (PDM) will be adopted.

Developed by Cootes et al. [CTCG95, CET01], PDM has been recognized as the fundamental model for statistical study of shape [DTA+03]. The rationale behind PDM is to represent each of the training shapes as a mean shape combined with variations of the mean shape along the main variation modes. To start with, the coordinates of each aligned deviation profiles are reorganized as a vectorized representation

$$\boldsymbol{X}_i = [x_1, x_2, \cdots, x_{M_p}, y_1, y_2, \cdots, y_{M_p}, \Delta z_1, \Delta z_2, \cdots, \Delta z_{M_p}]^T; i = 1, \cdots, N_{pl}$$

, where M_p is the number of points in the deviation profile which is identical to the number of grid points $M * N$, and $\Delta z_j = \Delta z(x_j, y_j)$ is the out-of-plane deviation. A mean shape is considered as $\bar{\boldsymbol{X}} = \sum_{i=1}^{N_{pl}} \boldsymbol{X}_i / N_{pl}$, and the shape covariance matrix is given by $\Sigma_{\boldsymbol{X}} = \sum_{i=1}^{N_{pl}} (\boldsymbol{X}_i - \bar{\boldsymbol{X}})(\boldsymbol{X}_i - \bar{\boldsymbol{X}})^T / N_{pl}$. The identification of variation modes is realized through Principle Component Analysis (PCA) on the shape data $\boldsymbol{X}$, the steps of PCA are as follows:

- Calculate the eigenvectors $\boldsymbol{V}$ and eigenvalues $\boldsymbol{\lambda}$ of the covariance matrix $\Sigma_{\boldsymbol{X}}$.
- Rearrange the eigenvector/eigenvalue pairs in descending order according to the eigenvalues. Each eigenvalue indicates the amount of variance of the original data explained by its corresponding principle component. Therefore, given a threshold ratio, a subset of t components needs to be retained to explain a considerable amount of variance in the original data.

$$\arg\min_t \left(\frac{\sum_{i=1}^{t} \boldsymbol{\lambda_i}}{\sum_{j=1}^{N_{pl}} \boldsymbol{\lambda_j}} \geq ratio \right) \tag{4.12}$$

- Transform the original shape to the reduced t-dimensional space and compute the its scores as $\boldsymbol{s}_i = \boldsymbol{V}_t^T (\boldsymbol{X}_i - \bar{\boldsymbol{X}}) \in R^t$, where $\boldsymbol{V}_t$ is the matrix composed of the eigenvectors of the first t principle components.
- The original shape can be approximated as

$$\boldsymbol{X_i} \approx \bar{\boldsymbol{X}} + \boldsymbol{V}_t \boldsymbol{s}_i \tag{4.13}$$

The scores represent the distribution of a layer's deviation profile in the reduced PCA space. Similar to the DCT-based method, a $N_{pl} \times t$ matrix is organized as Equation 4.14, in which the (i, j)-th entry denotes the j-th principle component score of profile i in the PCA space and each column $\boldsymbol{s}_j \in R^{N_{pl}}$ contains the scores of one principle component on all the deviation profiles. Since each profile corresponds to a part layer manufactured under a specific design and process parameter setting, therefore, $\boldsymbol{s}_j$ is treated as the response to the $R^{N_{pl}\times 4}$ parameter data set, thus composing the training data $(\boldsymbol{p}, h, \boldsymbol{s}_j)$.

$$\boldsymbol{s} = \begin{bmatrix} s_{11} & s_{12} & \cdots & s_{1t} \\ s_{21} & s_{22} & \cdots & s_{2t} \\ \vdots & \vdots & \ddots & \vdots \\ s_{N_{pl}1} & s_{N_{pl}2} & \cdots & s_{N_{pl}t} \end{bmatrix} \tag{4.14}$$

4.3.5 Predictive model building with Gaussian Process

As has been stated by Huang et al. [HC02], the modes identified by modal analysis are closely related to typical deviation patterns and the patterns are characterized by some indicators, namely the mode coefficients in DCT and the principle component scores in SSA. Unlike traditional manufacturing processes whose deviation patterns illustrate clear relationship with the deviation sources and could be analytically modeled by investigating the characteristics of the sources, the sources in AM process are far more complex, thus one-to-one mapping between the sources and the identified modes cannot hardly be established.

Therefore, based on the training data from modal analysis, a Gaussian Process model is proposed in this section which statistically investigate the effect of parameter setting on the mode indicators. Through effective training of the model, given any new parameter setting, the deviation profile of the manufactured layer can be predicted and the geometric deviations can be derived.

GP has been recognized by the machine learning community as a supervised learning approach that could make prediction on new inputs by measuring the similarity between the points among training data. To facilitate model description, here I_j is used to denote the mode indicator, either the mode coefficient $C_j, j = 1, \cdots, N_c$ or PCA score $s_j, j = 1, \cdots, t$. For each identified mode indicator, a GP model can be established as:

$$I_j(\boldsymbol{p}, h) = \mu_j(\boldsymbol{p}, h) + Z_j(\boldsymbol{p}, h) \tag{4.15}$$

, where $\mu_j(\boldsymbol{p}, h)$ serves as a mean function that models the global effect of input parameters on an indicator and $Z_j(\boldsymbol{p}, h)$ is a zero-mean GP which captures the non-linear effects that are beyond interpretability of the mean function. $\mu_j(\boldsymbol{p}, h)$ is considered as a linear combination of a series of basis functions and represented as $\mu_j(\boldsymbol{p}, h) = \boldsymbol{\beta}^T \boldsymbol{\Phi}(\boldsymbol{p}, h)$, where

$$\boldsymbol{\Phi}(\boldsymbol{p}, h) = (1, h, .., p^a, .., h^2, ..(p^a)^2, .., hp^a, .., p^a p^b, ..); a, b = 1, ..., 4 \tag{4.16}$$

are the first- and second-order monomials of $\boldsymbol{p}$ and h; $\boldsymbol{\beta}$ are the coefficients. This typical form of mean function is designed to measure the individual, quadratic and interaction effects between the input parameters. In practice, the function can be reduced by removing some unnecessary components through regularization. Here the Lasso algorithm [Tib96] is used which conducts both regularization and regression on the function parameters $\boldsymbol{\beta}$ and gives an optimal estimation as $\hat{\mu_j}(\cdot, \cdot)$. The covariance function of the GP model is quite critical since it measures the correlation between inputs. A variant of the 'radial basis function (RBF)'-based covariance is selected as Equation 4.17.

$$\begin{aligned} & k((\boldsymbol{p}_1, h_1), (\boldsymbol{p}_2, h_2)) \\ & = \sigma_f^2 \exp \left[-\sum_{l=1}^{4} \lambda_l (p_1^l - p_2^l)^2 - \lambda_0 (h_1 - h_2)^2 \right] \end{aligned} \tag{4.17}$$

The hyper-parameters $(\lambda_0, ..., \lambda_d)$ and σ_f are estimated following the maximum likelihood principle based on the training data $(\boldsymbol{p}, h, \boldsymbol{I}_j)$ and the optimal predictor for each mode coefficient is given as:

$$\hat{I}_j(\boldsymbol{p}, h) = \hat{\mu}_j(\boldsymbol{p}, h) + K_*^T K^{-1} (\boldsymbol{I}_j - \hat{\mu}_j(\boldsymbol{p}, h)) \tag{4.18}$$

, where $\hat{\mu}_j(\boldsymbol{p}, h)$ is the estimated mean; K_* is a N_{pl}-dimensional vector with the p-th element as $\hat{k}((\boldsymbol{p}_p, h_p), (\boldsymbol{p}, h))$; K is the $N_{pl} \times N_{pl}$ training set covariance matrix with the (a, b)-th entry as $\hat{k}((\boldsymbol{p}_a, h_a), (\boldsymbol{p}_b, h_b))$; $\hat{k}(\cdot, \cdot)$ is the RBF covariance function with the estimated hyper-parameters. The estimated GP functions $\{\hat{I}_j(\boldsymbol{x}, h)\}, j = 1, ..., N_c$ are consequently used to predict the deviation mode indicators for layers of any part built with new parameters $(\boldsymbol{p}^*, h^*)$. And through the inverse transformation of DCT $f(m, n, \hat{\boldsymbol{I}}(\boldsymbol{p}^*, h^*))$ (Equation 4.10) or the shape reconstruction of SSA $\boldsymbol{X_i} \approx \bar{\boldsymbol{X}} + \boldsymbol{V}_t \hat{\boldsymbol{I}}(\boldsymbol{p}^*, h^*)$ (Equation 4.13), the out-of-plane deviation profile is obtained. Recall that in Section 4.3.3, the smoothed deviation profile is defined on the grid as $\Delta z(x_m, y_n)$. Therefore, the deviation Δz_0 at points of the original layer geometry (x_0, y_0) can be conveniently obtained from the grid points (x_m, y_n) through techniques such as cubic spline interpolation, which has been widely adopted to map gridded data to query points. With a sufficient grid density, the interpolation can achieve a desirable accuracy.

Meanwhile, the out-of-plane deviations of layer contour points can be obtained from the predicted deviation profiles, laying the basis for building the SMS.

4.4 Application

In this section, a case study is presented to validate the proposed approach based on square shape parts. Latin Hypercube Design (LHD) is adopted to sample from 15 levels of each parameter and based thereon, $N_p = 15$ simulations are run for model training. Two extra simulations are conducted following two randomly generated parameter samples to test performance of the trained model. All simulations are performed on a mobile workstation equipped with a 2.40 GHz Intel Core i7 CPU, an 8 GB RAM and the Windows 10 operating system. The parameter setting of each simulation can be found in Tab. 4.1, in which the Time column lists the time consumed by each simulation and the Type column denotes whether the data are used for model training or testing.

Simulation *NO.*	*Part size* (mm)	*Layer thickness* (um)	*Laser power* (W)	*Scan speed* (mm/s)	*Time* (min)	*Type*
1	15	85	280	2400	14	Train
2	18	90	190	1600	16	Train
3	21	40	230	1300	91	Train
4	24	60	160	1700	30	Train
5	27	35	180	2100	83	Train
6	30	75	200	1000	158	Train
7	33	50	220	1900	75	Train
8	36	65	270	2200	51	Train
9	39	30	260	1400	706	Train
10	42	80	290	1800	187	Train
11	45	70	170	1100	362	Train
12	48	45	250	1200	661	Train
13	51	95	240	1500	354	Train
14	54	55	210	2000	139	Train
15	57	100	150	2300	195	Train
16	26	80	245	1850	40	Test
17	35	95	195	2250	54	Test

Table 4.1: Parameter values determined by experimental design for simulation

Following the part sizes specified in the *Part size* column, CAD part models are designed with a common height of $5mm$. Note that part size denotes the edge length of square shape parts. Simulations are run by setting the layer thickness, laser power and scan speed as corresponding values in the table while retaining a common setting for other parameters, for instance, material (Inconel 718), baseplate temperature (353K), hatch spacing (100um). The layer-wise deviation data are collected from each simulated part with a 1mm-interval from bottom to top layer, thus $N_l = 6$ layers of data are obtained for each part and $N_{pl} = 90$ layers in total.

The out-of-plane deviation profile of each part layer is further obtained on an $M(=20) \times N(20)$ rectangular grid with $1mm$ grid size and smoothed by DSI to ensure that the deviation data are aligned for parts of different sizes. In the following, the performance of both DCT and SSA will be discussed respectively.

4.4.1 Performance of the DCT-based method

DCT is performed with the combined mode truncation criteria, in which the energy preservation ratio is selected as 0.95 and the Hausdorff distance threshold as 0.03. Among the whole set of truncated modes, the most significant ones common for all the N_{pl} part layers are preserved, yielding $N_c = 15$ modes and their coefficients $\boldsymbol{C}$ serve as the response data for GP training. Figure 4.13 illustrates the first nine most significant modes. The deviation profiles of two sample layers reconstructed from these modes are also shown. It can be seen that with different coefficients, the same set of modes could represent different deviation patterns. The original out-of-plane deviation of sample layer 1 demonstrates an obvious upward curling at the four corners. The first 2 modes manage to capture this curling effect along x and y axes with an emphasis on the shape boundary. Mode 3 is to account for the global elevation of the layer in build direction. Mode 4, 6 and 9 modulate the magnitude of deviations along the two axes, and Mode 5, 7 and 8 characterize the significant difference between deviations of the shape boundary and the corners. Especially, the deviations of sample layer 2 show discrepancies between corners of the two diagonals, which can be captured mainly by Mode 2, 4, 5 and 7.

For each of the common mode coefficients, a GP model is constructed and trained with the predictors $(\boldsymbol{p}, h)$ and corresponding responses using a 5-fold cross validation. The trained model is tested on the two test parts, Figure 4.14 and Fig. 4.15 respectively

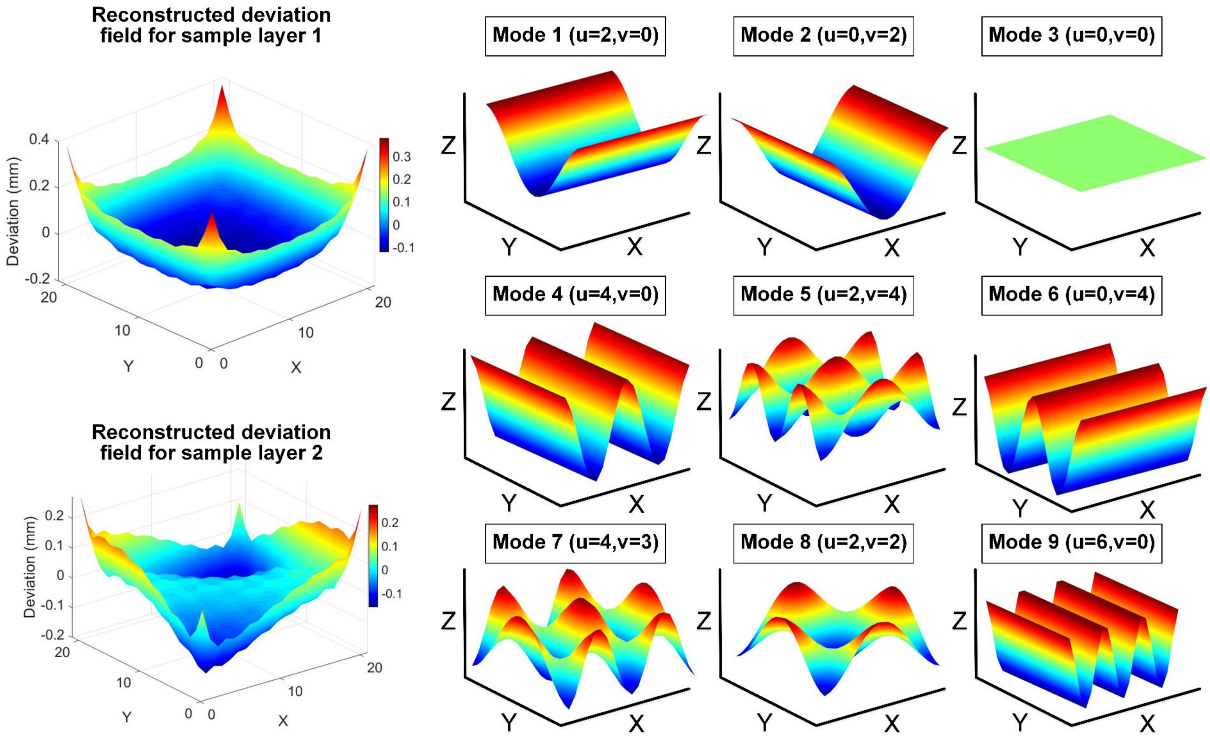

Figure 4.13: First nine most significant modes identified from the simulated deviation data

illustrate the prediction of deviation profiles on the 6 layers of test part $NO.16$ and $NO.17$. In both figures, the solid black dots denote the original out-of-plane deviation of points on the corresponding layer and the hollow dots are the mean prediction of deviations made by the proposed model. It can be observed that the mean prediction reaches a pretty close fitting to the original deviation. The GP models also provide the 95% prediction interval for each mode coefficient. After reconstruction of the deviation profiles from these coefficients, two bounds are derived around the mean as the confidence interval for deviation prediction, as represented by the cyan and brown surfaces in the figures. It's clear that a major portion of the original data falls within the interval, thus proving the effectiveness of the predictive model.

Moreover, to quantitatively evaluate the performance, the Root Mean Sum of Squares Error (RMSE) and R-square are calculated on each simulated part to measure the overall difference between the real and predicted data, as shown in Figure 4.16 and Figure 4.17. The RMSEs of predictions on both the training set and test set keep at a low level, and the R-square which measures the accuracy of fitting also maintains a high average value across the simulated parts. It's clear from both figures that, as the part size increases,

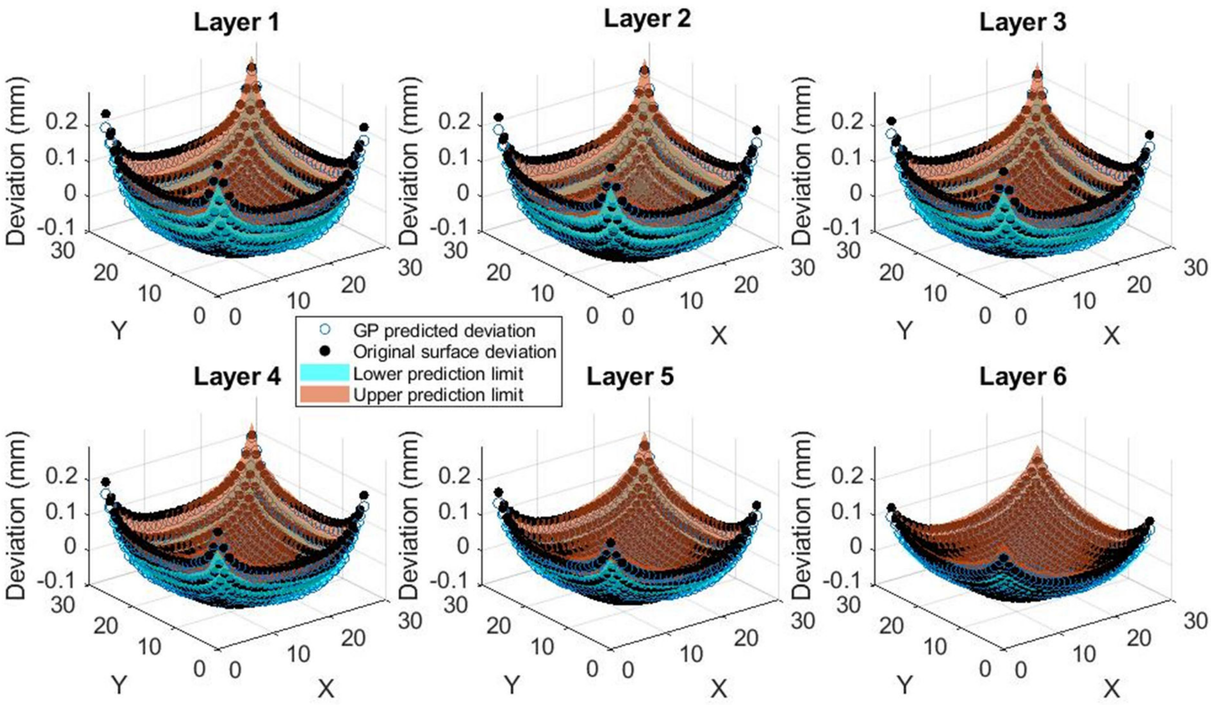

Figure 4.14: Out-of-plane deviation of layers of the test part ($NO.16$) predicted by GP with 95% confidence interval

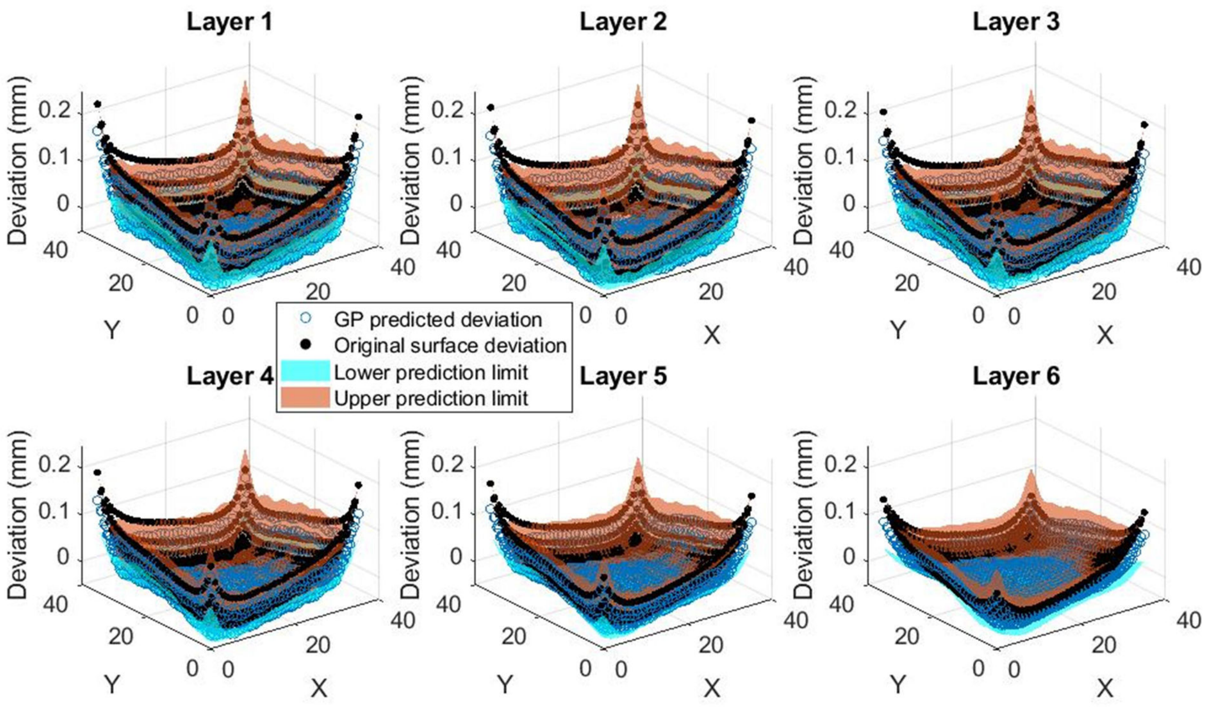

Figure 4.15: Out-of-plane deviation of layers of the test part ($NO.17$) predicted by GP with 95% confidence interval

the prediction accuracy shows a decreasing tendency. This is due to the fact that the deviation data are mapped to an identical grid structure, and for larger parts, some details will be lost after performing DSI. One possible solution is to increase the grid density at the cost of raising also the computational intensity.

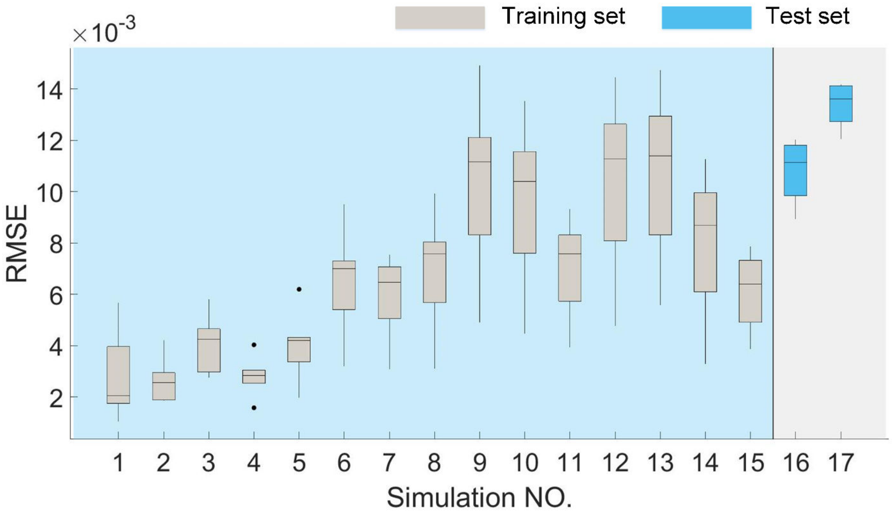

Figure 4.16: RMSE of predictions on layers of each part - DCT based method

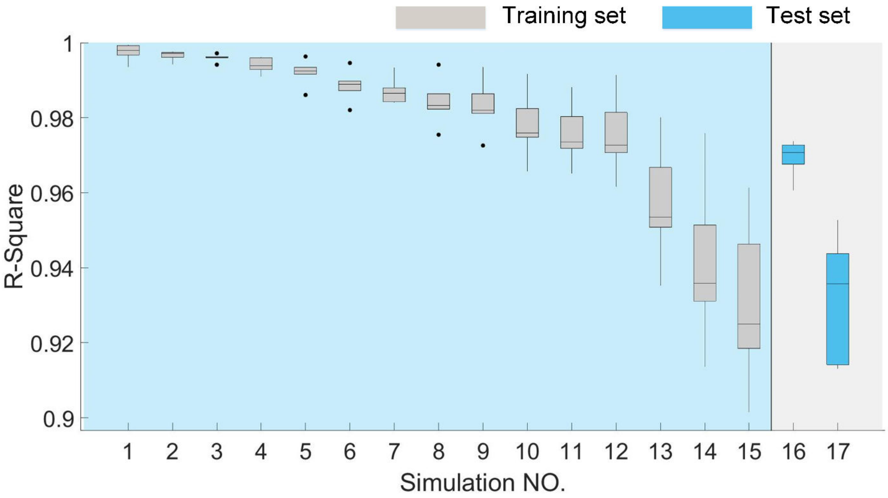

Figure 4.17: R-square of prediction on layers of each part- DCT based method

4.4.2 Performance of the SSA-based method

The same experimental results of the square shape parts are used to verify the SSA based method. The PDM of the N_{pl} deviation profiles is derived by calculating the mean profile and the deviation modes, or principle components. Among all the identified modes, the first $t = 4$ modes explain 98.944% of variance in the original data and therefore are kept for dimension reduction. The main mode scores $\boldsymbol{s}$ are calculated and provided to the GP model as response variables together with the corresponding parameters $(\boldsymbol{p}, h)$ as predictor variables. Independent GPs are trained to model each of the scores.

The trained GPs are further tested on deviations of test parts. Given the test parameters $\boldsymbol{p}^*$ as listed in Row *NO*.16 and *NO*.17 of Table 4.1, the scores $\boldsymbol{s}^*$ of test part layers are predicted by the GPs and the deviation profile of each layer can be reconstructed by Equation 4.13. The deviation values associated with the grid points of the deviation profile are consequently inversely mapped to the nominal layer geometry to obtain the actual out-of-plane deviation. The prediction results of both test parts regarding the 6 sampled layers are illustrated in Figure 4.18 and Figure 4.19. Since the magnitude of scores doesn't necessarily determine the magnitude of reconstructed deviations, the confidence interval of deviations is hard to obtain with the intervals of scores predicted by the GP model. Therefore, in both figures, only the mean prediction is provided.

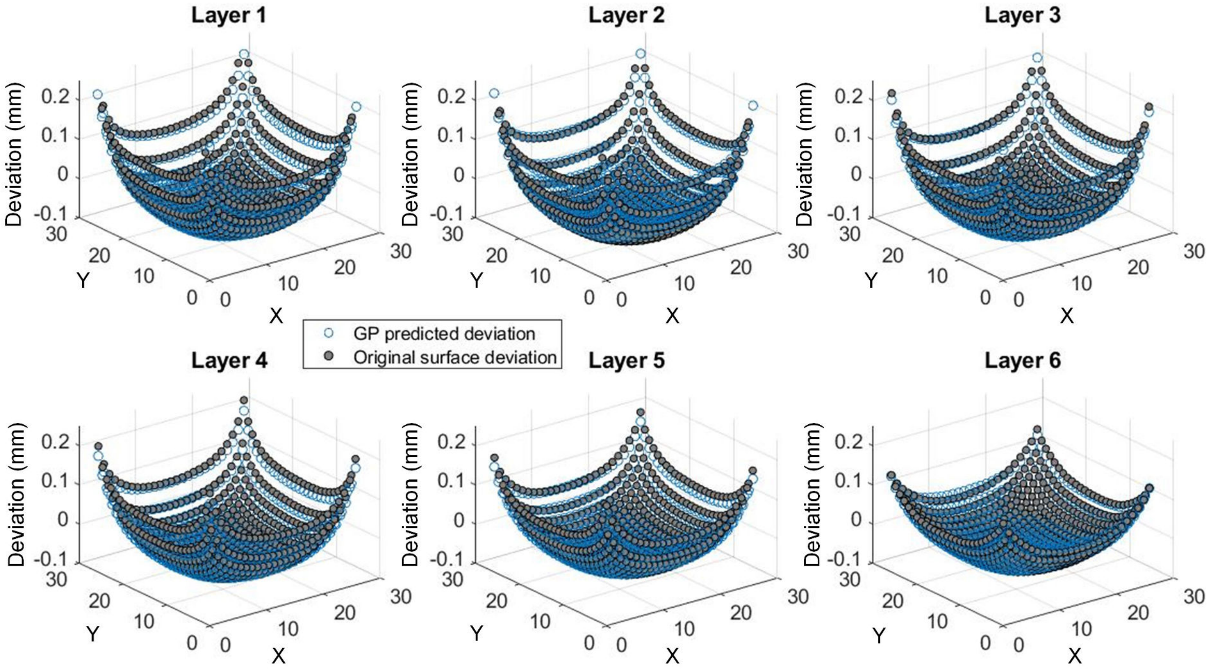

Figure 4.18: Predicted out-of-plane deviation compared with the actual deviation of Test Part *NO*.16

It can be seen from the figures that, the SSA-based method achieves an accurate

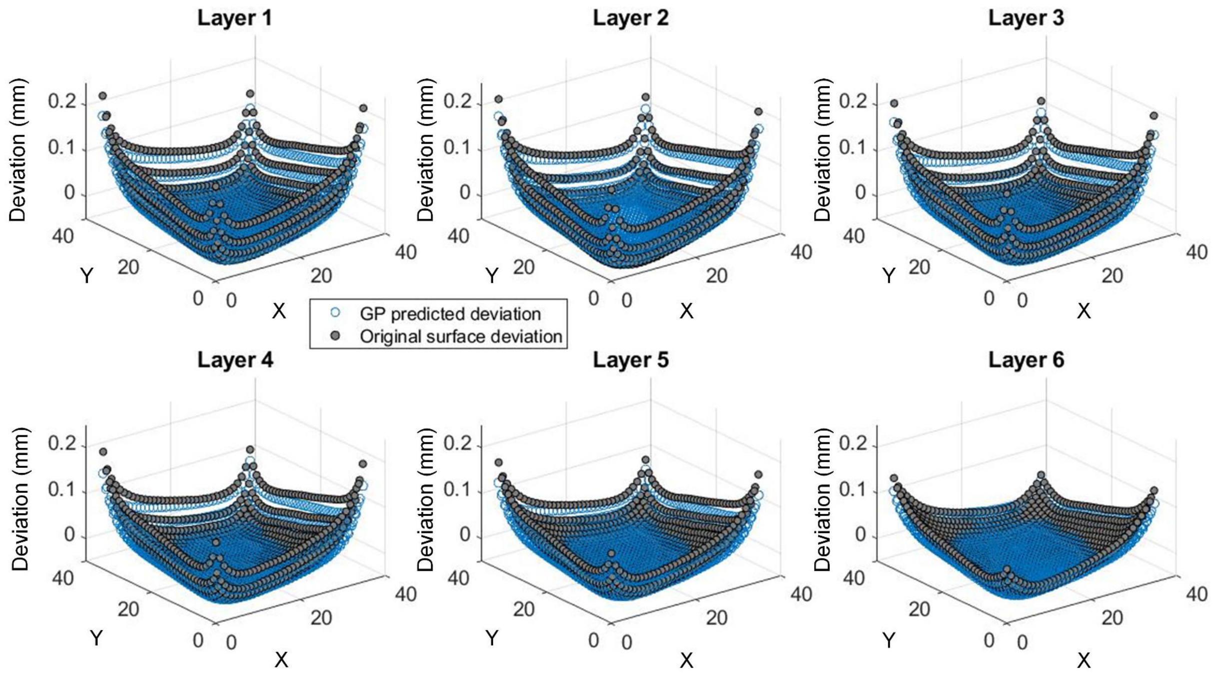

Figure 4.19: Predicted out-of-plane deviation compared with the actual deviation of Test Part *NO*.17

prediction of the deviations for both test parts. Figure 4.20 further provides a boxplot of the RMSEs of the prediction results on all parts. Compared with those predicted by the DCT-based method, current method reaches an overall improvement in the accuracy. The R-square computed on both the training and test parts maintains at a high level of over 98%, thus is not illustrated here.

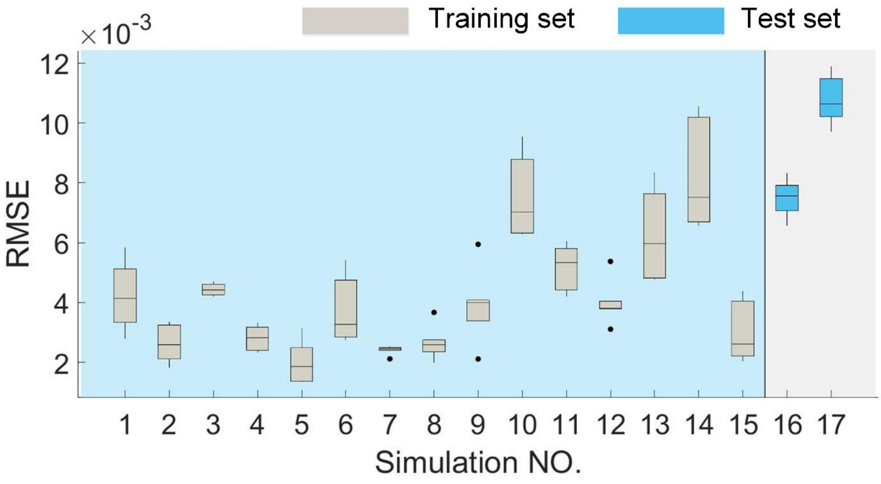

Figure 4.20: RMSE of predictions on layers of each part - SSA based method

4.5 Conclusion

In this chapter, a data-driven approach has been proposed aiming at the layer-level modeling of out-of-plane geometric deviations for AM parts. Based on deviation data obtained from FEA, modal analysis is conducted to identify the significant deviation modes in the layer data. Through statistical modeling of the mode indicators with respect to design and process characteristics, the approach enables accurate prediction of out-of-plane deviation on layers of AM parts fabricated under different process settings. Modal analysis is done using two approaches: DCT and SSA. From the case study, some general remarks can be made regarding the two approaches:

- For the same training shapes, the number of modes identified by SSA is much smaller than DCT. The modes identified by SSA contain more geometrical information about the original shape data, while the DCT is performed purely in the frequency domain. And the prediction results given by SSA illustrate a better accuracy than DCT.

- Both methods require a data alignment procedure, while since DCT should be strictly conducted on a rectangular grid structure, for non-rectangular shapes, the data needs to be interpolated or extrapolated to assign meaningful values to the grid points, which may sometimes bring in undesired modes. SSA allows for more flexibility in data alignment, as long as the correspondence between a common set of landmarks can be guaranteed. Therefore, SSA offers more convenience when it comes to complex free-form shapes. In this thesis, to unify the model description, the grid structure is used for both methods.

- The SSA-based method is highly dependent on the training shapes. In other words, it is hardly applicable to make prediction on shapes with a different form from the training shapes. In comparison, the modes identified by DCT are independent from the actual shapes and thus could be generalized to other shapes as well.

The incentive to use FEA is due to the difficulty in acquisition of internal layer deviation data from measurement, whereas, the credibility of the simulation results remains to be validated from real manufactured parts. The proposed method can also be generalized to measured deviations if such data are accessible with the help of more advanced measurement techniques, such as Computer Tomography (CT). Though the DCT-based method demonstrates a satisfactory performance on the square part, in order to maintain the performance for prediction of other shapes, the shape characteristics should be considered in the statistical model such that the deviation modes could be correlated to the actual shape. Therefore, parameterization of the shape-related properties is also worthwhile to be investigated. The shape descriptors can be used as a way to implement the parameterization. Based on a series of statistical models built for some basis shapes, the prediction of new shapes can be made by measuring their similarity to the basis shapes through the shape descriptors. Apart from modeling deviations for the generation of SMS, more applications of the proposed method can be envisioned. In quality control, given process settings, the prediction made by the method can be used to derive appropriate compensation plans on the CAD model prior to the manufacturing process, thus improving the geometrical accuracy of the final part. Moreover, with enriched process information, the method could assist in building the digital twin of AM products [SAMW17]. By providing information on the geometric deviations, high-fidelity virtual model can be built as a reference to the physical part and used in design and manufacturing for different purposes.

Some sections of this chapter include published works or works submitted for publication. The DCT-based method is submitted to *Journal of Mechanical Science and Engineering* as a paper entitled *Statistical Modal Analysis for Out-of-plane Deviation Prediction in Additive Manufacturing.* The SSA-based method has been presented in *29th CIRP Design Conference* as a paper entitled *Geometric deviation modeling with Statistical Shape Analysis in Design for Additive Manufacturing.*

Chapter

5

Implementation and case study

Contents

5.1 Introduction

In the previous chapters, deviation models have been discussed with respect to the single layers obtained after slicing the nominal STL file input to the AM process. The slicing procedure, however, has decomposed the overall product model and the topological information is totally lost. The Skin Model Shape, as its definition conveys, should be the non-ideal product model incorporating the geometric deviations, which means that the deviations should be mapped to the nominal geometry while maintaining its original topology. The topological information is conveyed in the STL as points and triangle facets that establish the connection between points. Both the in-plane and out-of-plane deviation models operate on points of separate layers and can be used to obtain deviated point coordinates $\boldsymbol{P}$. Therefore, reconstruction of the topology implies recreating the triangular connection $\boldsymbol{F}$ between these deviated points. Traditional techniques, Delaunay Triangulation for example, generally perform on the whole point set and may result in the inter-penetration between points of several different layers, thus reducing the geometric quality of the final model. In this chapter, an inter-layer triangulation solution will be presented which is able to generate a new surface model incorporating the deviation information by sequentially connecting the deviated layer boundary points. Based on case studies presented in previous chapters, an integrated process for building the SMS from the nominal STL model will be illustrated on a toolbox developed with MATLAB.

5.2 Construction of Skin Model Shapes based on layer-wise deviation models

The layer connection problem has been intensively discussed within the computer graphics community as the problem of 'surface reconstruction from planar cross sections' [Boi88] or 'triangulation of contour lines' [Kep75] and has been successfully implemented in medical image processing to reconstruct the 3D surface model from 2D cross-sectional images acquired from computed tomography (CT) and magnetic resonance imaging (MRI) [PK96]. Given a set of N_l planar contours represented as orderly connected points on the deviated layer geometry $\boldsymbol{P} = \{\boldsymbol{P}_i\}, i = 1, ..., N_l$, the objective is to reconstruct a triangulated surface $(\boldsymbol{P}, \boldsymbol{V})$ by triangulating each pair of adjacent contours. In order to illustrate how the triangulation is performed, we take two sets of counter-clockwise (CCW) ordered points from two adjacent contours for example as $\boldsymbol{P}^a = \{A_i\}, i = 1, ..., m$ and $\boldsymbol{P}^b = \{B_j\}, j = 1, ..., n$, as shown in Figure 5.1. The points need to be reasonably connected to form the edges of triangle facets, resulting in a total number of $n * m$ possible connections. Denote a binary matrix M with size $m \times n$ as a connection graph, then each element a_{ij} equals 1 if the i-th point A_i of contour $\boldsymbol{P}^a$ is connected to the j-th point B_j of contour $\boldsymbol{P}^b$, otherwise a_{ij} equals 0. Several constraints must be satisfied in order for a geometrically valid triangulation [Kep75]:

- Each triangle should contain two consecutive contour points either from contour $\boldsymbol{P}^a$ or contour $\boldsymbol{P}^b$. That is to say, if $a_{ij} = 1$, then either $a_{i+1,j} = 1$ or $a_{i,j+1} = 1$.
- Each point on one contour should be connected at least once with a point on the other contour, yielding the constraint: $\sum_{i=1}^{m} a_{ij} \geq 1$ and $\sum_{j=1}^{n} a_{ij} \geq 1$.
- Cross-over between two connected contour lines is not allowed. Therefore, if $a_{ij} = 1$ and $a_{i+1,j} = 1$, then it should be guaranteed that $a_{i,j+1} = 0$, likewise, $a_{i+1,j} = 0$ if both $a_{ij} = 1$ and $a_{i,j+1} = 1$ stand.

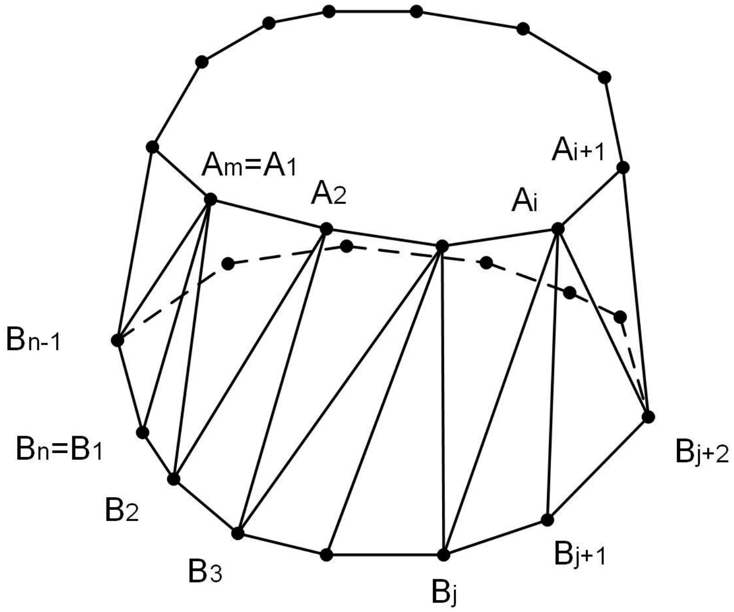

Figure 5.1: Triangulation of two parallel contours with ordered contour points

In this thesis, we introduce two different approaches to this triangulation problem: the span tour method and the graph-based method.

5.2.1 The span tour method

The two CCW-ordered contours can be expanded as two parallel lines as seen in Figure 5.2. Starting from an arbitrary point A_1 in $\boldsymbol{P}^a$, this method performs a tour on the upper and lower point pairs until reaching the rightmost of the lines, while conforming to the above-mentioned constraints [HK95]. This procedure can be explained as follows:

1. Contour $\boldsymbol{P}^a$ is translated in its 2D plane so that the line formed by its centroid and the centroid of $\boldsymbol{P}^b$ is perpendicular to the 2D plane of $\boldsymbol{P}^b$.

2. Starting from a point $A_i \in \boldsymbol{P^a}$, a span tour $\boldsymbol{S}_i$ is searched. Initially, a shortest span $S(i, j)$ is determined denoting the line that connects A_i with $B_j \in \boldsymbol{P^a}$ and has the shortest length among all n candidates, namely $\arg\min\limits_j |A_i B_j|$.

3. Once a current span is determined, the next span is chosen as either $S((i+1)\%m, j)$ or $S(i, (j+1)\%n)$. The feasibility of these spans should be checked in case of cross-over between previous spans, as illustrated in Figure 5.2. If both spans are feasible, the one with smaller length is selected.

4. The span tour terminates when the current span being evaluated is either $S((i-1)\%m, j)$ or $S(i, (j-1)\%n)$. The sum of all span lengths is then calculated as $L(\boldsymbol{S}_i)$.

5. Step 2 to Step 4 are repeated on all points $A_i, i = 1, ..., m$, resulting in m span tours. The optimal span tour is selected as the one with index $\hat{i} = \arg\min\limits_i L(\boldsymbol{S}_i)$. The corresponding spans in this span tour together with the edges of two contours form the reconstructed triangles.

The span tour method adopts a greedy solution when selecting the feasible spans and the complexity of this algorithm is $O(m(m+n))$.

5.2.2 Graph based method

The formulation of triangles actually corresponds to consecutively connecting two nearest 1-elements of M from a_{11} to a_{mn} while conforming to the constraints, and the best configuration needs to be selected from all possible candidates according to some given metrics. An intuitive solution was proposed in [SWPF15] by introducing a graph

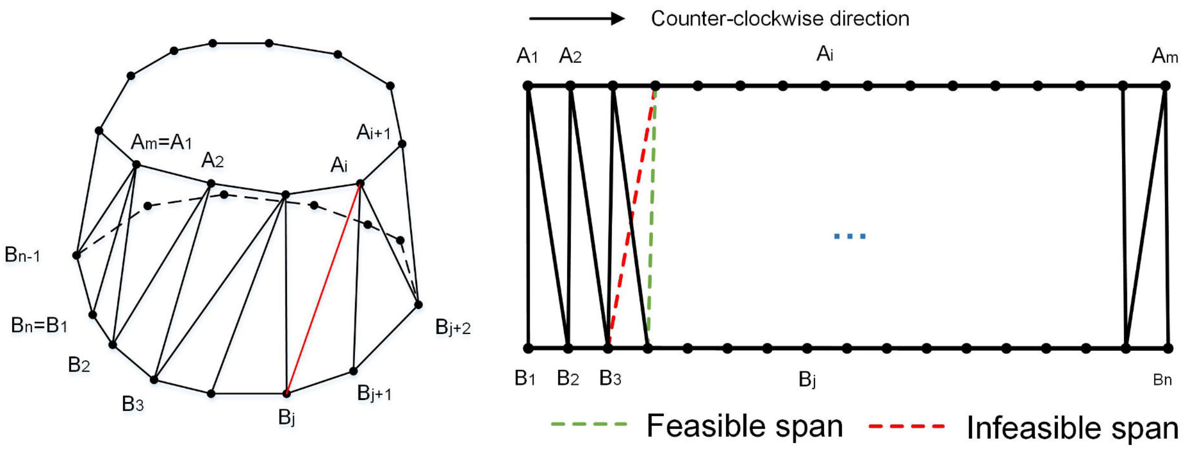

Figure 5.2: Span tour method

$G = \{N, E\}$, where a node N_{ij} of the graph denotes the element a_{ij} in M, and an arc E connecting two nodes (N_{ij}, N_{ik}) actually reflects the formulation of a triangle $A_iB_jB_k$. The triangulation problem now reduces to a path finding problem, in which a path traversing through G from N_{11} to N_{mn} while satisfying the constraints represents a possible configuration of triangulation. An optimal path is found by maximizing or minimizing given metrics specified on the nodes or edges of the graph. Common metrics are [MSS92]:

- *Volume metric* [Kep75]. The volume metric is to assign each arc $E_{ij} = (N_{ij}, N_{i+1,j})$ or $(N_{ij}, N_{i,j+1})$ a weight as the volume $v(i,j)$ of the tetrahedron $A_iA_{i+1}B_jO_b$ or $A_iB_jB_{j+1}O_a$, with i and j ranging from 1 to $m-1$ and $n-1$. O_a and O_b are origins of the $x-y$ coordinate system associated with the plane where contours P^a or P^b lies respectively. Among all the possible paths, one that maximizes the total volume is selected, which can be formulated as $\hat{\pi} = \arg\max\limits_{\pi} \sum_{E_{ij}\in\pi} v(i,j)$. Figure 5.3 provides an illustration of the volume metric. It is evident that the maximum volume criterion doesn't hold for concave shapes, therefore, some special care must be taken to the concave subsets of a shape by altering the max-operator to min-operator.

- *Area metric* [FKU77]. This metric is to assign each arc $E_{ij} = (N_{ij}, N_{i+1,j})$ or $(N_{ij}, N_{i,j+1})$ a weight as the area $s(i,j)$ of the corresponding triangle formed by $A_iA_{i+1}B_j$ or $A_iB_jB_{j+1}$. Among all the possible paths, one that minimizes the total triangle area is selected, which can be formulated as $\hat{\pi} = \arg\min\limits_{\pi} \sum_{E_{ij}\in\pi} s(i,j)$.

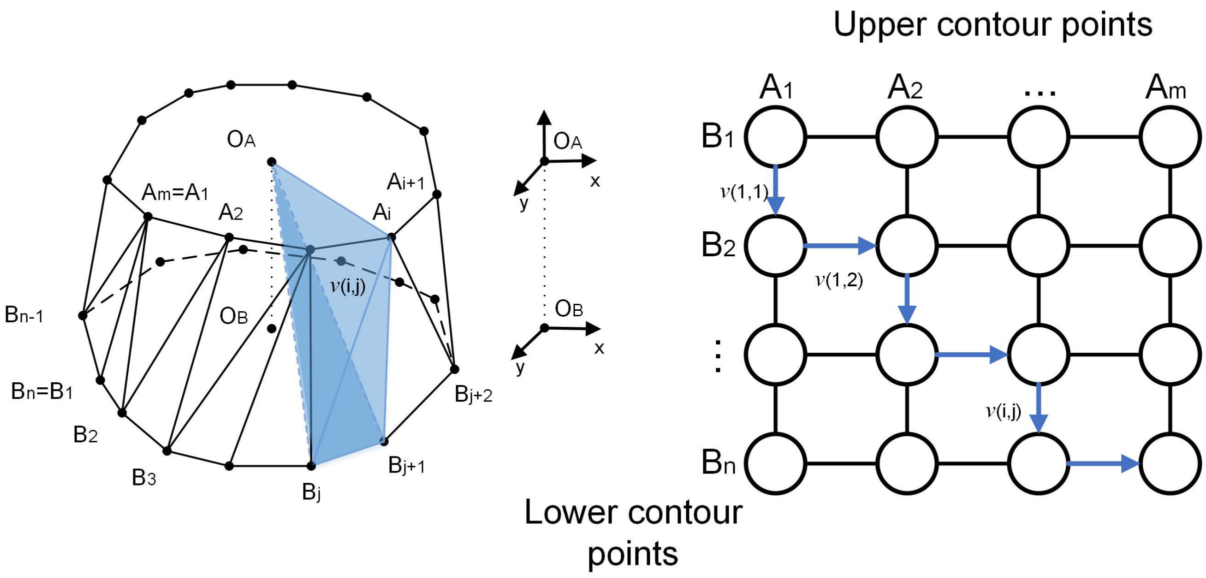

Figure 5.3: The volume metric

Figure 5.4 provides an illustration of the area metric.

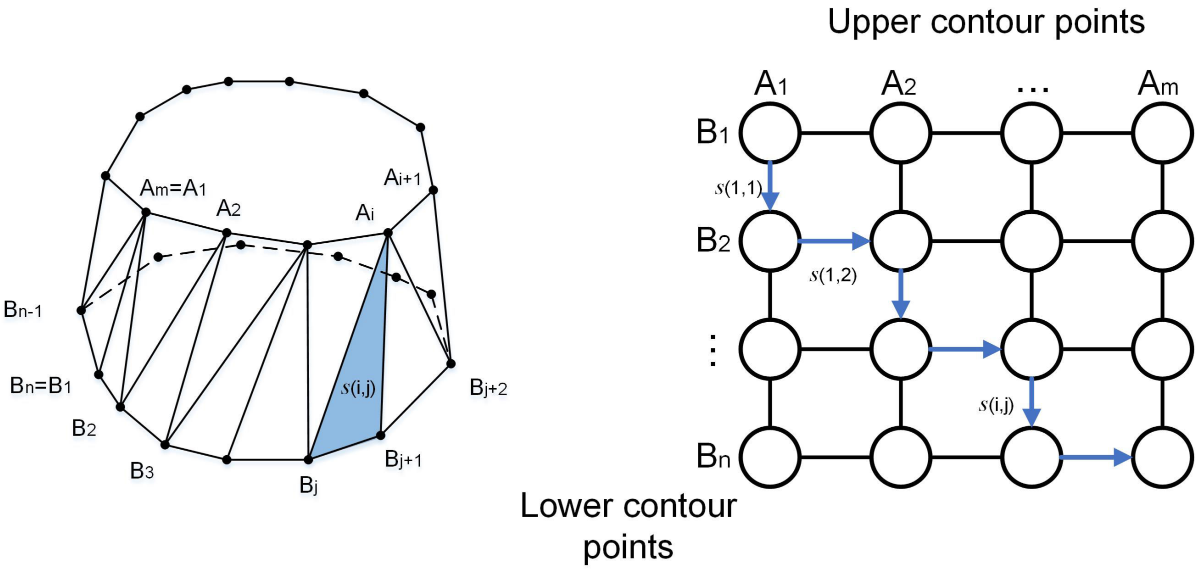

Figure 5.4: The area metric

- *Span length metric* [CS78, SWPF15]. The 'span' shares the same definition as that introduced in the span tour method, denoting a line connecting two points from each contour. This metric is to assign each node N_{ij} a weight as the corresponding span length $l(i,j) = |A_iB_j|$. Among all the possible paths, one that minimizes the total span length is selected, which can be formulated as $\hat{\pi} = \arg\min_{\pi} \sum_{N_{ij} \in \pi} l(i,j)$.

Figure 5.5 provides an illustration of the span length metric. This quite resembles the span tour method.

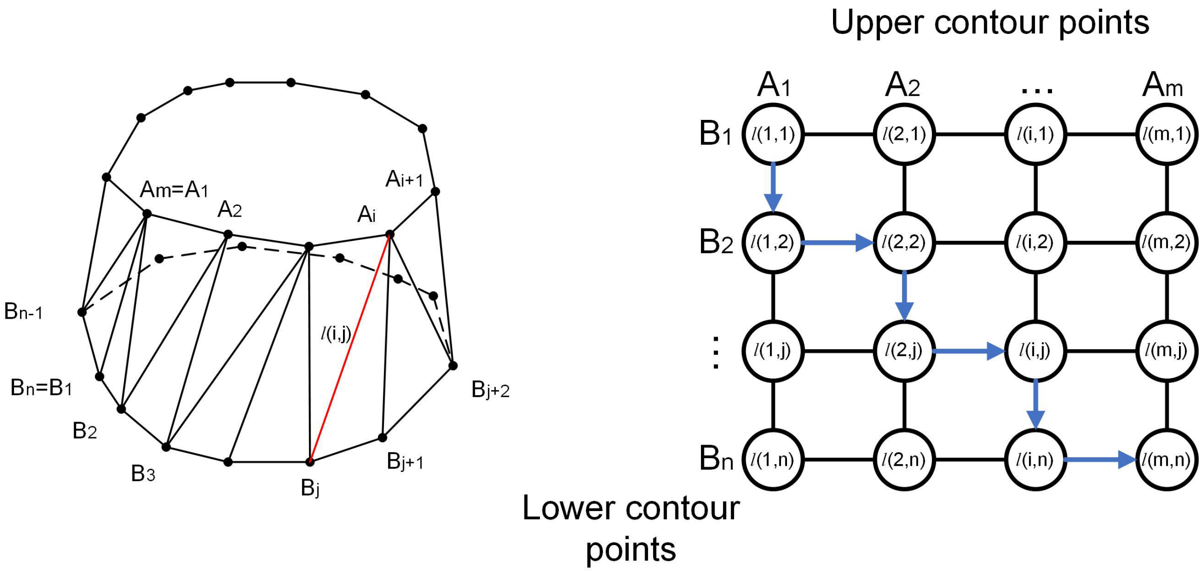

Figure 5.5: The span length metric

In this research, the span-length metric has been chosen due to its robustness in dealing with different special cases [MSS92]. With the defined metric and the corresponding weights calculated for all the nodes of the graph G, the optimal triangulation can be found by solving a minimum cost path problem using a dynamic programming method. Here we simply introduce how this method is implemented:

- Initialize an $m \times n$ zero matrix Q. Each element of this matrix will be consequently updated by measuring the cost accumulated while traveling from N_{11} to it.
- Set $Q_{11} = l(1,1)$, where $l(i,j)$ is the span length weight of node N_{ij}. Sequentially update the first row and first column of Q following

  $Q_{1i} = Q_{1,i-1} + l_{1,i}; i = 2, ..., m,$

  $Q_{j1} = Q_{j-1,1} + l_{j,1}; j = 2, ..., n.$
- Update the remaining elements row-by-row following

  $Q_{ij} = l_{i,j} + min(Q_{i-1,j}, Q_{i,j-1});\ i = 2, .., m; j = 2, .., n.$
- The final updated value of Q_{mn} should be the minimum cost of all paths, i.e. the minimum total arc length. Then trace back from Q_{mn} to Q_{11} to find the sequence of nodes that composes the path.

Algorithme 2 Minimum cost path finding for optimal triangulation of two contours

```
Inputs: Span length weight $\{l(i,j)\}$ on each node $N_{ij}$ of $G$
Outputs: List of node indices $L$ denoting the minimum cost path
Initialize $m \times n$ zero matrix $Q$, list $L$, stack $S$
for $i$ in 2 to $m$ do
    $Q[1][i] = Q[1][i-1] + l[1][i]$
end for
for $j$ in 2 to $n$ do
    $Q[j][1] = Q[j-1][1] + l[j][1]$
end for
for $i$ in 2 to $n$ do
    for $j$ in 2 to $m$ do
        $Q[i][j] = l[i][j] + \min(Q[i-1][j], Q[i][j-1])$
    end for
end for
$i \longleftarrow n$,$j \longleftarrow m$
while $i > 1$ or $j > 1$ do
    if $i > 1$ and $(Q[i][j]$ equals $Q[i-1][j] + l[i][j])$ then
        if $j$ equals $n$ then
            $S$.push($(i-1, 1)$)
        else
            $S$.push($(i-1, j)$)
        end if
        $i \longleftarrow i-1$
    else
        if $Q[i][j]$ equals $Q[i][j-1] + l[i][j]$ then
            if $i$ equals $m$ then
                $S$.push($(1, j-1)$)
            else
                $S$.push($(i, j-1)$)
            end if
            $j \longleftarrow j-1$
        end if
    end if
end while
while not $S$.isEmpty do
    $L$.append($S$.pop)
end while
```

The detailed explanation of the path finding algorithm is provided in Algorithm 2. The output list L contains a sequence of graph nodes, namely triangle edges, to be connected. With this guideline, a triangulation can be established to connect the two contours. The graph-based method adopts a dynamic programming strategy to reach a global search for the optimal solution. Compared to the span tour method, the span lengths are pre-calculated, so the searching process needn't be performed repeatedly for each point of the contour, thus reducing the complexity to $O(mn)$ and improving the computational efficiency. Therefore, the graph-based method will be applied for layer connection.

So far, the triangulation problem has been discussed regarding two single adjacent contours, while there exists some far more complex scenarios. For instance, a correspondence issue would arise when there are multiple contours in both layers and a branching problem needs to be tackled when one single contour needs to be connected with several contours from the other layer. Since these problems are not the focus of this research, their solutions will be omitted here. Iterating the layer connection algorithm on each pair of adjacent layers along the build direction, a geometrically valid triangular surface model is obtained incorporating the modeled geometric deviations. This model serves as an SMS of the nominal product model.

5.3 Development of an integrated deviation modeling system

With the layer connection method, now we could define the whole process for building SMSs from the STL. The triangular surface model in the STL is first sliced with a given layer thickness, resulting in a total number of N_l layers of contour points $\{\boldsymbol{P}_i\}, i = 1, \cdots, N_l$. The contour points are sequentially connected in CCW direction to form the nominal in-plane shape. By transforming the shape into the PCS, the in-plane deviation models can be used to obtain the deviated shape, which is subsequently transformed back to the CCS. Meanwhile, based on the layer height and specified design and process parameters, the deviation of the in-plane shape is derived from the out-of-plane deviation models. Likewise, a new shape is obtained which comprises both kinds of deviations. Finally, the graph-based layer connection method is used to perform triangulation on all pair of adjacent layer contours and the reconstructed surface model can be treated as the SMS. A platform has been developed on MATLAB with a user interface to facilitate the interactive illustrations of all methods mentioned in this thesis. The architecture of this toolbox can be found in Figure 5.6, which has been organized according to the workflow mentioned above. The functions of this toolbox will be explained with respect to different panels based on a square part designed with $23mm$ side length and $5mm$ height.

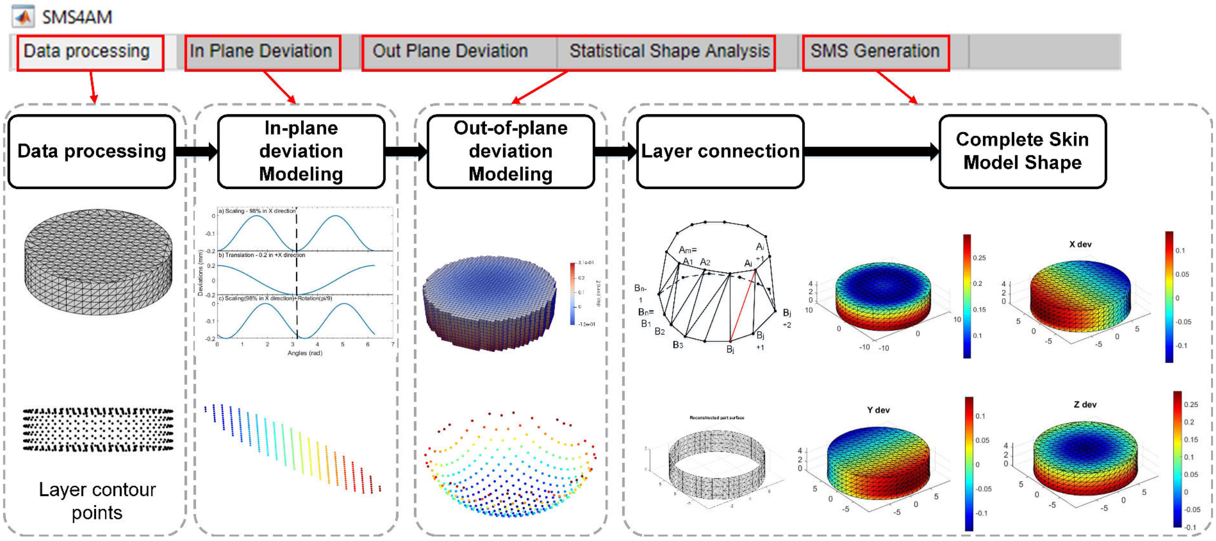

Figure 5.6: The architecture of the toolbox

5.3.1 The data processing panel

In the data processing panel, the part geometry is imported from the STL file and layer contours $\{\boldsymbol{P}_i\}, i = 1, \cdots, N_l$ are obtained by slicing the STL with user-defined layer thickness and error threshold. To avoid redundant density of the resulting SMS, a default thickness of $1mm$ is provided, thus $N_l = 6$. The layer contours are further transformed into the PCS as $\{r_i(\theta)\}$ for the subsequent in-plane deviation modeling procedure. The 2D shape of each layer in the PCS can be visualized in a plot widget by adjusting the slider to select the target layer to be plotted.

5.3.2 The in-plane deviation modeling panel

In the in-plane deviation modeling panel, both the Fourier Series expansion based method (FSE) and the transformation-based method are supported. As seen from Figure 5.8(a), the FSE method receives predefined Fourier Series (FS) coefficients $\{\boldsymbol{a}_i, \boldsymbol{b}_i\}, i = 1, \cdots, N_l$ as input, where $\boldsymbol{a}_i$, $\boldsymbol{b}_i$ are N-dimensional vectors and N denotes the order of expansion. To better illustrate the transformation effects on the in-plane deviation, five slider widgets are provided and users can conveniently adjust different combinations of scaling, rotation and translation parameters to observe the resulting deviation patterns in PCS, as shown in Figure 5.8(b). Alternatively, empirical parameter settings $\{\Psi_i\}, i = 1, \cdots, N_l$ could be imported from external files, where Ψ_i is the 5-element vector containing the parameter values. Either the FS coefficients or transformation

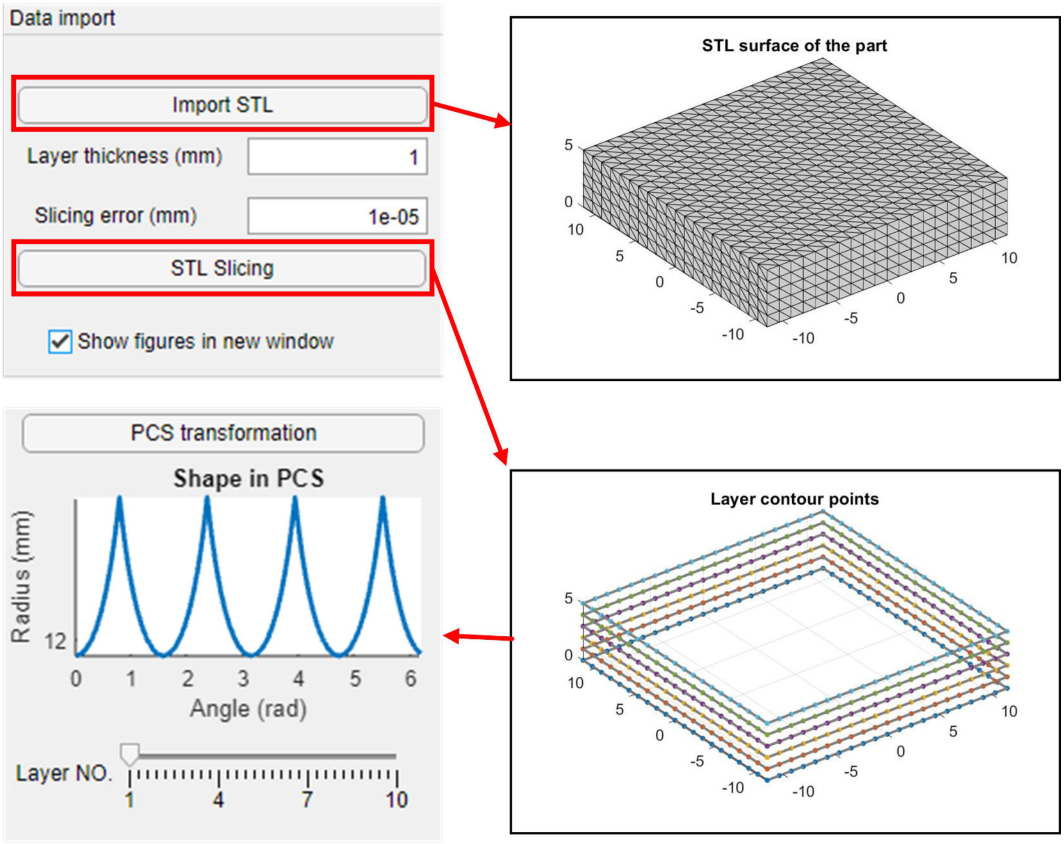

Layer thickness (mm) 1

Slicing error (mm) 1e-05

☑ Show figures in new window

Figure 5.7: The data processing panel

parameters are gathered from experience data and saved in a .mat file. The deviations of each layer are calculated as $\{\Delta r_i(\theta)\}$ and can be visualized on plot widgets by adjusting the target layer. The deviated in-plane shape is then derived in the PCS as $r_i'(\theta) = r_i(\theta) + \Delta r_i(\theta)$. By transforming the deviated shape back to the CCS and comparing with the nominal shape, the modeled in-plane deviations can be derived and intuitively visualized on the part surface regarding the overall magnitude as well as its projection in X and Y direction, as can be found in Figure 5.8.

5.3.3 The out-of-plane deviation panel

Following the discussion in Chapter 4, the out-of-plane deviation is modeled either on the whole external surface or in a layer-wise manner through statistical modal analysis. Free-form Deformation (FFD) and the random field method are used to respectively model systematic and random out-of-plane deviation on the part surface. The FFD operation starts with the bounding box calculation and subdivision of control points on the box. The number of control points can be flexibly adjusted by the user to reach

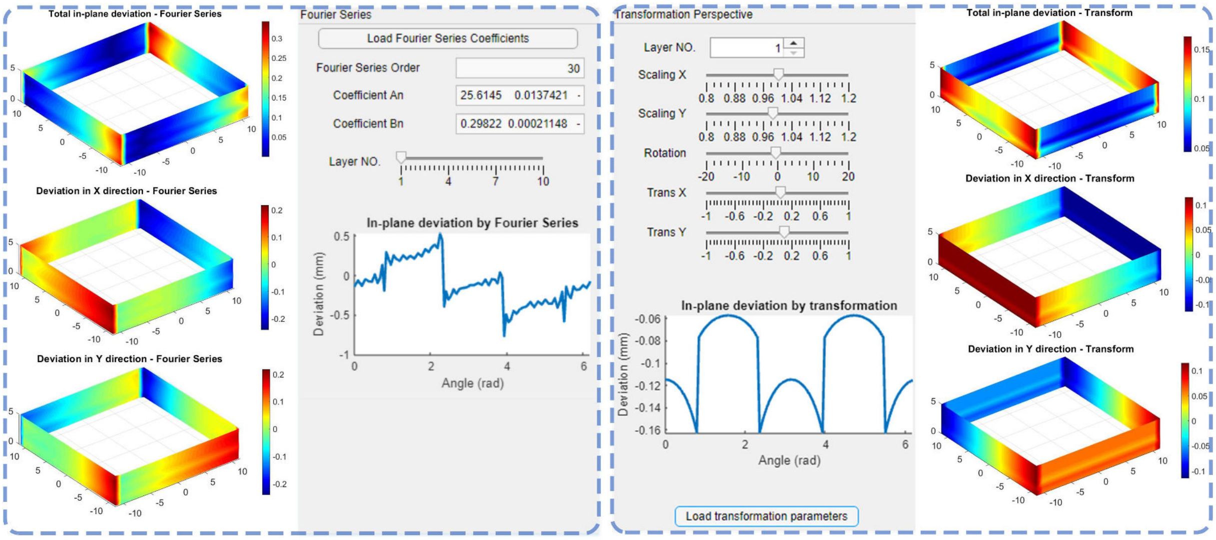

Fourier Series Order 30

Coefficient An 25.6145 0.0137421 -

Coefficient Bn 0.29822 0.00021148 -

Layer NO. 1

(a) The Fourier-Series based method (b) Transformation based method

Figure 5.8: The in-plane deviation modeling panel

different levels of control on the details. Deformations of these control points can be predefined according to out-of-plane deviation models and loaded to the toolbox, based on which FFD is performed to obtain the deviation on the whole part surface. In the next step, random deviations are generated based on random field parameters specified by the user. These sequential procedures are demonstrated in Figure 5.9 with numbers together with their results on the test square part. Finally, the deviations modeled respectively by FFD and random field are integrated to obtain a complete non-ideal part model with out-of-plane deviation.

Modal analysis is performed on observed deviation data gathered from AM simulation. The out-of-plane deviations, along with the associated voxel points, are stored in a .csv file in the simulation result and loaded to the toolbox, as seen in Figure 5.10(a). These data are further smoothed layer-by-layer to a regular grid whose range and interval are specified by the user. Thereafter, given the energy preservation ratio, DCT is performed on the deviation data of each layer, and the most significant DCT modes as well as the deviation reconstructed from them are visualized. As shown in Figure 5.10(b), the deviation of Layer 4 can be closely approximated with 6 DCT modes while preserving over 95% of information in the original data.

To enable effective deviation prediction based on experimental data, a design of experiments (DoE) is conducted to select a set of design and process parameters $\boldsymbol{p} \in$

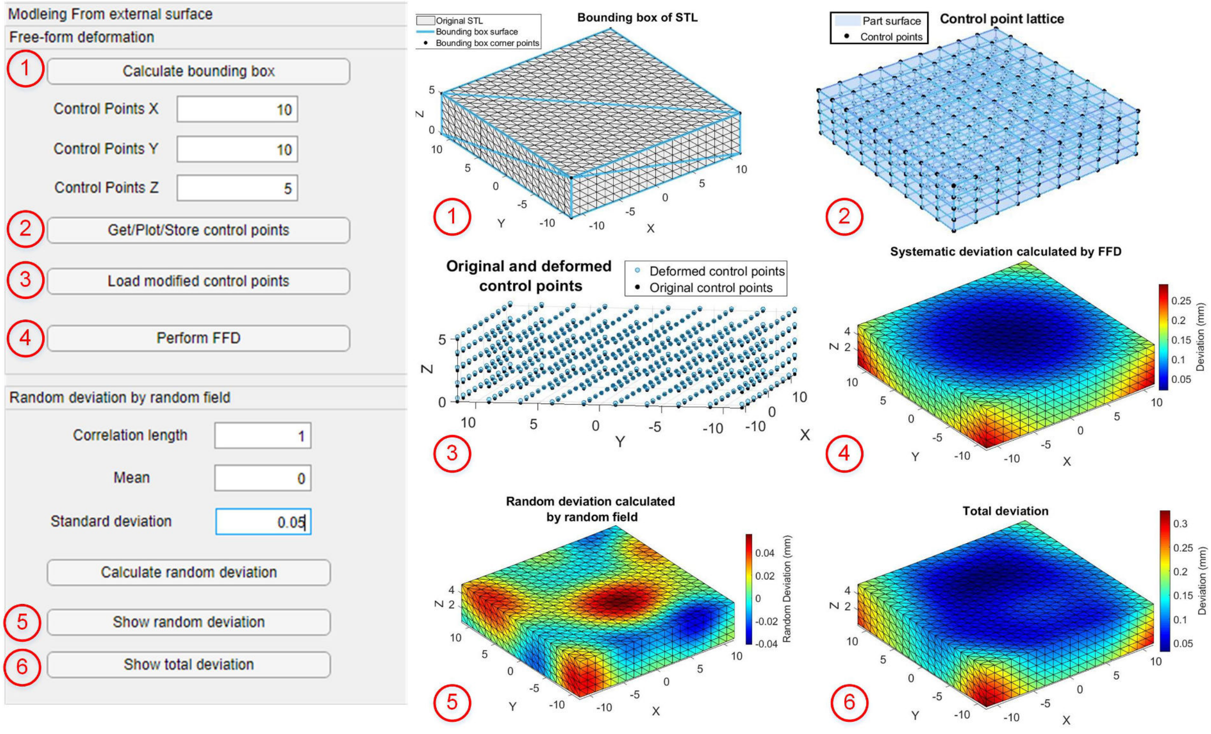

Modleing From external surface

Free-form deformation

Control Points X: 10

Control Points Y: 10

Control Points Z: 5

Random deviation by random field

Correlation length: 1

Mean: 0

Standard deviation: 0.05

Figure 5.9: The out-of-plane deviation modeling panel - external surface

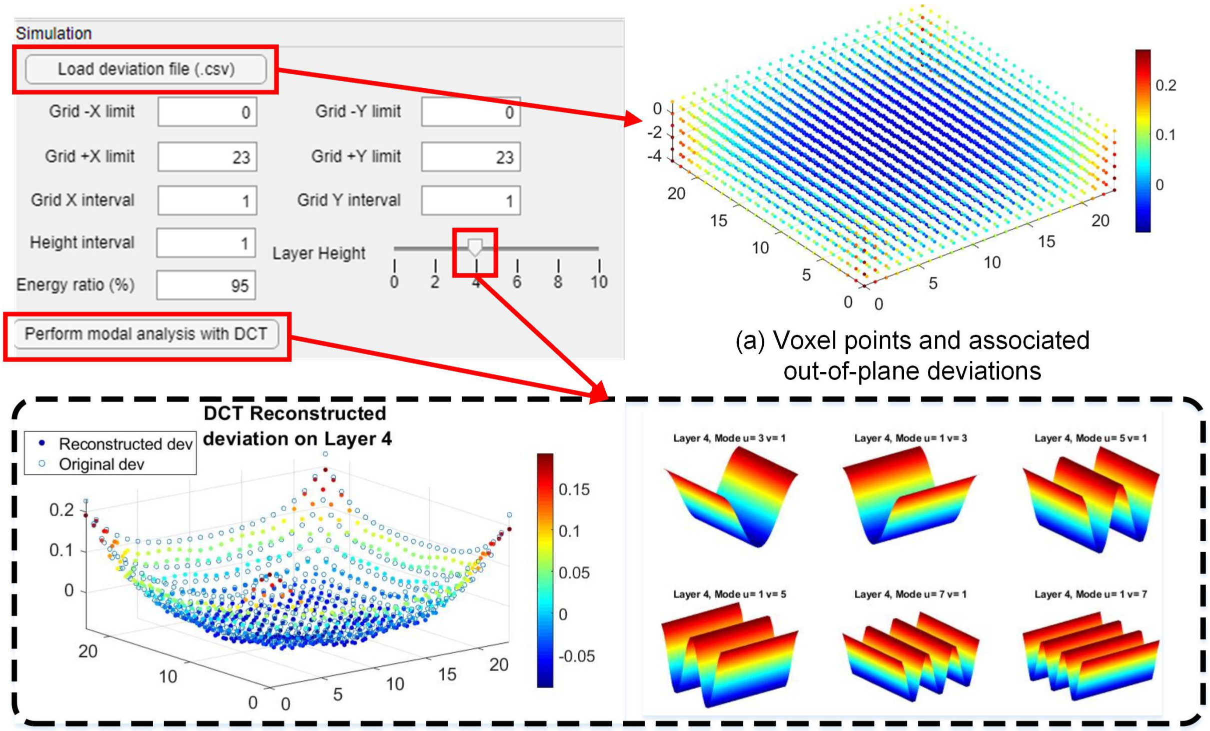

Simulation

Grid -X limit: 0

Grid -Y limit: 0

Grid +X limit: 23

Grid +Y limit: 23

Grid X interval: 1

Grid Y interval: 1

Height interval: 1

Energy ratio (%): 95

Layer Height: 4

(a) Voxel points and associated out-of-plane deviations

(b) Major deviation modes identified by DCT and deviation reconstructed by such modes

Figure 5.10: The out-of-plane deviation modeling panel - modal analysis with DCT

$R^{N_p \times 4}$, guided by which simulations are performed. The experimental design and the collected simulation data used in Section 4.4 are adopted here. A table widget is provided in the toolbox showing the designed parameter combinations. The deviation profile of a specific layer of the experimental parts can be visualized by selecting the corresponding row element of the target part and adjusting the layer height h through the slider widget, as shown in Figure 5.11.

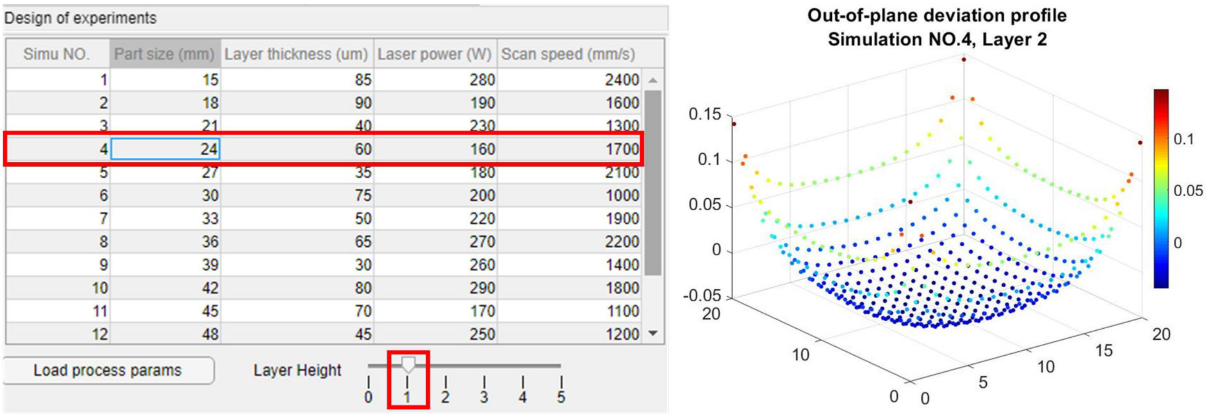
Design of experiments

Simu NO.	Part size (mm)	Layer thickness (um)	Laser power (W)	Scan speed (mm/s)
1	15	85	280	2400
2	18	90	190	1600
3	21	40	230	1300
4	24	60	160	1700
5	27	35	180	2100
6	30	75	200	1000
7	33	50	220	1900
8	36	65	270	2200
9	39	30	260	1400
10	42	80	290	1800
11	45	70	170	1100
12	48	45	250	1200

Figure 5.11: The out-of-plane deviation modeling panel - deviation profile of experimental parts

The $N_{pl} = N_p * N_l$ pieces of layer-wise deviation profiles are further processed with SSA to extract the most significant modes capable of explaining an adequate amount of information in the data. By specifying the number of principle components, SSA is performed and as a result, the mean deviation profile is plotted and the scores of profiles corresponding to each mode are displayed in a table. Each row of the table corresponds to the scores of one deviation profile. The deviation explained by mode j of profile i will be demonstrated when the (i, j)-th entry of the table is clicked, along with the deviation profile reconstructed by addition of the mean profile and the identified modes, as seen in Figure 5.12. Gaussian Process models are trained with the parameters as predictors and the mode scores as response. The trained models are then used to predict the out-of-plane deviation for new parts.

5.3.4 The Skin Model Shapes generation panel

The test part involved in this case study is simulated with new parameters specified in the table of Figure 5.13. Combining the trained Gaussian Process models with the result of SSA, the out-of-plane deviation of each layer of the test part are predicted. It can be

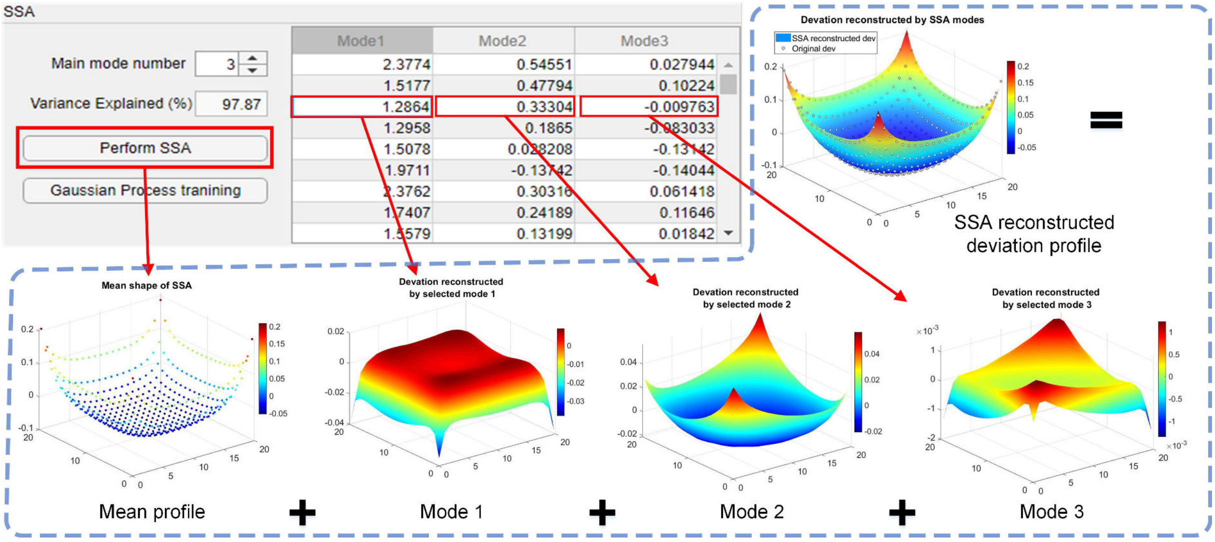

SSA

Main mode number: 3

Variance Explained (%): 97.87

Mode1	Mode2	Mode3
2.3774	0.54551	0.027944
1.5177	0.47794	0.10224
1.2864	0.33304	-0.009763
1.2958	0.1865	-0.083033
1.5078	0.028208	-0.13142
1.9711	-0.13742	-0.14044
2.3762	0.30316	0.061418
1.7407	0.24189	0.11646
1.5579	0.13199	0.01842

Figure 5.12: The out-of-plane deviation modeling panel - statistical shape analysis

found from Figure 5.13 that the prediction result reaches a high consistency with the observed deviation. The contours with in-plane deviations obtained in Section 5.3.2 are further deviated in the build directions based on these predicted out-of-plane deviations. Different from the in-plane deviation that is only modeled on the contour points, the out-of-plane deviation also has an effect on the internal points of the top and bottom surface, therefore, these points should also be considered. At the last step, the layer connection method introduced in Section 5.2 is adopted to triangulate the deviated layer geometries to eventually generate the comprehensive SMS of the test part. The overall deviation of the SMS surface along x, y and z direction is also demonstrated, as shown in Figure 5.13.

5.4 Conclusion

In this chapter, the approach to building the complete SMS for an AM part is explained. The span tour based and graph based methods are introduced which could connect the deviated contours to generate the non-ideal part surface. The final SMS incorporates both the in-plane and out-of-plane deviations, and the layer-per-layer modeling process conforms to the characteristic of AM. With all such theoretical foundations, a toolbox is developed which provides an interactive platform integrating the deviation modeling methods discussed in previous chapters to build the SMS step-wise. Different functions of the toolbox as well as the intermediate results produced by them are demonstrated on a test part.

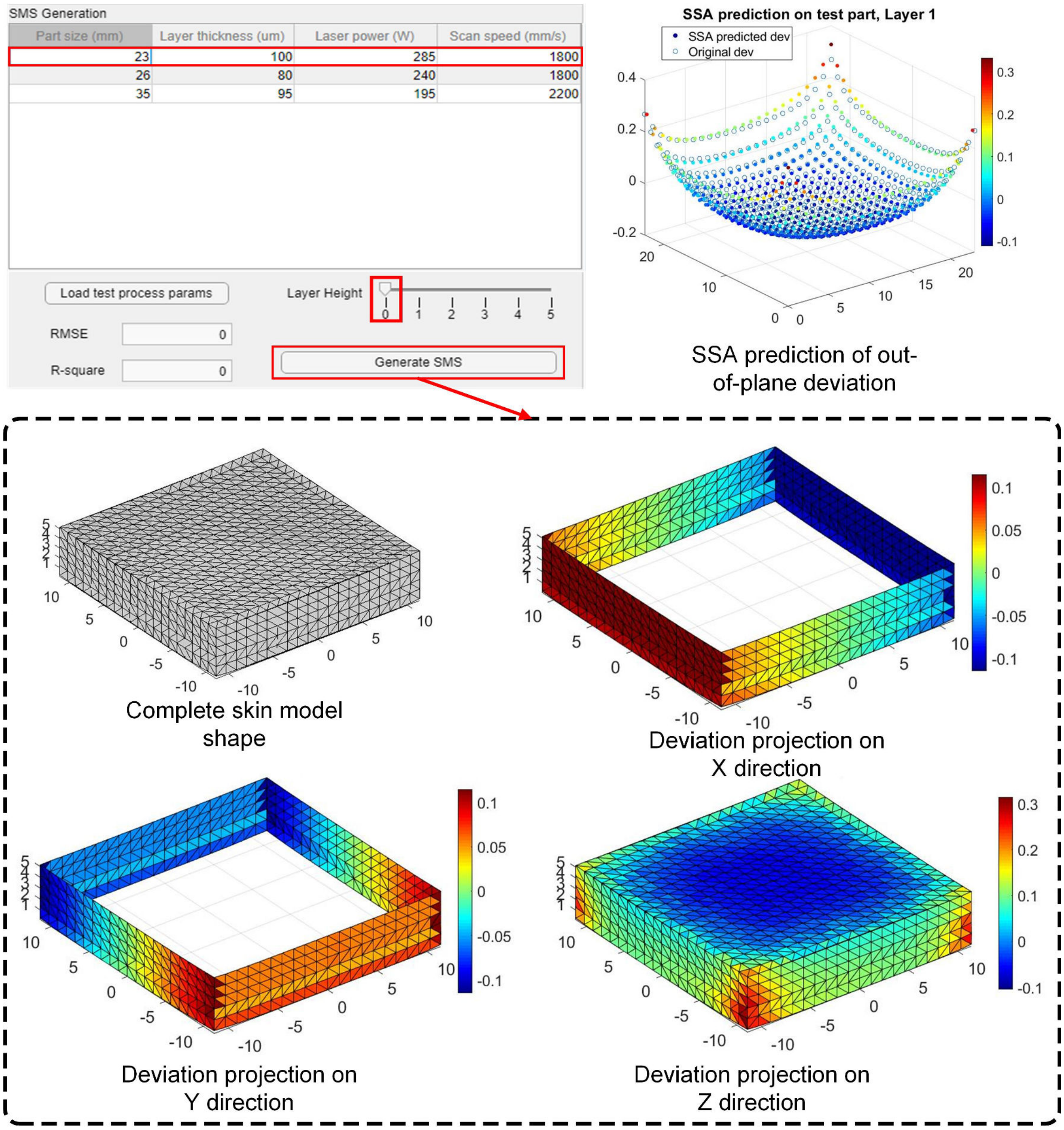

SMS Generation

Part size (mm)	Layer thickness (um)	Laser power (W)	Scan speed (mm/s)
23	100	285	1800
26	80	240	1800
35	95	195	2200

RMSE 0

R-square 0

SSA prediction of out-of-plane deviation

Complete skin model shape

Deviation projection on X direction

Deviation projection on Y direction

Deviation projection on Z direction

Figure 5.13: The Skin Model Shapes generation panel

Chapter 6
Conclusion

Contents

The geometrical inaccuracies of final products pose a critical demand for effective modeling of geometric deviations for AM processes. The complicated error sources in AM, however, are beyond the interpretability of traditional deviation modeling methods. The new layer-per-layer building mechanism also calls for a new perspective that could capture the intra-layer and inter-layer information about deviations. In view of the mature theoretical background and rich practical application of the SMS framework in geometric deviation modeling, new attempts are made in this thesis to develop a new SMS framework specifically for AM processes.

6.1 Contributions

To summarize, the major contributions of this work are listed as follows:

- A survey has been made regarding existing research on the deviation modeling for AM processes. The reviewed methods are divided into three categories according to their specific focus on: geometric approximation errors, machine errors and process parameters and material shrinkage. General remarks are made on these methods with respect to their strength, weakness and application scope. The mainstream AM simulation software packages are also introduced with a benchmark has been made summarizing their respective features, especially in the support for prediction of geometric deviations. This survey has covered a substantial range of research interests in AM deviation modeling and provides the basis for development of new methods for AM.

- The methodologies and applications of SMS are comprehensively reviewed. As the background information, the origin and concept of the SMS are introduced. The different mathematical models used for generating the SMS in both the prediction and observation stage are explained, some of which are inherited for AM deviation modeling. The engineering applications are also discussed, including tolerance modeling, assembly simulation and tolerance analysis. For each application, the problem formulation, technical details and the characteristics of solutions are elaborated. The new challenges when extending the current framework to AM are also depicted. This review presents an overview of the SMS framework and serves as a reference for the new AM deviation modeling framework. The consideration of systematic and random deviations, and the classification of prediction and observation stage, are inherently conveyed in the new framework.

- The transformation perspective achieves more efficient parameterization of in-plane deviation and is more consistent with the potential effects of AM process errors. The variational effects on the in-plane shape are mapped into affine shape transformations and the transformation parameters are estimated from observed deviation data using statistical methods. This parametric model manages to represent the in-plane deviation patterns with reduced complexity and enhanced generality among different shapes.

- The statistical modal analysis enables the layer-level investigation of out-of-plane deviation with a data-driven approach. The method enables the deviation prediction under different combinations of design and process parameters, enhancing the transferability among different process conditions. A novel strategy is also proposed to build SMS from the deviated geometry of each layer. The data-driven methods endows the new framework with improved expandability to conveniently adapt to new shapes and process conditions.

- A toolbox is developed on MATLAB with a graphical user interface to demonstrate the works developed in this thesis. The toolbox starts from reading the STL file of a part and conducts step-wise modeling of in-plane and out-of-plane deviations for each layer of the part. Users could flexibly specify the parameters to view the resulting deviations and generate the final SMS of the part. Beyond the demonstration purpose, this toolbox could be further upgraded with more interactivity to serve as a fully functional platform.

6.2 Future perspectives

The work discussed in this thesis are not sufficient yet, and some interesting research topics remain to be exploited on the basis of this thesis. In the following, some possible directions of the future work are envisioned.

- The statistical modal analysis method used for out-of-plane deviation modeling can also be applied for in-plane deviation modeling. In Chapter4, the out-of-plane deviation profiles serve as the input for modal analysis, so it is possible to obtain the in-plane deviation profiles for deviations in x and y directions as well. Likewise, the deviations are added to the planar grid structure in the z direction to form the profiles. Since the deviation patterns along the three directions are mutually different, both the DCT and SSA method, as well as the GP models, should be established independently. In this way, the modal analysis could be extended to tackle the complete deviation modeling task, and a unified processing work-flow can be achieved for both type of deviations.

- Current methods are validated mostly on simulation data, the model calibration on measurement data from manufactured samples remains to be accomplished. The use of simulation data brings multiple benefits, including time-saving data acquisition, simplified data processing and low noise in data. However, there are some phenomena in the real AM process that cannot be reflected from simulation, such as porosity, surface finish and defects caused by support removal. In order for a reliable model which could be used in industrial applications, such phenomena should also be accounted for. Nevertheless, despite the huge task for manufacturing and measurement of a moderate number of sample parts, how to obtain the deviation of the internal layer geometry is another unavoidable challenge which could be solved only if more advanced measurement device is available.

- The out-of-plane model could still be enriched with consideration of more factors in the AM process. Though current model covers several process parameters in the SLM process, it is anticipated that more parameters could be incorporated, such as hatch spacing, build orientation, scan pattern, powder bed temperature, material properties etc. However, simply adding these parameters into the statistical model may not make sense in explaining the physical effects of such factors. For example, a different build orientation results in changes of the shape of each layer, hence the deviation profiles are significantly inconsistent and cannot be analyzed with a common statistical shape model. This problem may also arise when the shape of different layers of a part are not uniform. In this case, it is important to develop new models to accommodate the characteristics of new factors.

- The shape-specific deviation model can be improved with enhanced transferability among shapes of different complexities using deep learning techniques. Ongoing work has been made to adopt a Convolutional Neural Network (CNN) to learn to predict geometric deviations given the input shape and process parameters. A typical CNN is composed of a number of hidden layers, including convolution layer, non-linearity layer, pooling layer and fully-connected layer, which are able to extract the features from input images and make predictions for either classification or regression tasks. The motivation to use CNN for our research is the expectation to capture the shape characteristics within deviation data taking advantage of the feature extraction capability of CNN. To this end, a CNN architecture has been designed as illustrated in Figure 6.1. The input to this network is a multi-dimensional matrix imitating a multi-channel image for traditional image classification tasks. The first dimension of the matrix is the geometry dimension which comprises the 2D shape information of a layer. Each of the other dimensions is filled with constants representing the design and process parameters. The output is a three-dimensional matrix containing the deviations of the input shape along x,y and z respectively. Therefore, this network is actually performing a element-wise regression task aiming at predicting the deviation at each location of the shape dimension given the assigned values in the parameter dimensions. If a sufficient number of training data from a large range of different shapes are available, the trained network would be able to identify the features of a new unseen shape and make the desired prediction of deviations. The results obtained from existing work have demonstrated satisfactory prediction performance of this network on simple cylindrical and rectangular shapes, and more efforts will be devoted to extending the variety of shapes. Moreover, the laser scan pattern could be formulated as another input dimension to help gain a better understanding of the distribution of deviations.

Apart from improvement of the deviation models, the future applications of SMS in AM processes could be envisioned as follows.

- The deviation modeling methods could assist Design for Additive Manufacturing (DfAM). Among the many investigated tasks of DfAM, the geometrical validation aiming to ensure the consistency between digital product and the final outcome, as well as design optimization intended to achieve optimal geometrical or topological design incorporating process knowledge, are closely concerned with geometric

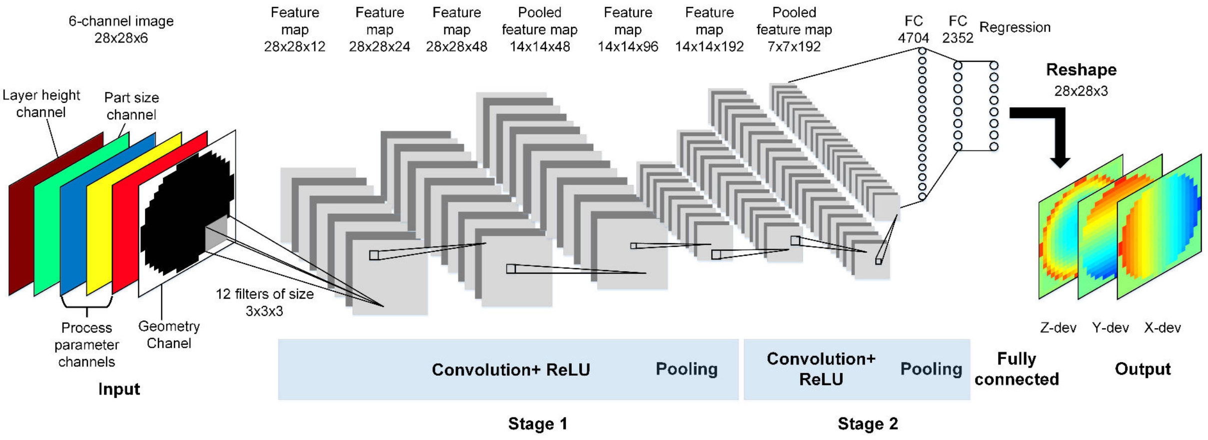

Figure 6.1: The CNN architecture for AM deviation modeling

deviations [LSAL15, LSALC14, TMV+16]. Through the deviation modeling methods discussed in this thesis, designers could have a predictive view of the probable geometrical defects on the manufactured product prior to mass production, and make correction and compensation on the original model to obtain optimized geometric consistency with the design intent. Therefore, more technical details can be explored based on this thesis to develop the methodologies well suited for DfAM.

- The generated SMSs could be used for multiple purposes in tolerancing. Though the deviations are modeled layer by layer, the final SMS is reconstructed as a non-ideal surface model and the tolerance modeling method introduced in Section 2.3.4 can be used to evaluate the deviations with respect to tolerance specifications. Likewise, the assembly simulation and tolerance analysis techniques regarding the non-ideal models of multiple parts can be adapted to AM.

- The generated SMSs can serve as reference models for developing the digital twin of AM products. The digital twin is recognized as 'a comprehensive physical and functional description of a product that includes its major information covering the life-cycle' [BR16]. The use of SMS in building the digital twin has been discussed in [SAMW17] regarding its concept, representation and implementation along the product life-cyle. The work in this thesis could be incorporated in the digital twin research as a branch to AM and will be further investigated towards industrial applications.

Acknowledgements

Firstly, I would like to express my deepest gratitude to my directors Prof.Nabil Anwer and Pro.Luc Mathieu for their patient guidance and academic support in my Ph.D study, for their kindness, motivation, and profound knowledge. Their guidance helped me in all the time of research and writing of this thesis.

Besides, I would like to express my thanks to the thesis committee members: Dr.Alex Ballu, Prof.Jean-Yves Dantan, Prof.Lihong Qiao, Prof.François Villeneuve, Prof.Giovanni Moroni and Prof.Olivier Bruneau, for their insightful suggestions and encouragement, and also for the questions raised by them which motivated me to broaden my research from various perspectives.

I thank my colleagues in LURPA for the meaningful discussions, for their help with my daily life, and for all the fun we have had in the last three years. Also I thank all my friends in Cachan, for the wonderful memories we have shared and the firm support in preparing the celebration party.

I would like also to thank my sponsors of the China Scholarship Council, Ms.Min Zhao and Mr.Jingsong Fan, without their help, I wouldn't have got the scholarship to follow my Ph.d study.

Last but not the least, I would like to thank my dear friend, Dr.Lloyd Williams, my girlfriend, Mengqi Xie, and my parents for supporting me spiritually throughout writing this thesis and my life in general.

Bibliography

[17411] ISO 17450-1:2011. Geometrical product specifications (gps) – general concepts – part 1: Model for geometrical specification and verification. 2011.

[22411] ISO 22432:2011. Geometrical product specifications (gps) – features utilized in specification and verification. 2011.

[3DS18] 3DS. Simulia abaqus. `https://www.3ds.com/products-services/simulia/`, December 2018. Online; accessed 2018-12-20.

[ABC18] Antonio Armillotta, Mattia Bellotti, and Marco Cavallaro. Warpage of FDM parts: Experimental tests and analytic model. *Robotics and Computer-Integrated Manufacturing*, 50(August 2017):140–152, 2018.

[ABM13] Nabil Anwer, Alex Ballu, and Luc Mathieu. The skin model, a comprehensive geometric model for engineering design. *CIRP Annals - Manufacturing Technology*, 62(1):143–146, 2013.

[ANR74] Nasir Ahmed, T Natarajan, and Kamisetty R Rao. Discrete cosine transform. *IEEE transactions on Computers*, 100(1):90–93, 1974.

[ANS18] ANSYS. Ansys additive print. `https://www.ansys.com/products/structures/ansys-additive-print`, December 2018. Online; accessed 2018-12-20.

[ASG$^+$07] Gaurav Ameta, S. Serge, M. Giordano, Jami J. Shah, Gaurav Ameta, Zhengshu Shen, and Joseph Davidson. Navigating the Tolerance Analysis Maze. *Computer-Aided Design and Applications*, 4(5):705–718, 2007.

[ASMW14] Nabil Anwer, Benjamin Schleich, Luc Mathieu, and Sandro Wartzack. From solid modelling to skin model shapes: Shifting paradigms in computer-aided tolerancing. *CIRP Annals - Manufacturing Technology*, 63(1):137–140, 2014.

[AST13] ASTM International. F2792-12a - Standard Terminology for Additive Manufacturing Technologies. *Rapid Manufacturing Association*, pages 10–12, 2013.

[Aut18] Autodesk. Netfabb. `https://www.autodesk.com/products/netfabb/overview`, December 2018. Online; accessed 2018-12-20.

[AWML15] Gaurav Ameta, Paul Witherell, Shawn Moylan, and Robert Lipman. Tolerance specification and related issues for additively manufactured products. In *ASME 2015 International Design Engineering Technical Conferences and Computers and Information in Engineering Conference*, pages V01AT02A027–V01AT02A027. American Society of Mechanical Engineers, 2015.

[BCLO95] Gabriel Bugeda, Miguel Cervera, Guillermo Lombera, and Eugenio Oñate. Numerical analysis of stereolithography processes using the finite element method. *Rapid Prototyping Journal*, 1(2):13–23, 1995.

[BCW08] Edwin Bonilla, Kian Ming Chai, and Christopher Williams. Multi-task Gaussian Process Prediction. *Nips*, 20(October):153–160, 2008.

[BM96] Alex Ballu and Luc Mathieu. Univocal expression of functional and geometrical tolerances for design, manufacturing and inspection. In *Computer-aided Tolerancing*, pages 31–46. Springer, 1996.

[Boi88] Jean-Daniel Boissonnat. Shape reconstruction from planar cross sections. *Computer vision, graphics, and image processing*, 44(1):1–29, 1988.

[BR16] Stefan Boschert and Roland Rosen. Digital twin—the simulation aspect. In *Mechatronic Futures*, pages 59–74. Springer, 2016.

[BS18] Matteo Bugatti and Quirico Semeraro. Limitations of the inherent strain method in simulating powder bed fusion processes. *Additive Manufacturing*, 23:329–346, 2018.

[CET01] Timothy F Cootes, Gareth J Edwards, and Christopher J Taylor. Active appearance models. *IEEE Transactions on Pattern Analysis & Machine Intelligence*, (6):681–685, 2001.

[Com18] MSC Software Company. Simufact. https://www.simufact.com/, December 2018. Online; accessed 2018-12-20.

[CS78] Henry N Christiansen and Thomas W Sederberg. Conversion of complex contour line definitions into polygonal element mosaics. In *ACM Siggraph Computer Graphics*, volume 12, pages 187–192. ACM, 1978.

[CTCG95] Timothy F Cootes, Christopher J Taylor, David H Cooper, and Jim Graham. Active shape models-their training and application. *Computer vision and image understanding*, 61(1):38–59, 1995.

[CTW17] Longwei Cheng, Fugee Tsung, and Andi Wang. A Statistical Transfer Learning Perspective for Modeling Shape Deviations in Additive Manufacturing. *IEEE Robotics and Automation Letters*, 2(4):1988–1993, 2017.

[CWT18] Longwei Cheng, Andi Wang, and Fugee Tsung. A prediction and compensation scheme for in-plane shape deviation of additive manufacturing with information on process parameters. *IISE Transactions*, 50(5):394–406, 2018.

[DBM08] Jean Yves Dantan, Alex Ballu, and Luc Mathieu. Geometrical product specifications - model for product life cycle. *CAD Computer Aided Design*, 40(4):493–501, 2008.

[DHG$^+$17] Jean Yves Dantan, Zhicheng Huang, Edoh Goka, Lazhar Homri, Alain Etienne, Nicolas Bonnet, and Mickael Rivette. Geometrical variations management for additive manufactured product. *CIRP Annals - Manufacturing Technology*, 66(1):161–164, 2017.

[DIM14] Erik R Denlinger, Jeff Irwin, and Pan Michaleris. Thermomechanical modeling of additive manufacturing large parts. *Journal of Manufacturing Science and Engineering*, 136(6):061007, 2014.

[DTA$^+$03] Rhodri H Davies, Carole J Twining, P Daniel Allen, Tim F Cootes, and Christopher J Taylor. Shape discrimination in the hippocampus using an mdl model. In *Biennial International Conference on Information Processing in Medical Imaging*, pages 38–50. Springer, 2003.

[FKU77] Henry Fuchs, Zvi M Kedem, and Samuel P Uselton. Optimal surface reconstruction from planar contours. *Communications of the ACM*, 20(10):693–702, 1977.

[Geo18] GeoNX. Virfac. http://www.geonx.com/, December 2018. Online; accessed 2018-12-20.

[GW15] P. L. Green and K. Worden. Bayesian and markov chain monte carlo methods for identifying nonlinear systems in the presence of uncertainty. *Philosophical Transactions of the Royal Society A: Mathematical, Physical and Engineering Sciences*, 373(2051):20140405, August 2015.

[Has70] Wilfred Keith Hastings. Monte carlo sampling methods using markov chains and their applications. *Biometrika*, 57(1):97–109, 1970.

[HC02] Wenzhen Huang and Dariusz Ceglarek. Mode-based decomposition of part form error by discrete-cosine-transform with implementation to assembly and stamping system with compliant parts. *CIRP Annals-Manufacturing Technology*, 51(1):21–26, 2002.

[HGLD17] Lazhar Homri, Edoh Goka, Guillaume Levasseur, and Jean Yves Dantan. Tolerance analysis — Form defects modeling and simulation by modal decomposition and optimization. *CAD Computer Aided Design*, 91:46–59, 2017.

[HK95] Park Hyungjun and Kim Kwangsoo. 3-d shape reconstruction from 2-d cross-sections. *Journal of Design and Manufacturing*, 5:171–185, 1995.

[HLC$^+$14] Wenzhen Huang, Jinya Liu, Vijya Chalivendra, Darek Ceglarek, Zhenyu Kong, and Yingqing Zhou. Statistical modal analysis for variation characterization and application in manufacturing quality control. *IIE Transactions (Institute of Industrial Engineers)*, 46(5):497–511, 2014.

[HNX$^+$14a] Qiang Huang, Hadis Nouri, Kai Xu, Yong Chen, Sobambo Sosina, and Tirthankar Dasgupta. Predictive modeling of geometric deviations of 3D printed products-A unified modeling approach for cylindrical and polygon shapes. *IEEE International Conference on Automation Science and Engineering*, 2014-Janua:25–30, 2014.

[HNX$^+$14b] Qiang Huang, Hadis Nouri, Kai Xu, Yong Chen, Sobambo Sosina, and Tirthankar Dasgupta. Statistical Predictive Modeling and Compensation of Geometric Deviations of Three-Dimensional Printed Products. *Journal of Manufacturing Science and Engineering*, 136(6):061008, 2014.

[HTB15] Lazhar Homri, Denis Teissandier, and Alex Ballu. Tolerance analysis by polytopes: Taking into account degrees of freedom with cap half-spaces. *Computer-Aided Design*, 62:112–130, 2015.

[Hua16] Qiang Huang. An Analytical Foundation for Optimal Compensation of Three-Dimensional Shape Deformation in Additive Manufacturing. *Journal of Manufacturing Science and Engineering*, 138(6):061010, 2016.

[HZSD15a] Qiang Huang, Jizhe Zhang, Arman Sabbaghi, and Tirthankar Dasgupta. Optimal offline compensation of shape shrinkage for three-dimensional printing processes. *IIE Transactions*, 47(5):431–441, 2015.

[HZSD15b] Qiang Huang, Jizhe Zhang, Arman Sabbaghi, and Tirthankar Dasgupta. Optimal offline compensation of shape shrinkage for three-dimensional printing processes. *IIE Transactions (Institute of Industrial Engineers)*, 47(5):431–441, 2015.

[ISO16] ISO/ASTM52915-16. Standard specification for additive manufacturing file format (amf) version 1.2. *ASTM International*, 2016.

[JJH16] Yuan Jin, S. Joe Qin, and Qiang Huang. Offline Predictive Control of Out-of-Plane Shape Deformation for Additive Manufacturing. *Journal of Manufacturing Science and Engineering*, 138(12):121005, 2016.

[JQH15] Yuan Jin, S Joe Qin, and Qiang Huang. Out-of-plane geometric error prediction for additive manufacturing. In *Automation Science and Engineering (CASE), 2015 IEEE International Conference on*, pages 918–923. IEEE, 2015.

[JQH16] Yuan Jin, S Joe Qin, and Qiang Huang. Prescriptive analytics for understanding of out-of-plane deformation in additive manufacturing. In *Automation Science and Engineering (CASE), 2016 IEEE International Conference on*, pages 786–791. IEEE, 2016.

[Kam16] Chandrika Kamath. Data mining and statistical inference in selective laser melting. *International Journal of Advanced Manufacturing Technology*, 86(5-8):1659–1677, 2016.

[Kep75] Eric Keppel. Approximating complex surfaces by triangulation of contour lines. *IBM Journal of research and development*, 19(1):2–11, 1975.

[KNXP13] Nils Keller, Fabian Neugebauer, H Xu, and Vasily Ploshikhin. Thermo-mechanical simulation of additive layer manufacturing of titanium aerospace structures. In *LightMAT Conference*, volume 3, 2013.

[LB17] Amirali Lalehpour and Ahmad Barari. Developing skin model in coordinate metrology using a finite element method. *Measurement: Journal of the International Measurement Confederation*, 109:149–159, 2017.

[LFC$^+$18] Chen Luo, Pasquale Franciosa, Darek Ceglarek, Zhonghua Ni, and Fang Jia. A Novel Geometric Tolerance Modeling Inspired by Parametric Space Envelope. *IEEE Transactions on Automation Science and Engineering*, 15(3):1386–1398, 2018.

[LFGF16] C. Li, C.H. Fu, Y.B. Guo, and F.Z. Fang. A multiscale modeling approach for fast prediction of part distortion in selective laser melting. *Journal of Materials Processing Technology*, 229:703–712, March 2016.

[LGCH19] He Luan, Marco Grasso, Bianca M Colosimo, and Qiang Huang. Prescriptive data-analytical modeling of laser powder bed fusion processes for accuracy improvement. *Journal of Manufacturing Science and Engineering*, 141(1):011008, 2019.

[LH15] He Luan and Qiang Huang. Predictive modeling of in-plane geometric deviation for 3d printed freeform products. In *2015 IEEE International Conference on Automation Science and Engineering (CASE)*, pages 912–917. IEEE, 2015.

[LH17] He Luan and Qiang Huang. Prescriptive modeling and compensation of in-plane shape deformation for 3-D printed freeform products. *IEEE Transactions on Automation Science and Engineering*, 14(1):73–82, 2017.

[LJY18] Jingran Li, Ran Jin, and Hang Z. Yu. Integration of physically-based and data-driven approaches for thermal field prediction in additive manufacturing. *Materials and Design*, 139:473–485, 2018.

[LLG17] Chao Li, Jingfu Liu, and YueBin Guo. Efficient predictive model of part distortion and residual stress in selective laser melting. *Additive Manufacturing*, 17:157–168, 2017.

[LLH10] Jonathan Lecompte, Olivier Legoff, and Jean Yves Hascoet. Technological form defects identification using discrete cosine transform method. *International Journal of Advanced Manufacturing Technology*, 51(9-12):1033–1044, 2010.

[LPA+19] Ting Liu, Laurent Pierre, Nabil Anwer, Yanlong Cao, and Jiangxin Yang. Form defects consideration in polytope-based tolerance analysis. *Journal of Mechanical Design*, 141(6):061702, January 2019.

[LSAL15] Floriane Laverne, Frédéric Segonds, Nabil Anwer, and Marc Le Coq. Assembly Based Methods to Support Product Innovation in Design for Additive Manufacturing: An Exploratory Case Study. *Journal of Mechanical Design*, 137(12):121701, 2015.

[LSALC14] Floriane Laverne, Frédéric Segonds, Nabil Anwer, and Marc Le Coq. Dfam in the design process: A proposal of classification to foster early design stages. *CONFERE, Sibenik, Croatia*, 2014.

[LZDS18] Jianhua Liu, Zhiqiang Zhang, Xiaoyu Ding, and Nan Shao. Integrating form errors and local surface deformations into tolerance analysis based on skin model shapes and a boundary element method. *Computer-Aided Design*, 104:45–59, 2018.

[Mal89] Jean-Laurent Mallet. Discrete smooth interpolation. *ACM Transactions on Graphics (TOG)*, 8(2):121–144, 1989.

[Mal92] Jean-Laurent Mallet. Discrete smooth interpolation in geometric modelling. *Computer-Aided Design*, 24(4):178–191, April 1992.

[Mal97] Jean-Laurent Mallet. Discrete modeling for natural objects. *Mathematical geology*, 29(2):199–219, 1997.

[MCHR10] Timothy I Matuszyk, Michael J Cardew-Hall, and Bernard F Rolfe. The kernel density estimate/point distribution model (kde-pdm) for statistical shape modeling of automotive stampings and assemblies. *Robotics and Computer-Integrated Manufacturing*, 26(4):370–380, 2010.

[MMP$^+$14] Richard Martukanitz, Pan Michaleris, Todd Palmer, Tarasankar DebRoy, Zi-Kui Liu, Richard Otis, Tae Wook Heo, and Long-Qing Chen. Toward an integrated computational system for describing the additive manufacturing process for metallic materials. *Additive Manufacturing*, 1:52–63, 2014.

[MPP17] Giovanni Moroni, Stefano Petrò, and Wilma Polini. Geometrical product specification and verification in additive manufacturing. *CIRP Annals - Manufacturing Technology*, 66(1):0–3, 2017.

[MSS92] David Meyers, Shelley Skinner, and Kenneth Sloan. Surfaces from contours. *ACM Transactions On Graphics (TOG)*, 11(3):228–258, 1992.

[MZD17] Tuhin Mukherjee, W Zhang, and Tarasankar DebRoy. An improved prediction of residual stresses and distortion in additive manufacturing. *Computational Materials Science*, 126:360–372, 2017.

[NPA13] Gaurav Navangul, Ratnadeep Paul, and Sam Anand. Error Minimization in Layered Manufacturing Parts by Stereolithography File Modification Using a Vertex Translation Algorithm. *Journal of Manufacturing Science and Engineering*, 135(3):031006, 2013.

[NWF05] Yiyi Ning, Y. S. Wong, and Jerry Ying Hsi Fuh. Effect and control of hatch length on material properties in the direct metal laser sintering process. *Proceedings of the Institution of Mechanical Engineers, Part B: Journal of Engineering Manufacture*, 219(1):15–25, 2005.

[NWFL06] Yiyi Ning, Y. S. Wong, Jerry Ying Hsi Fuh, and Han Tong Loh. An approach to minimize build errors in direct metal laser sintering. *IEEE Transactions on Automation Science and Engineering*, 3(1):73–80, 2006.

[PA15] Ratnadeep Paul and Sam Anand. A new Steiner patch based file format for Additive Manufacturing processes. *CAD Computer Aided Design*, 63:86–100, 2015.

[PF77] Eric Persoon and King-Sun Fu. Shape discrimination using fourier descriptors. *IEEE Transactions on systems, man, and cybernetics*, 7(3):170–179, 1977.

[PK96] Hyungjun Park and Kwangsoo Kim. Smooth surface approximation to serial cross-sections. *CAD Computer Aided Design*, 28(12):995–1005, 1996.

[PPA14] Neeraj Panhalkar, Ratnadeep Paul, and Sam Anand. Increasing Part Accuracy in Additive Manufacturing Processes Using a k-d Tree Based Clustered Adaptive Layering. *Journal of Manufacturing Science and Engineering*, 136(6):061017, 2014.

[Ras06] Carl Edward Rasmussen. Gaussian processes for machine learning. *International journal of neural systems*, 14(2):69–106, 2006.

[Reh10] Olaf Rehme. *Cellular design for laser freeform fabrication.* Cuvillier Göttingen, 2010.

[RP07] N Raghunath and Pulak Mohan Pandey. Improving accuracy through shrinkage modelling by using taguchi method in selective laser sintering. *International journal of machine tools and manufacture*, 47(6):985–995, 2007.

[SAMW14] Benjamin Schleich, Nabil Anwer, Luc Mathieu, and Sandro Wartzack. Skin model shapes: A new paradigm shift for geometric variations modelling in mechanical engineering. *Computer-Aided Design*, 50:1–15, 2014.

[SAMW15] Benjamin Schleich, Nabil Anwer, Luc Mathieu, and Sandro Wartzack. Contact and Mobility Simulation for Mechanical Assemblies Based on Skin Model Shapes. *Journal of Computing and Information Science in Engineering*, 15(2):021003, 2015.

[SAMW17] Benjamin Schleich, Nabil Anwer, Luc Mathieu, and Sandro Wartzack. Shaping the digital twin for design and production engineering. *CIRP Annals - Manufacturing Technology*, 66(1):141–144, 2017.

[SAZ+14] Benjamin Schleich, Nabil Anwer, Z Zhu, Lihong Qiao, Luc Mathieu, and Sandro Wartzack. Comparative study on tolerance analysis approaches. In *International Symposium on Robust Design (ISoRD'14)*, 2014.

[SBJ+16] Christoph Schmutzler, Fabian Bayerlein, Stephan Janson, Christian Seidel, and Michael F Zaeh. Pre-compensation of warpage for additive manufacturing. In *Fraunhofer Direct Digital Manufacturing Conference (DDMC), Berlin*, 2016.

[SDH+14] Arman Sabbaghi, Tirthankar Dasgupta, Qiang Huang, Jizhe Zhang, et al. Inference for deformation and interference in 3d printing. *The Annals of Applied Statistics*, 8(3):1395–1415, 2014.

[SG02] Mikkel B Stegmann and David Delgado Gomez. A brief introduction to statistical shape analysis. *Informatics and mathematical modelling, Technical University of Denmark, DTU*, 15(11), 2002.

[Sha14] Kunal Sharma. *Slice Contour Modification in Additive Manufacturing for Minimizing Part Errors*. PhD thesis, University of Cincinnati, 2014.

[SP86] Thomas W Sederberg and Scott R Parry. Free-form deformation of solid geometric models. *ACM SIGGRAPH computer graphics*, 20(4):151–160, 1986.

[SPA15] Nandkumar Siraskar, Ratnadeep Paul, and Sam Anand. Adaptive Slicing in Additive Manufacturing Process Using a Modified Boundary Octree Data Structure. *Journal of Manufacturing Science and Engineering*, 137(1):011007, 2015.

[SPR08] K Senthilkumaran, Pulak Mohan Pandey, and PV Madhusudan Rao. Shrinkage compensation along single direction dexel space for improving accuracy in selective laser sintering. In *2008 IEEE International Conference on Automation Science and Engineering*, pages 827–832. IEEE, 2008.

[SPR09a] K. Senthilkumaran, Pulak M. Pandey, and P. V M Rao. New model for shrinkage compensation in selective laser sintering. *Virtual and Physical Prototyping*, 4(2):49–62, 2009.

[SPR09b] K. Senthilkumaran, Pulak M. Pandey, and P. V.M. Rao. Influence of building strategies on the accuracy of parts in selective laser sintering. *Materials and Design*, 30(8):2946–2954, 2009.

[SPR12] K Senthilkumaran, PM Pandey, and PVM Rao. Statistical modeling and minimization of form error in sls prototyping. *Rapid Prototyping Journal*, 18(1):38–48, 2012.

[SRW+16] Chenhui Shao, Jie Ren, Hui Wang, Jionghua (Judy) Jin, and S. Jack Hu. Improving Machined Surface Shape Prediction by Integrating Multi-Task Learning With Cutting Force Variation Modeling. *Journal of Manufacturing Science and Engineering*, 139(1):011014, 2016.

[SW15a] Benjamin Schleich and Sandro Wartzack. Approaches for the assembly simulation of skin model shapes. *Computer-Aided Design*, 65:18–33, 2015.

[SW15b] Benjamin Schleich and Sandro Wartzack. Evaluation of geometric tolerances and generation of variational part representatives for tolerance analysis. *International Journal of Advanced Manufacturing Technology*, 79(5-8):959–983, 2015.

[SW18] Benjamin Schleich and Sandro Wartzack. Novel approaches for the assembly simulation of rigid Skin Model Shapes in tolerance analysis. *CAD Computer Aided Design*, 101:1–11, 2018.

[SWHT14] Suoyuan Song, Andi Wang, Qiang Huang, and Fugee Tsung. Shape deviation modeling for fused deposition modeling processes. In *Automation Science and Engineering (CASE), 2014 IEEE International Conference on*, pages 758–763. IEEE, 2014.

[SWPF15] Kyle Sunderland, Boyeong Woo, Csaba Pinter, and Gabor Fichtinger. Reconstruction of surfaces from planar contours through contour interpolation. In *Medical Imaging 2015: Image-Guided Procedures, Robotic Interventions, and Modeling*, volume 9415, page 94151R. International Society for Optics and Photonics, 2015.

[SWW+12] Benjamin Schleich, Michael Walter, Sandro Wartzack, Nabil Anwer, and Luc Mathieu. A comprehensive framework for skin model simulation. In

ASME 2012 11th Biennial Conference on Engineering Systems Design and Analysis, pages 567–576. American Society of Mechanical Engineers, 2012.

[SZZ16] Christoph Schmutzler, Alexander Zimmermann, and Michael F. Zaeh. Compensating Warpage of 3D Printed Parts Using Free-form Deformation. *Procedia CIRP*, 41:1017–1022, 2016.

[TALJ03] Kun Tong, E Amine Lehtihet, and Sanjay Joshi. Parametric error modeling and software error compensation for rapid prototyping. *Rapid Prototyping Journal*, 9(5):301–313, 2003.

[Tib96] Robert Tibshirani. Regression shrinkage and selection via the lasso. *Journal of the Royal Statistical Society. Series B (Methodological)*, pages 267–288, 1996.

[TJL08] Kun Tong, Sanjay Joshi, and E. Amine Lehtihet. Error compensation for fused deposition modeling (FDM) machine by correcting slice files. *Rapid Prototyping Journal*, 14(1):4–14, 2008.

[TLJ04] Kun Tong, E Amine Lehtihet, and Sanjay Joshi. Software compensation of rapid prototyping machines. *Precision Engineering*, 28(3):280–292, 2004.

[TMV$^+$16] Mary Kathryn Thompson, Giovanni Moroni, Tom Vaneker, Georges Fadel, R Ian Campbell, Ian Gibson, Alain Bernard, Joachim Schulz, Patricia Graf, Bhrigu Ahuja, et al. Design for additive manufacturing: Trends, opportunities, considerations, and constraints. *CIRP annals*, 65(2):737–760, 2016.

[WLLS14] Ola Wagersten, Björn Lindau, Lars Lindkvist, and Rikard Söderberg. Using Morphing Techniques in Early Variation Analysis. *Journal of Computing and Information Science in Engineering*, 14(1):011007, 2014.

[Wor18] Additive Works. Amphyon. `https://additive.works/`, December 2018. Online; accessed 2018-12-20.

[WQZA19] Jianshun Wu, Lihong Qiao, Zuowei Zhu, and Nabil Anwer. A novel representation method of non-ideal surface morphologies and its application in shaft-hole sealing simulation analysis. *Proceedings of the Institution of Mechanical*

Engineers, Part B: Journal of Engineering Manufacture, 233(2):575–587, 2019.

[WXJ07] Tian Ming Wang, Jun Tong Xi, and Ye Jin. A model research for prototype warp deformation in the FDM process. *International Journal of Advanced Manufacturing Technology*, 33(11-12):1087–1096, 2007.

[XHSD13] Lijuan Xu, Qiang Huang, Arman Sabbaghi, and Tirthankar Dasgupta. Shape deviation modeling for dimensional quality control in additive manufacturing. In *ASME 2013 International Mechanical Engineering Congress and Exposition*, pages V02AT02A018–V02AT02A018. American Society of Mechanical Engineers, 2013.

[YB18a] Xingyu Yan and Alex Ballu. Review and Comparison of Form Error Simulation Methods for Computer Aided Tolerancing. *Journal of Computing and Information Science in Engineering*, 19(March):1–16, 2018.

[YB18b] Xingyu Yan and Alex Ballu. Tolerance analysis using skin model shapes and linear complementarity conditions. *Journal of Manufacturing Systems*, 48(July):140–156, 2018.

[ZA15] Wentao Zha and Sam Anand. Geometric approaches to input file modification for part quality improvement in additive manufacturing. *Journal of Manufacturing Processes*, 20:465–477, 2015.

[ZAHM18] Zuowei Zhu, Nabil Anwer, Qiang Huang, and Luc Mathieu. Machine learning in tolerancing for additive manufacturing. *CIRP Annals*, 67(1):157–160, 2018.

[ZAM17] Zuowei Zhu, Nabil Anwer, and Luc Mathieu. Deviation Modeling and Shape Transformation in Design for Additive Manufacturing. In *Procedia CIRP*, volume 60, pages 211–216, 2017.

[ZAM18] Zuowei Zhu, Nabil Anwer, and Luc Mathieu. Shape Transformation Perspective for Geometric Deviation Modeling in Additive Manufacturing. *Procedia CIRP*, 75:75–80, 2018.

[ZAMZ11] Min Zhang, Nabil Anwer, Luc Mathieu, and Haibin Zhao. A discrete geometry framework for geometrical product specifications. In *Proceedings of the 21st CIRP Design Conference, Kaist, MK Thompson, ed., Paper*, number 20, 2011.

[ZAS+13] Min Zhang, Nabil Anwer, Andreas Stockinger, Luc Mathieu, and Sandro Wartzack. Discrete shape modeling for skin model representation. *Proceedings of the Institution of Mechanical Engineers, Part B: Journal of Engineering Manufacture*, 227(5):672–680, 2013.

[ZC06] Y Zhang and YK Chou. Three-dimensional finite element analysis simulations of the fused deposition modelling process. *Proceedings of the Institution of Mechanical Engineers, Part B: Journal of Engineering Manufacture*, 220(10):1663–1671, 2006.

[ZC08] Y Zhang and K Chou. A parametric study of part distortions in fused deposition modelling using three-dimensional finite element analysis. *Proceedings of the Institution of Mechanical Engineers, Part B: Journal of Engineering Manufacture*, 222(8):959–968, 2008.

[ZKA+17] ZHU Zuowei, Safa Keimasi, Nabil Anwer, Luc Mathieu, and QIAO Lihong. Review of shape deviation modeling for additive manufacturing. In *Advances on Mechanics, Design Engineering and Manufacturing*, pages 241–250. Springer, 2017.

[ZL+02] Dengsheng Zhang, Guojun Lu, et al. A comparative study of fourier descriptors for shape representation and retrieval. In *Proc. 5th Asian Conference on Computer Vision*, page 35. Citeseer, 2002.

[ZL04] Dengsheng Zhang and Guojun Lu. Review of shape representation and description techniques. *Pattern Recognition*, 37(1):1–19, 2004.

[ZLDS18] Zhiqiang Zhang, Jianhua Liu, Xiaoyu Ding, and Nan Shao. Tolerance analysis of annular surfaces considering form errors and local surface deformations. *Procedia CIRP*, 75:291–296, 2018.

[ZQA16] Zuowei Zhu, Lihong Qiao, and Nabil Anwer. An improved tolerance analysis method based on skin model shapes of planar parts. *Procedia Cirp*, 56:237–242, 2016.

[ZR72] Charles T Zahn and Ralph Z Roskies. Fourier descriptors for plane closed curves. *IEEE Transactions on computers*, 100(3):269–281, 1972.

Appendix A

Derivation of the transformation-based in-plane deviation function

In the appendix, a complementary discussion is be made on the derivation of in-plane deviation functions based on the transformation-based method introduced in Section 3.3. Two regular shapes, namely the bi-circular shape and the elliptical shape, are used as examples. The mathematical forms of these shapes and the deviations resulting from the scaling transformation effects are presented, together with illustrations of the deviation patterns under specific settings of the scaling parameters.

A.1 Transformation of circular shapes

The representation of a circular shape with radius r is given by $r^{\circ}(\theta) = r, \theta \in [0, 2\pi]$ in PCS and $(x^{\circ})^2 + (y^{\circ})^2 = r^2$ in CCS. Assuming that the manufactured shape shares the same PCS origin with the nominal one, then combining the two representations and Equation 3.16, we get the analytical form of $r^*(\theta; \Psi, r^{\circ}(\theta))$ from A.1 and therefore $f(\theta; \Psi)$.

$$
\begin{aligned}
(h_1(x^*, y^*, \Psi))^2 + (h_2(x^*, y^*, \Psi))^2 &= (r^{\circ}(\theta))^2 \\
x^* = r^* cos(\theta), y^* &= r^* sin(\theta) \\
h_1(x^*, y^*, \Psi) &= [(x^* - \Delta y)cos(\alpha) - (y^* - \Delta x)sin(\alpha)]/\varphi_y \\
h_2(x^*, y^*, \Psi) &= [(x^* - \Delta y)sin(\alpha) - (y^* - \Delta x)cos(\alpha)]/\varphi_x
\end{aligned}
\tag{A.1}
$$

The derived $f(\theta; \Psi)$ is quite lengthy, so its complete form will not be presented here. By varying the transformation parameter values input to $f(\theta; \Psi)$, it is possible to recognize some typical deviation patterns. In Figure A.1, 3 such patterns are illustrated on a circular shape with radius $r = 10mm$, as a result of scaling in x-axis $\varphi_x = 0.98$ (A.1(a)), translation along x-axis $\Delta x = 0.2mm$ (A.1(b)) and combined scaling and rotation $\varphi_x = 0.98, \alpha = \pi/9(rad)$ (A.1(c)).

A.2 Transformation of bi-circular shapes

Another interesting shape that is worth investigating on is the bi-circular shape, which is a joint of two circles that have the same radius but different center points, and the inner part of the joint is removed. Consider the simple case in which the two center points lie on the X axis and are symmetric with respect to the Y axis, then two parameters can be used to define such a shape, namely r_0 that defines the radius of two

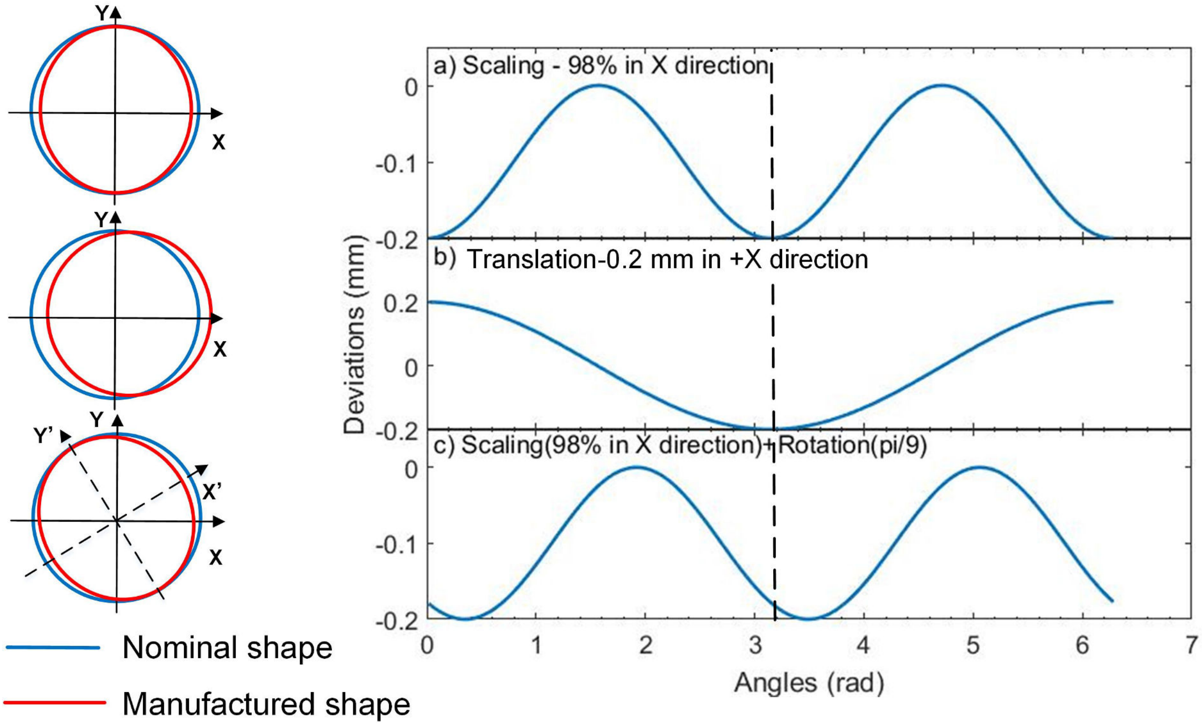

Figure A.1: Deviation of circular shape under (a) Scaling effect; (b) Translation effect; (c) Combined scaling and rotation effect

circles and $2a (0 < a < r_0)$ that defines the distance between the two center points, as can be seen in Figure A.2.

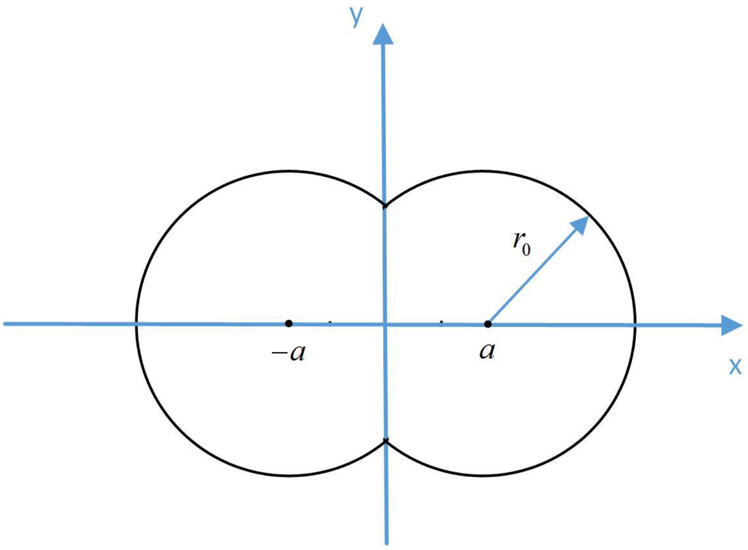

Figure A.2: Bi-circular shape in a simplified case

It is easy to derive the mathematical representation of the shape in the CCS as $(|x| - a)^2 + y^2 = r_0^2$. Likewise, substituting x, y with $r\cos(\theta), r\sin(\theta)$, we get the polar representation of the shape as $r(\theta) = a|\cos(\theta)| + \sqrt{r_0^2 - a^2\sin(\theta)^2}$. Figure A.3 provides a plot of this function for a shape with $r_0 = 4mm, a = 3mm$, two sharp transitions can be observed at $\pi/2$ and $3\pi/2$ where the two circles join. Transformation of the shape is applied using the approach discussed in Section 3.3.1 and the mathematical form of the transformed shape in the PCS can be derived using symbolic transformation. As an example, the derivation of the deviation function under the scaling effects will be briefly demonstrated. Denote φ_x and φ_y as the scaling factors, the in-plane deviation is represented as the radial difference between the scaled shape and the original shape:

$$\begin{aligned}\Delta r_s(\theta) &= r_s(\theta) - r(\theta)\\ &= \frac{\left[a\varphi_x\varphi_y^2|\cos(\theta)| + \varphi_x\varphi_y\sqrt{r_0^2\varphi_x^2\sin(\theta)^2 + r_0^2\varphi_y^2\cos(\theta)^2 - a^2\varphi_x^2\sin(\theta)^2}\right]}{[\varphi_x^2\sin(\theta)^2 + \varphi_y^2\cos(\theta)^2]} - r(\theta)\end{aligned} \tag{A.2}$$

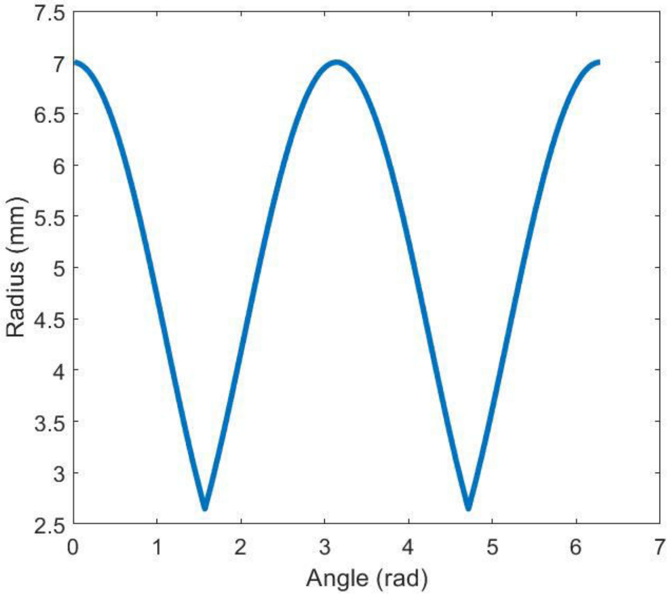

Figure A.3: Polar representation of the bi-circular shape

By setting different values to the scaling factors, the in-plane deviation patterns can be visualized, as seen in Figure A.4.

A.3 Transformation of elliptical shapes

An ellipse can be defined by two parameters, the semi-major axis length a and semi-minor axis length b. For elliptical shapes, its polar representation is $r(\theta) = ab/\sqrt{b^2\cos(\theta)^2 + a^2\sin(\theta)^2}$. This representation is derived by substituting the Carte-

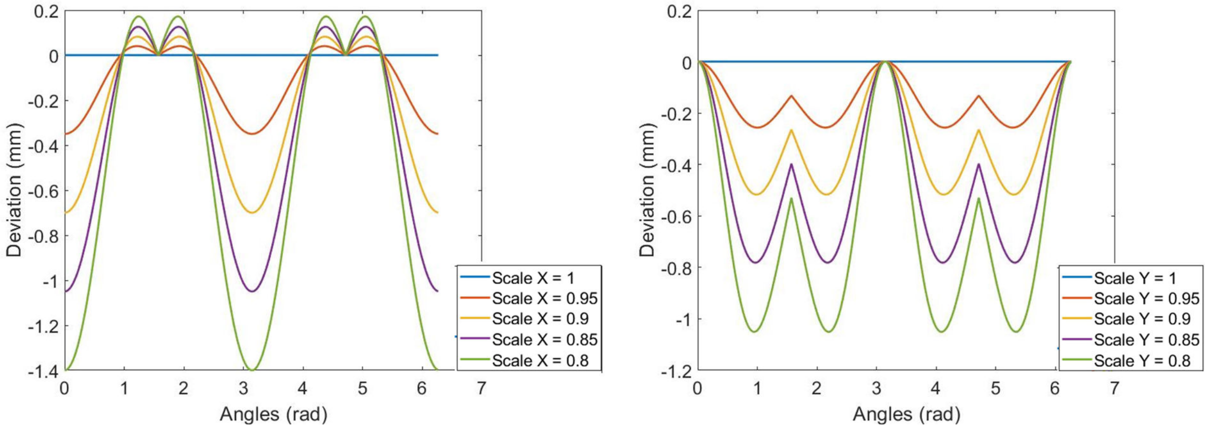

Figure A.4: In-plane deviation patterns of the bi-circular shape under different scaling factors along X and Y axis

sian coordinates x, y with $r\cos(\theta), r\sin(\theta)$ in the function $x^2/a^2 + y^2/b^2 = 1$. Figure A.5 shows the polar representation of an elliptical shape with $a = 4mm, b = 3mm$. Similarly, we can derive the polar equation of the transformed ellipse shape and therefore the shape deviation function following the same method as adopted in dealing with the circular shape. The equation is too long to be put in this document, but the simplified equation under single scaling transformation effects will be discussed here.

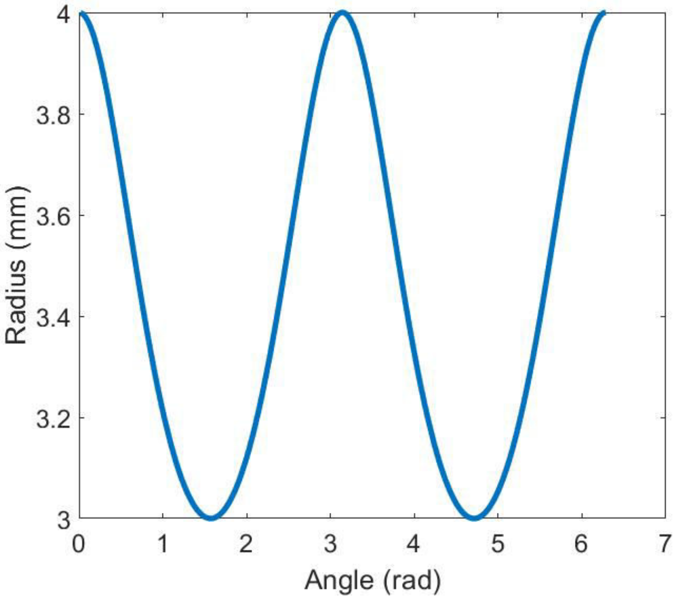

Figure A.5: Polar representation of the bi-circular shape

Following the transformation approach in Section 3.3.1, the scaled elliptical shape is represented in PCS as Equation A.3.

$$r_s(\theta) = \frac{\sqrt{2}ab\varphi_x\varphi_y}{\sqrt{b^2\cos(\theta)^2 + a^2\sin(\theta)^2 + (b^2\varphi_y^2 - a^2\varphi_x^2)\cos(2\theta)}} \tag{A.3}$$

Therefore, the in-plane deviation is derived as:

$$\Delta r_s(\theta) = \\ \sqrt{2}ab\left(\frac{\varphi_x\varphi_y}{\sqrt{b^2\cos(\theta)^2 + a^2\sin(\theta)^2 + (b^2\varphi_y^2 - a^2\varphi_x^2)\cos(2\theta)}} - \frac{1}{\sqrt{b^2\cos(\theta)^2 + a^2\sin(\theta)^2}}\right) \tag{A.4}$$

By setting different values to the scaling factors, the in-plane deviation patterns can be visualized, as seen in Figure A.6.

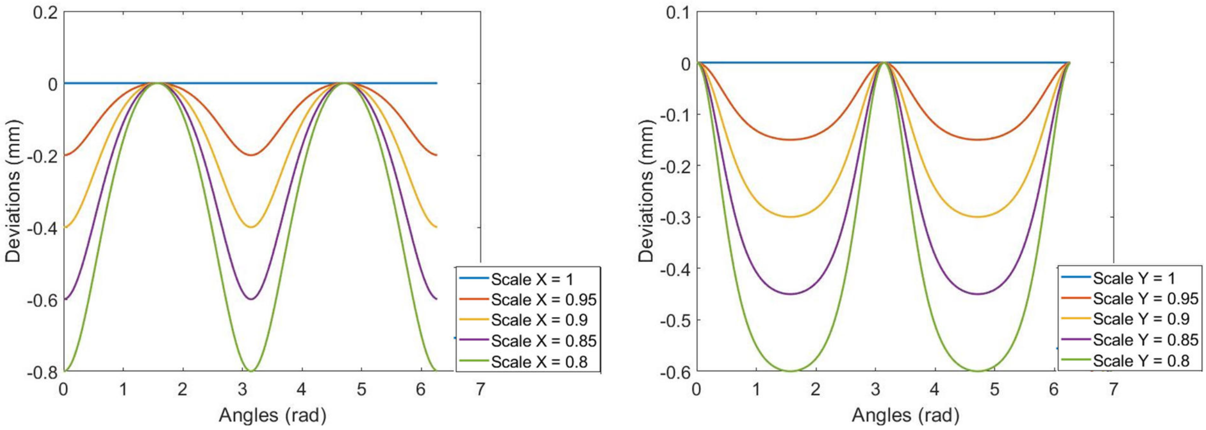

Figure A.6: In-plane deviation patterns of the elliptical shape under different scaling factors along X and Y axis

Even though only the scaling parameters are considered for bi-circular and elliptical shapes, the complete deviation function incorporating all the transformation parameters can be calculated through symbolic computation. More deviation patterns can be discovered by varying the parameter values.

A.4 Transformation of polygonal shapes

A more general case that is worth investigating is the polygonal shape. For an arbitrary convex polygon with N vertices sorted in counter-clockwise order, $f(\theta;\Psi)$ could be represented by evaluating the polar function of nominal and transformed shape in an edge-wise routine. Different from circles whose polar function is simply constant, the radius of a polygon varies discretely as the polar angle scans along the boundary and should be specifically treated for each edge. The edges are defined by adjacent point pairs as $[P_1, P_2], [P_2, P_3], ..., [P_{N-1}, P_N], [P_N, P_1]$. Transforming point coordinates to the PCS, the angular range covered by each edge is determined by the angles of its end points. It can be seen from Figure A.7(a) that, the polygon radius at θ is computed with regard to the specific edge whose angular range contains θ. Assuming that this edge is $[P_b(x_b, y_b), P_a(x_a, y_a)]$ with the range $[\theta_b, \theta_a]; a, b = 1, 2, ..., N$, the radius is then derived as $r^\circ(\theta)$ in Equation A.5.

$$
\begin{aligned}
&x(\theta) = x_b - t(\theta)(x_b - x_a) \\
&y(\theta) = y_b - t(\theta)(y_b - y_a) \\
&t(\theta) = \frac{y_b - \tan(\theta) x_b}{\tan(\theta)(x_a - x_b) + y_b - y_a}, \theta \in [\theta_b, \theta_a] \\
&r^\circ(\theta) = \sqrt{x(\theta)^2 + y(\theta)^2}
\end{aligned}
\tag{A.5}
$$

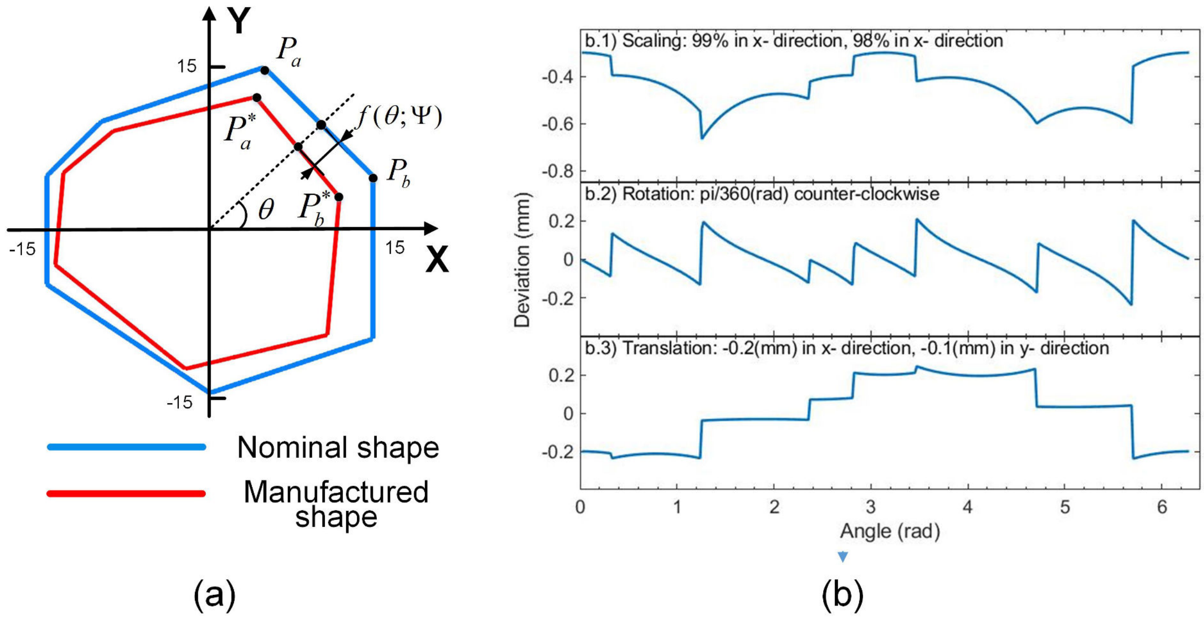

Figure A.7: (a) In-plane deviation of a polygonal shape (b) Deviation patterns in the deviation space

The radius of the transformed shape is calculated by the same means, other than that the angular ranges of edges have to be re-estimated according to new positions of their end points calculated following Equation 3.15. As seen in Figure A.7(a), the original points P_b, P_a now become P_b^*, P_a^* after applying the transformations. In this way, $f(\theta; \Psi)$ is known by evaluating $r^\circ(\theta)$ and $r^*(\theta; \Psi, r^\circ(\theta))$ at any given θ. Figure A.7(b) illustrates three deviation patterns of the polygonal shape obtained by separately assigning the parameters as $\varphi_x = 0.99, \varphi_y = 0.98$ (A.7(b.1)), $\alpha = \pi/360(rad)$ (A.7(b.2)) and $\Delta x = -0.2mm, \Delta x = -0.1mm$ (A.7(b.3)). This model can also be extended to freeform shape by densely sampling points on its boundary and approximating the shape with a complex polygon constructed from the sequentially connected points. Since Ψ is the only parameter, this model is insensitive to the complexity of shape and the number of parameters is substantially reduced compared with methods as discussed in Section 3.2. Given the explicit form of the deviation functions and observed deviation data, the parameters can be estimated, thus helping understanding of the causes of in-plane deviations.

Abstract

The intricate error sources within different stages of the Additive Manufacturing (AM) process have brought about major issues regarding the dimensional and geometrical accuracy of the manufactured product. Therefore, effective modeling of the geometric deviations is critical for AM. The Skin Model Shapes (SMS) paradigm offers a comprehensive framework aiming at addressing the deviation modeling problem at different stages of product lifecycle, and is thus a promising solution for deviation modeling in AM. In this thesis, considering the layer-wise characteristic of AM, a new SMS framework is proposed which characterizes the deviations in AM with in-plane and out-of-plane perspectives.

The modeling of in-plane deviation aims at capturing the variability of the 2D shape of each layer. A shape transformation perspective is proposed which maps the variational effects of deviation sources into affine transformations of the nominal shape. With this assumption, a parametric deviation model is established based on the Polar Coordinate System which manages to capture deviation patterns regardless of the shape complexity. This model is further enhanced with a statistical learning capability to simultaneously learn from deviation data of multiple shapes and improve the performance on all shapes.

Out-of-plane deviation is defined as the deformation of layer in the build direction. A layer-level investigation of out-of-plane deviation is conducted with a data-driven method. Based on the deviation data collected from a number of Finite Element simulations, two modal analysis methods, Discrete Cosine Transform (DCT) and Statistical Shape Analysis (SSA), are adopted to identify the most significant deviation modes in the layer-wise data. The effect of part and process parameters on the identified modes is further characterized with a Gaussian Process (GP) model.

The discussed methods are finally used to obtain high-fidelity SMSs of AM products by deforming the nominal layer contours with predicted deviations and rebuilding the complete non-ideal surface model from the deformed contours. A toolbox is developed in the MATLAB environment to demonstrate the effectiveness of the proposed methods.

Résumé

Les différentes étapes et processus de la fabrication additive (FA) induisent des erreurs de sources multiples et complexes qui soulèvent des problèmes majeurs au niveau de la qualité géométrique du produit fabriqué. Par conséquent, une modélisation effective des écarts géométriques est essentielle pour la FA. Le paradigme Skin Model Shapes (SMS) offre un cadre intégral pour la modélisation des écarts géométriques des produits manufacturés et constitue ainsi une solution efficace pour la modélisation des écarts géométriques en FA.

Dans cette thèse, compte tenu de la spécificité de fabrication par couche en FA, un nouveau cadre de modélisation à base de SMS est proposé pour caractériser les écarts géométriques en FA en combinant une approche dans le plan et une approche hors plan.

La modélisation des écarts dans le plan vise à capturer la variabilité de la forme 2D de chaque couche. Une méthode de transformation des formes est proposée et qui consiste à représenter les effets de variations sous la forme de transformations affines appliquées à la forme nominale. Un modèle paramétrique des écarts est alors établi dans un système de coordonnées polaires, quelle que soit la complexité de la forme. Ce modèle est par la suite enrichi par un apprentissage statistique permettant la collecte simultanée de données des écarts de formes multiples et l'amélioration des performances de la méthode.

La modélisation des écarts hors plan est réalisée par la déformation de la couche dans la direction de fabrication. La modélisation des écarts hors plan est effectuée à l'aide d'une méthode orientée données. Sur la base des données des écarts obtenues à partir de simulations par éléments finis, deux méthodes d'analyse modale: la transformée en cosinus discrète (DCT) et l'analyse statistique des formes (SSA) sont exploitées. De plus, les effets des paramètres des pièces et des procédés sur les modes identifiés sont caractérisés par le biais d'un modèle à base de processus Gaussien.

Les méthodes présentées sont finalement utilisées pour obtenir des SMSs haute-fidélité pour la fabrication additive en déformant les contours de la couche nominale avec les écarts prédits et en reconstruisant le modèle de surface non idéale complet à partir de ces contours déformés. Une toolbox est développée dans l'environnement MATLAB pour démontrer l'efficacité des méthodes proposées.

université PARIS-SACLAY
ÉCOLE DOCTORALE
Sciences mécaniques et énergétiques, matériaux et géosciences (SMEMAG)

Titre : Modèles Géométriques avec Défauts pour la Fabrication Additive

Mots clés : Skin Model Shapes, Fabrication additive, Modélisation des écarts géométriques, Analyse Modale Statistique, Transformée en Cosinus Discrète, Analyse Statistique des Formes, Processus Gaussien

Résumé :

Les différentes étapes et processus de la fabrication additive (FA) induisent des erreurs de sources multiples et complexes qui soulèvent des problèmes majeurs au niveau de la qualité géométrique du produit fabriqué. Par conséquent, une modélisation effective des écarts géométriques est essentielle pour la FA. Le paradigme Skin Model Shapes (SMS) offre un cadre intégral pour la modélisation des écarts géométriques des produits manufacturés et constitue ainsi une solution efficace pour la modélisation des écarts géométriques en FA. Dans cette thèse, compte tenu de la spécificité de fabrication par couche en FA, un nouveau cadre de modélisation à base de SMS est proposé pour caractériser les écarts géométriques en FA en combinant une approche dans le plan et une approche hors plan. La modélisation des écarts dans le plan vise à capturer la variabilité de la forme 2D de chaque couche. Une méthode de transformation des formes est proposée et qui consiste à représenter les effets de variations sous la forme de transformations affines appliquées à la forme nominale. Un modèle paramétrique des écarts est alors établi dans un système de coordonnées polaires, quelle que soit la complexité de la forme. Ce modèle est par la suite enrichi par un apprentissage statistique permettant la collecte simultanée de données des écarts de formes multiples et l'amélioration des performances de la méthode. La modélisation des écarts hors plan est réalisée par la déformation de la couche dans la direction de fabrication. La modélisation des écarts hors plan est effectuée à l'aide d'une méthode orientée données. Sur la base des données des écarts obtenues à partir de simulations par éléments finis, deux méthodes d'analyse modale: la transformée en cosinus discrète (DCT) et l'analyse statistique des formes (SSA) sont exploitées. De plus, les effets des paramètres des pièces et des procédés sur les modes identifiés sont caractérisés par le biais d'un modèle à base de processus Gaussien. Les méthodes présentées sont finalement utilisées pour obtenir des SMSs haute-fidélité pour la fabrication additive en déformant les contours de la couche nominale avec les écarts prédits et en reconstruisant le modèle de surface non idéale complet à partir de ces contours déformés. Une toolbox est développée dans l'environnement MATLAB pour démontrer l'efficacité des méthodes proposées.

Title : Skin Model Shapes for Additive Manufacturing

Keywords : Skin Model Shapes, Additive Manufacturing, Geometric deviation modeling, Statistical modal analysis, Discrete Cosine Transform, Statistical Shape Analysis, Gaussian Process

Abstract :

Effective modeling of the geometric deviations is critical for Additive Manufacturing (AM). The Skin Model Shapes (SMS) offers a comprehensive framework aiming at addressing the deviation modeling problem at different stages of product lifecycle, and is thus a promising solution for deviation modeling of AM. In this thesis, considering the layer-wise characteristic of AM, a new SMS framework is proposed which characterizes the deviations in AM with in-plane and out-of-plane perspectives. The modeling of in-plane deviation aims at capturing the variability of the 2D shape of each layer. A shape transformation perspective is proposed which maps the variational effects of deviation sources into affine transformations of the nominal shape. With this assumption, a parametric deviation model is established which manages to capture deviation patterns regardless of the shape complexity. This model is further enhanced with a statistical learning capability to simultaneously learn from deviation data of multiple shapes and improve the modeling accuracy on all shapes. A layer-level investigation of out-of-plane deviation is conducted with a data-driven method. Based on the deviation data collected from a number of Finite Element simulations, two modal analysis methods, Discrete Cosine Transform (DCT) and Statistical Shape Analysis (SSA), are adopted to identify the most significant deviation modes in the layer-wise data. The effect of part and process parameters on the identified modes is further characterized with a Gaussian Process (GP) model. The discussed methods are finally used to obtain high-fidelity SMSs of AM products by deforming the nominal layer contours with predicted deviations and using a graph-based layer connection technique to rebuild the complete non-ideal surface model from the deformed contours.

Université Paris-Saclay
Espace Technologique / Immeuble Discovery
Route de l'Orme aux Merisiers RD 128 / 91190 Saint-Aubin, France